

# Azimuthal Transverse Single-spin Asymmetries of Inclusive Jets and Charged Pions Within Jets from Polarized-proton Collisions

at  $\sqrt{s} = 500 \text{ GeV}$

## A Note for the 2011 Analysis

James L. Drachenberg,<sup>1</sup> J. Kevin Adkins,<sup>2</sup> Renee  
Fatemi,<sup>2</sup> Carl Gagliardi,<sup>3</sup> and Adam Gibson-Even<sup>4</sup>

<sup>1</sup>*Lamar University, Physics Department, Beaumont, Texas 77710, USA*

<sup>2</sup>*University of Kentucky, Lexington, Kentucky, 40506-0055, USA*

<sup>3</sup>*Texas A&M University, College Station, Texas 77843, USA*

<sup>4</sup>*Valparaiso University, Valparaiso, Indiana 46383, USA*

(Dated: June 10, 2017)

## CONTENTS

I. Introduction	3
II. Run Selection	4
III. Jet Reconstruction	4
IV. Event Cuts	7
V. Beam Polarization	10
VI. Transverse Single-spin Asymmetry	11
VII. Simulations	13
A. Tuning Intrinsic $k_T$	15
B. Simulation Trigger Thresholds	16
C. Minimum Bias Trigger and Level-2 Algorithm	20
D. Data-Monte Carlo Comparisons	23
VIII. Systematics	23
A. Kinematic Shifts	25
1. Jet $p_T$ Correction	25
2. Pion $z$ Correction	28
3. Pion $j_T$ Correction	34
B. Generator-level Associations	34
C. Trigger Bias	43
D. Azimuthal Resolutions	46
E. Non-uniform Acceptance Effects	51
F. Contaminations to Pion Sample	56
G. Polarization Uncertainty	74
IX. Asymmetry Analysis	75
A. Statistical Cross-checks	77
B. Results	82

1. Inclusive Jet Asymmetry	82
2. Collins-like Asymmetry	84
3. Collins Asymmetry	85
C. Comparison to Models	90
 A. Run List	 93
 B. Resolution Corrections	 95
 C. Non-pion Background Corrections	 107
 Acknowledgments	 118
 References	 118

## I. INTRODUCTION

The following is a STAR Note for the 2011 analysis of transverse single-spin asymmetries in inclusive jet production and in the production of pions within jets. The observables for these measurements are denoted  $A_{UT}^{\sin\phi}$  where the superscript varies depending upon the modulation of the asymmetry. This convention has been chosen to be consistent with existing measurements from SIDIS [1–3]. Another common notation for transverse single-spin asymmetries is  $A_N$ . This would apply appropriately to the asymmetry in inclusive jet production, here, labeled  $A_{UT}^{\sin\phi_S}$ . The use of this notation in the measurement of pions within jets is a bit less clear, since the asymmetries are not in the azimuthal distribution of pions relative to the beams but rather relative to the jet frame of reference. Here, we have decided it is more clear to utilize  $A_{UT}$  for all measurements and clarify the particular observable with the modulation in the superscript.

Described, herein, are the measurements of three observables: the inclusive jet asymmetry, the Collins asymmetry, and the so-called “Collins-like” asymmetry. The inclusive jet asymmetry is sensitive to the twist-3 PDF [4, 5] that is related to the  $k_T$ -integrated Sivers function [6, 7]. The Collins asymmetry is sensitive to transversity (describing the transverse polarization of quarks within a transversely polarized nucleon) and the “Collins” fragmen-

tation function, a fragmentation function correlating the scattered quark polarization to the transverse momenta of the fragmenting hadrons (calculated relative to the parent jet axis) [8]. The “Collins-like” asymmetry is essentially the gluon-analog of the Collins asymmetry, e.g. with sensitive to linearly-polarized gluons rather than transversely polarized quarks [9].

## II. RUN SELECTION

The present data were collected in 2011 during the  $p + p$  transverse polarization period. All  $p + p$  data in 2011 were taken at  $\sqrt{s} = 500$  GeV/ $c$ . Runs were chosen from the “pp500\\_production\\_2011” production.

To ensure events of good quality, data-taking runs were required to have sensible averages of towers above the BHT1, BHT2, and BHT3 thresholds,  $N_{\text{trig}}$ , as well as sensible trigger rates for BHT1, BHT2, JP0, JP1, JP2\*L2JetHigh, and AJP. Specifically,  $\langle N_{\text{trig}} \rangle$  was calculated relative to the number of triggered events. The trigger rates were evaluated by looking at the ratio of prescale-corrected triggered events to prescale-corrected minimum-bias events. By examining the quantities run-by-run, 78 runs were excluded as outliers.  $\langle N_{\text{trig}} \rangle$  and the trigger rates, after excluding outliers are shown in Figs. 1 and 2, respectively.

After jet trees had been produced for the runs, excluding the outliers, it was apparent that 36 runs experienced significant hot towers or dead regions in the BEMC or EEMC. These runs were also excluded. Runs were also excluded in the absence of good polarization information (Sec. V). Altogether, this leaves a total of 702 “good” runs (Appendix A).

## III. JET RECONSTRUCTION

Jets were reconstructed with the standard STAR jet-finding code, as can be found in the CVS repository (StRoot/StJetMaker/macros/RunJetFinder2009pro.C). Events were filtered to accept only the following triggers: BBCMB, VPDMB, BHT0\*VPDMB, BHT1, BHT2, JP0, JP1, JP2\*L2JetHigh, and AJP. The trigger simulator was defined for the 2011 jet-patch triggers. Jets were reconstructed from TPC tracks and/or EMC towers using the anti- $k_T$  jet-finding algorithm [10] with R-parameters of 0.5, 0.6, and 0.7. Different branches were set for jets with only EMC towers or with EMC towers and TPC tracks. Tracks were required to pass the following quality cuts:

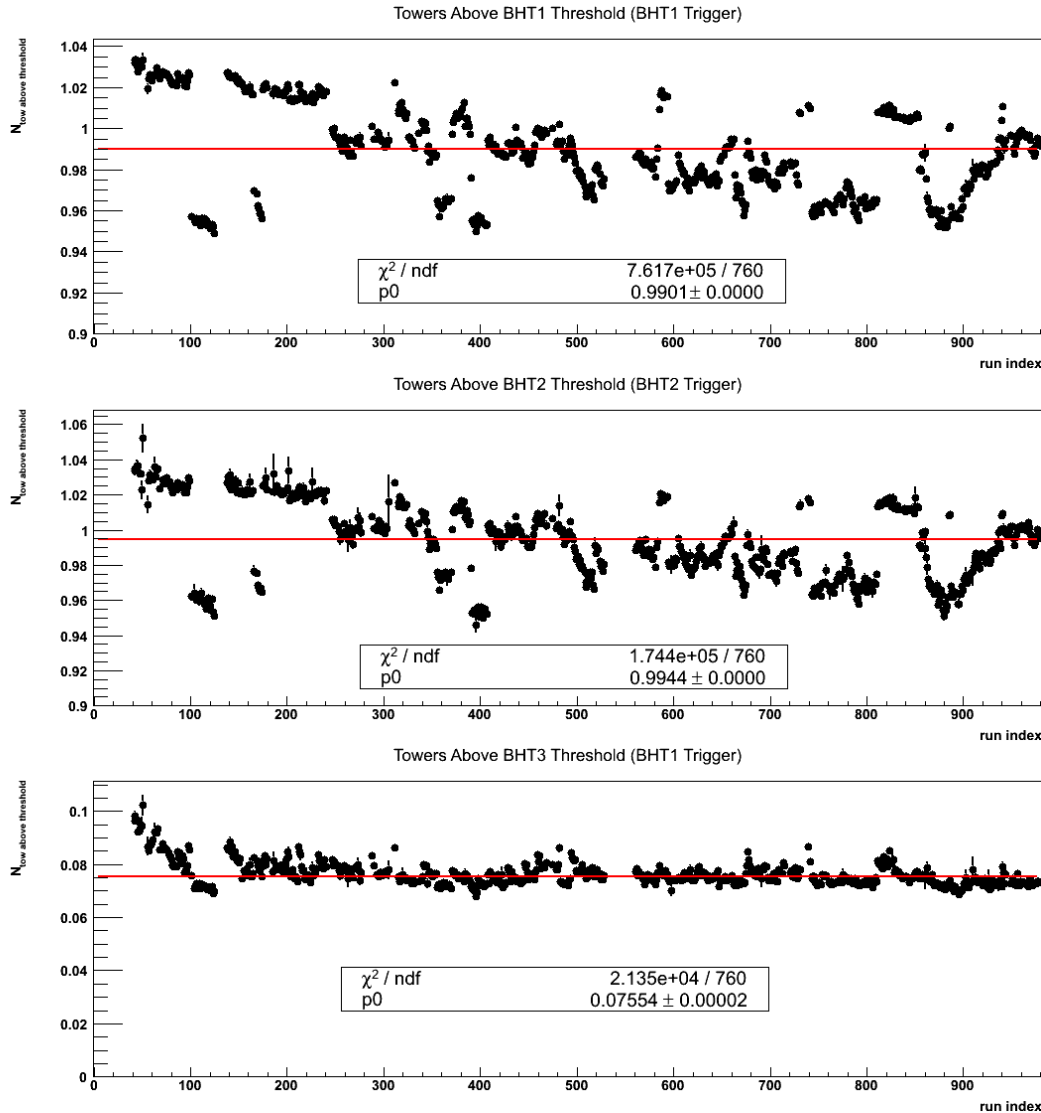


FIG. 1. Average number of towers per event above barrel high-tower trigger thresholds. Averages are shown as a function of run (indexed chronologically). The distributions are fit with a constant to give a sense of the overall average.

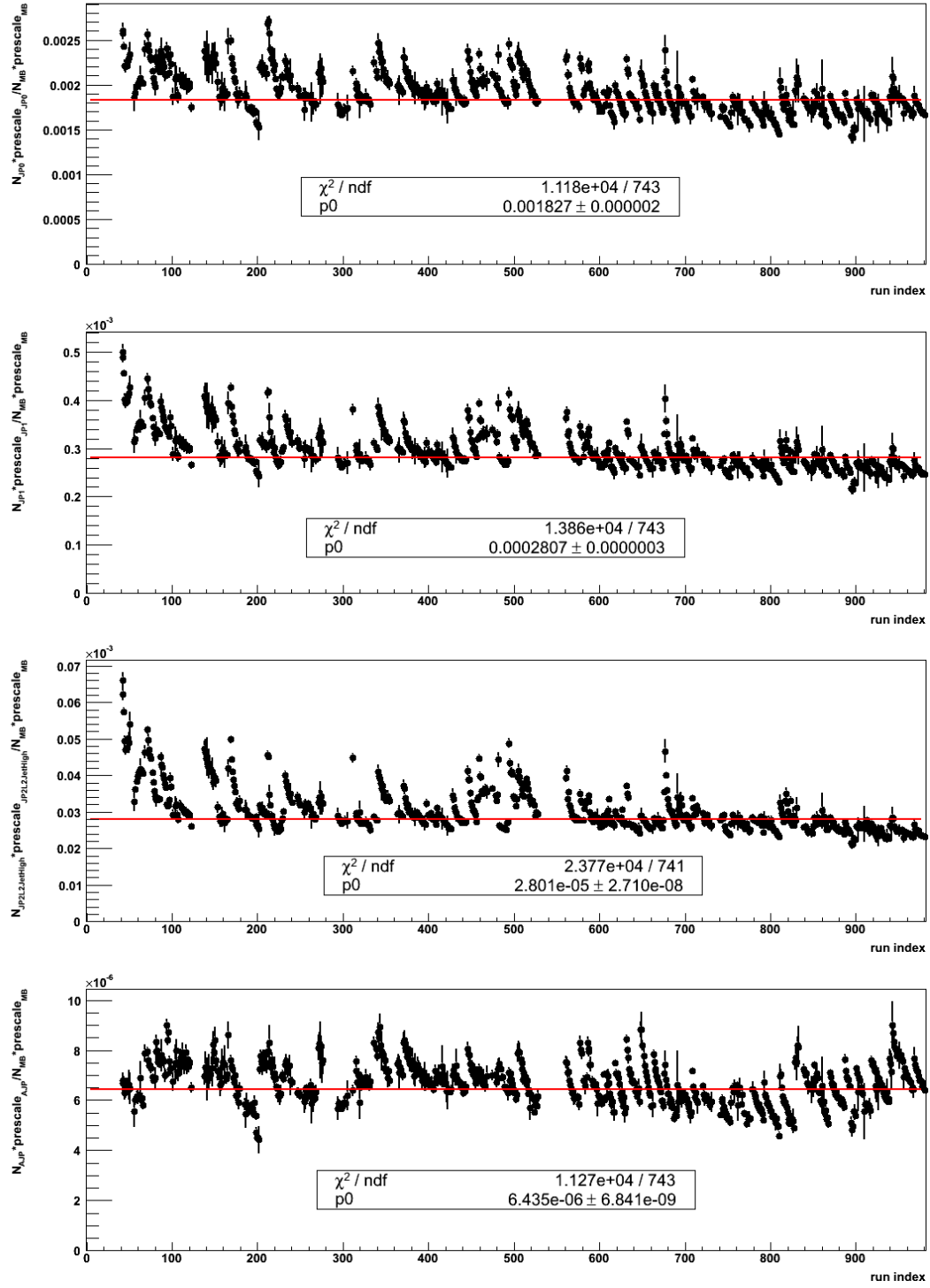


FIG. 2. Average trigger rate for (top) JP0, (second) JP1, (third) JP2\*L2JetHigh, and (bottom) AJP, shown as a function of run (indexed chronologically). Rates are calculated by dividing the prescale-corrected number of JP-triggered events by the number of prescale-corrected minimum-bias events. The distributions are fit with a constant to give a sense of the overall average.

- “Flag”  $> 0$
- $N_{\text{hits}} > 12$  or 5 depending on the branch
- $N_{\text{hits}}/N_{\text{poss}} > 0.51$
- $p_T$ -dependent DCA cut
- $0.2 < p_{T,\text{track}} < 200 \text{ GeV}/c$
- $|\eta| < 2.5$
- Radius of last point  $> 125 \text{ cm}$

EMC towers were required to pass the following quality cuts:

- Status = 1
- Masking known hot towers from the jet finder
- ADC – pedestal  $> 4$  and ADC – pedestal  $> 3 \times \text{RMS}$
- $E_T > 0.2 \text{ GeV}$

For reconstruction, jets are required to have a minimum  $p_T$  of 5 GeV with a maximum of 200 GeV. As with the 2009 inclusive-jet analysis [11], the jet finder used the so-called “100% subtraction scheme” for tracks pointing to EMC towers. Specifically, this hadronic subtraction scheme takes away up to 100% of the track momentum from the struck tower. If the subtraction would lead to a negative result, the tower energy is set to zero.

#### IV. EVENT CUTS

Event cuts largely follow those typical of STAR inclusive-jet analyses (e.g. the 2009 inclusive-jet  $A_{LL}$  [11]). Events were accepted for the analysis if they passed the following cuts:

- A good polarization value from the CNI group analysis

- A hardware trigger for VPDMB or a hardware and software trigger for JP0, JP1, JP2\*L2JetHigh, or AJP (IDs listed in Table I; note: due to hardware trigger prescales, the event can be selected by satisfying a hardware and software condition for two different triggers, e.g. a software trigger condition for JP0 and a hardware trigger condition for JP2\*L2JetHigh). The run QA, polarization, and trigger selections yield a sample of 81M VPDMB and 19.2M JP2\*L2JetHigh events, corresponding to 80.5% and 85.1%, respectively, of the total for the 2011 transverse run. According to the luminosity monitoring page [12], this represents 23.2 of the 27.248 pb<sup>-1</sup> of JP2\*L2JetHigh in the 2011 transverse run.
- A bunch crossing outside the blue (111 – 119) and yellow (31 – 39) beam abort gaps
- Event vertex with positive rank
- Event vertex with  $|z| < 90$  cm for jet-patch triggers or  $|z| < 30$  cm for VPDMB
- For VPDMB triggers, require  $|z_{\text{TPC}} - z_{\text{VPD}}| < 6$  cm
- Spin bit of 5, 6, 9, or 10

The spin bits and their relation to spin orientations are summarized in Table II. The spin states are reported by CDEV relative to their orientation at the source. In 2011 there were an even number of spin flips between the source and the 12:00 position, the orientation at the source is the same as the orientation at 12:00. There is a single spin flip for each beam from the 12:00 position to STAR. Thus, the spin orientations as reported by CDEV are flipped relative to their orientations at STAR.

In addition to the aforementioned event cuts, individual jets were accepted for analysis provided fulfilling the following requirements:

- Containing no tracks with  $p_T > 30$  GeV/ $c$
- $R_T < 0.94$
- $\sum p_T^{\text{charge}} > 0.5$  GeV/ $c$
- $|\eta_{\text{detector}} - 0.1| < 0.8$

Trigger Name	Trigger ID	First Run	Last Run
VPDMB	320000	12038078	12038092
VPDMB	320001	12038106	12061018
VPDMB	320011	12064003	12065018
VPDMB	320021	12075019	12098031
JP0	320600	12038078	12098031
JP1	320601	12038078	12098031
JP2*L2JetHigh	320602	12038078	12098031
AJP	320603	12038078	12098031

TABLE I. Various trigger IDs used for the 2011 inclusive jet analysis.

Spin Bits	Blue Beam	Yellow Beam
5	down	down
6	down	up
9	up	down
10	up	up

TABLE II. Spin bits and spin orientations at the STAR IR. These are flipped relative to both the source and the 12:00 position.

- $|\eta| < 1.0$
- $6.0 < p_T < 55 \text{ GeV}/c$
- $|\eta_{\text{jet}} - \eta_{\text{patch}}| < 0.6$  and  $|\phi_{\text{jet}} - \phi_{\text{patch}}| < 0.6$  (jet-patch triggered events, only)
- $p_T > 6, 7.1, 9.9, \text{ or } 16.3 \text{ GeV}/c$  for VPDMB, JP0, JP1, or JP2/AJP, respectively

For purposes of trigger classification (e.g. the  $p_T$  cut or trigger-dependent corrections), jets are assigned to the least restrictive trigger available, given the hardware, software, and geometric triggers. The  $p_T$  thresholds have been chosen to account for the ramp-up for the various triggers. The jet-patch trigger thresholds are summarized in Table III. The

Trigger Name	ADC Threshold	$E_T$ Threshold [GeV]
JP0	32	6.4
JP1	43	9.0
JP2*L2JetHigh	64	13.9

TABLE III. Trigger thresholds for various jet-patch triggers used in the 2011 analysis.

conversion from ADC channel to transverse energy is  $E_T \approx 0.236 \times (\text{ADC} - 5)$  GeV.

Charged particles within jets satisfying the aforementioned cuts were accepted for analysis given the following criteria:

- $0.1 < z < 0.8$
- $\Delta R = \sqrt{(\eta_{\text{jet}} - \eta_{\text{track}})^2 + (\phi_{\text{jet}} - \phi_{\text{track}})^2} > 0.04$
- $-1.5 < n_\sigma(\pi) < 2.5$
- $N_{\text{hits}, dE/dx} > 5$

## V. BEAM POLARIZATION

The beam polarizations were provided by the CNI polarimetry group [13]. For each fill, an initial polarization ( $P_0$ ), initial time ( $t_0$ ), and decay slope ( $dP/dt$ ) were quoted for each beam. The event-by-event polarizations were calculated as  $P_0 + (dP/dt)\Delta t$ , where  $\Delta t$  is the difference between  $t_0$  and the event timestamp. The average beam polarizations are summarized in Table IV. The polarization uncertainty is divided into three pieces: an overall scale for a given running period, a fill-to-fill scale systematics, and uncertainties on the fill-to-fill profile corrections. The overall scale uncertainty for 2011 is  $\sigma(P)/P = 3.3\%$  for both blue and yellow beams. The fill-to-fill scale uncertainties for 2011 are  $\sigma(P)/P = 0.9\%$  for the scale and  $\sigma(P)/P = 0.5\%$  for the profile correction. This yields a total polarization uncertainty of 3.5% for the 2011 transverse run, which is treated as an uncertainty on the overall sale of the asymmetries.

For the  $\Delta t$  calculation, some care is needed. The  $\mu$ DSTs and jet trees utilize a TDatime structure to store the event timestamp. The time stored in these structures appears to be that

Trigger Name	Average Blue Beam Polarization	Average Yellow Beam Polarization
VPDMB	0.530	0.525
JP0	0.527	0.509
JP1	0.527	0.510
JP2*L2JetHigh	0.529	0.511
AJP	0.529	0.510

TABLE IV. Average beam polarizations in terms of event trigger.

of the event in GMT. When the Convert() function is used to obtain the appropriate Unix timestamp, the function appears to assume the stored information is the local time according to the machine on which the jobs run. The effect is a shift by whatever is appropriate to convert the time of the local machine to GMT. This is 4 or 5 hours on RCF and 7 or 8 hours on PDSF, depending on Daylight Saving Time.

## VI. TRANSVERSE SINGLE-SPIN ASYMMETRY

The transverse single-spin asymmetry is defined as

$$A_{UT} \sin(\phi) = \frac{\sigma^\uparrow(\phi) - \sigma^\downarrow(\phi)}{\sigma^\uparrow(\phi) + \sigma^\downarrow(\phi)}, \quad (1)$$

that is the amplitude of the sinusoidal azimuthal-dependence of the spin-dependent cross section. For purposes of measurement, it is typically convenient to utilize the so-called “cross-ratio” method [14]. This method allows both acceptance and luminosity effects to cancel, at least, to first order. The cross-ratio formula for a particular bin of  $\phi$  can be formed by combining yields from opposite detector halves ( $\alpha$  vs.  $\beta$ ) when the spin orientations are flipped, i. e.

$$A_{UT} = \frac{1}{P} \frac{\sqrt{N_\alpha^\uparrow N_\beta^\downarrow} - \sqrt{N_\alpha^\downarrow N_\beta^\uparrow}}{\sqrt{N_\alpha^\uparrow N_\beta^\downarrow} + \sqrt{N_\alpha^\downarrow N_\beta^\uparrow}}, \quad (2)$$

where  $P$  is the beam polarization. To squeeze out as much statistical precision as possible (as well as to handle correctly polarization differences when multiple triggers with varying

prescales are in play), an event-weighting variation of Eq. 2 can be utilized

$$A_{UT} = \frac{\sqrt{N_{1,\alpha}^{\uparrow} N_{1,\beta}^{\downarrow}} - \sqrt{N_{1,\alpha}^{\downarrow} N_{1,\beta}^{\uparrow}}}{\sqrt{N_{2,\alpha}^{\uparrow} N_{2,\beta}^{\downarrow}} + \sqrt{N_{2,\alpha}^{\downarrow} N_{2,\beta}^{\uparrow}}}, \quad (3)$$

where  $N_1 = \sum_i P_i$  and  $N_2 = \sum_i P_i^2$  and  $P_i$  is the polarization for the  $i^{\text{th}}$  event. To implement this in the analysis, separate histograms were filled for the numerator, weighting by the event polarization, and for the denominator, weighting by the square of the event polarization. Events were designated  $\alpha$  or  $\beta$  for jets which landed in the “top” ( $0 < \phi_{\text{jet}} < \pi$ ) or “bottom” ( $-\pi < \phi_{\text{jet}} < 0$ ) half of the barrel, respectively. A total of eight sets of histograms were, then, used, separated into numerator vs. denominator,  $\alpha$  vs.  $\beta$ , and spin-up vs. spin-down.

A critical component becomes the propagation of uncertainties, accounting for the event-weighting. The statistical uncertainties can be expressed

$$\begin{aligned} (\sigma_{A_{UT}})^2 = & \frac{1}{4(A_2 + B_2)^2} \left\{ \left( \frac{N_{1,\beta}^{\downarrow}}{A_1} \right)^2 N_{2,\alpha}^{\uparrow} + A_{UT}^2 \left( \frac{N_{2,\beta}^{\downarrow}}{A_2} \right)^2 \sum_{i_{\alpha}^{\uparrow}} P_{i_{\alpha}^{\uparrow}}^4 - 2A_{UT} \frac{N_{1,\beta}^{\downarrow} N_{2,\beta}^{\downarrow}}{A_1 A_2} \sum_{i_{\alpha}^{\uparrow}} P_{i_{\alpha}^{\uparrow}}^3 \right. \\ & + \left( \frac{N_{1,\alpha}^{\uparrow}}{A_1} \right)^2 N_{2,\beta}^{\downarrow} + A_{UT}^2 \left( \frac{N_{2,\alpha}^{\uparrow}}{A_2} \right)^2 \sum_{i_{\beta}^{\downarrow}} P_{i_{\beta}^{\downarrow}}^4 - 2A_{UT} \frac{N_{1,\alpha}^{\uparrow} N_{2,\alpha}^{\uparrow}}{A_1 A_2} \sum_{i_{\beta}^{\downarrow}} P_{i_{\beta}^{\downarrow}}^3 \right\} \\ & + \frac{1}{4(A_2 + B_2)^2} \left\{ \left( \frac{N_{1,\beta}^{\uparrow}}{B_1} \right)^2 N_{2,\alpha}^{\downarrow} + A_{UT}^2 \left( \frac{N_{2,\beta}^{\uparrow}}{B_2} \right)^2 \sum_{i_{\alpha}^{\downarrow}} P_{i_{\alpha}^{\downarrow}}^4 + 2A_{UT} \frac{N_{1,\beta}^{\uparrow} N_{2,\beta}^{\uparrow}}{B_1 B_2} \sum_{i_{\alpha}^{\downarrow}} P_{i_{\alpha}^{\downarrow}}^3 \right. \\ & + \left. \left( \frac{N_{1,\alpha}^{\downarrow}}{B_1} \right)^2 N_{2,\beta}^{\uparrow} + A_{UT}^2 \left( \frac{N_{2,\alpha}^{\downarrow}}{B_2} \right)^2 \sum_{i_{\beta}^{\uparrow}} P_{i_{\beta}^{\uparrow}}^4 + 2A_{UT} \frac{N_{1,\alpha}^{\downarrow} N_{2,\alpha}^{\downarrow}}{B_1 B_2} \sum_{i_{\beta}^{\uparrow}} P_{i_{\beta}^{\uparrow}}^3 \right\}, \end{aligned} \quad (4)$$

where  $A_1 = \sqrt{N_{1,\alpha}^{\uparrow} N_{1,\beta}^{\downarrow}}$ ,  $B_1 = \sqrt{N_{1,\alpha}^{\downarrow} N_{1,\beta}^{\uparrow}}$ ,  $A_2 = \sqrt{N_{2,\alpha}^{\uparrow} N_{2,\beta}^{\downarrow}}$ , and  $B_2 = \sqrt{N_{2,\alpha}^{\downarrow} N_{2,\beta}^{\uparrow}}$ . The polarizations, themselves, also carry uncertainties. However, the statistical component of the polarization uncertainty is expected to be tiny compared to the systematic component. Thus, the portion of the statistical uncertainty on  $A_{UT}$  coming from that of the polarization is considered negligible; and the polarization uncertainty is treated as an overall scale uncertainty and not included in the bin-by-bin calculations for  $\sigma_{A_{UT}}$ .

The cross-ratios can be binned in terms of any of the different azimuthal angles. For the present analysis, those most relevant are  $\phi_S$ ,  $\phi_S - \phi_H$ , and  $\phi_S - 2\phi_H$ . The present analysis follows the conventions as described in Ref. [9]. Here,  $\phi_S$  is the azimuthal angle

between the spin polarization vector and the event plane, i.e.  $\phi_S = \phi_{P_{\text{beam}}} - \phi_{\text{jet}}$ , while  $\phi_H$  is the azimuthal angle of the pion relative to the jet axis (in the so-called “NLS” coordinate system). To ensure the proper  $\phi$  bins were combined for the final cross-ratio calculations,  $\phi_S$  for  $\alpha$  events was always calculated treating the beam polarization as “up”; while  $\phi_S$  for  $\beta$  events was always calculated treating the beam polarization as “down.” This further ensures that for Collins(-like) measurements,  $\phi_S - \phi_H$  and  $\phi_S - 2\phi_H$ , span the full active range of  $(-\pi, +\pi)$ . Further details on this convention can be found in Ref. [15]

## VII. SIMULATIONS

To evaluate systematics such as shifts in the jet or particle kinematics or trigger and reconstruction bias events are simulated with PYTHIA, fed through GEANT to simulate detector response, and their resulting ADCs embedded into real zero-bias data. The events are generated with PYTHIA 6.426 [16] using the Perugia 0 tune [17]. The detector response is simulated with the GSTAR package based upon GEANT 3.21/08 [18].

The runs into which the PYTHIA events are embedded were chosen so as to sample the full range of luminosities encountered during the 2011 run. The runs were selected to cover a wide span of time, so that changes in detector state would be well represented in the embedding sample.

The first step in the embedding production is to generate a Gaussian vertex distribution with the width so chosen as to reflect the general shape of the data. Event weights are later used to account for residual differences in the data and generated vertex distributions. The PYTHIA events are, then, thrown with the given vertex distribution; and GSTAR simulates the detector response, using the 2011 STAR geometry. The event is, then, mixed with real zero bias data and reconstructed using production options identical to those for the data reconstruction (modulo flags specific to simulation). Unlike the 2009 analyses [11], minimum bias data play a significant role in the physics message of the 2011 analysis. Thus, the trigger filter was not an option for the 2011 simulation sample. This greatly increases the intensity of the CPU usage, and so the size of the embedding sample was kept modest. A much larger set of pure PYTHIA events were generated for purposes of comparing PYTHIA distributions to NLO pQCD. The two samples are summarized in Table V. Events

<b>Partonic <math>p_T</math></b>	<b><math>\sigma</math> (pb)</b>	<b>Fudge Factor</b>	<b>Embedding Events</b>	<b>PYTHIA Events</b>
2 – 3	$27.24 \times 10^9$	0.5922	95508	2120000
3 – 4	$5.274 \times 10^9$	0.8422	52774	600000
4 – 5	$1.480 \times 10^9$	0.9476	49194	300000
5 – 7	$7.499 \times 10^8$	0.9787	27339	200000
7 – 9	$1.553 \times 10^8$	1	25269	100000
9 – 11	$4.455 \times 10^7$	1	23764	90000
11 – 15	$2.221 \times 10^7$	1	76041	80000
15 – 20	$4.743 \times 10^6$	1	70297	72000
20 – 25	$9.623 \times 10^5$	1	70924	72000
25 – 35	$3.428 \times 10^5$	1	20008	21000
35 – 45	$4.346 \times 10^4$	1	20018	21000
45 – 55	$7.915 \times 10^3$	1	10019	11000
55 – 65	$1.816 \times 10^3$	1	7009	10000
65 – 75	$4.680 \times 10^2$	1	2005	10000
75 – $\infty$	$1.950 \times 10^2$	1	1001	10000

TABLE V. Simulation statistics for the 2011 analysis. The final partonic- $p_T$  event weights are calculated as  $w = \text{Fudge Factor} \times \sigma/N_{\text{events}}$ .

are generated in bins of partonic  $p_T$ . The individual samples must be normalized to account for differences in generated luminosity for the various  $p_T$  bins. For reasons of efficiency, PYTHIA also overestimates the cross section for the lowest partonic  $p_T$  bins (while the distribution remains appropriate). To account for this, “fudge factors” are calculated to ensure the partonic cross section is continuous across all  $p_T$  bins. This is done simply fitting functions across the different bins and tuning the weights to ensure smooth transitions across the bin boundaries.

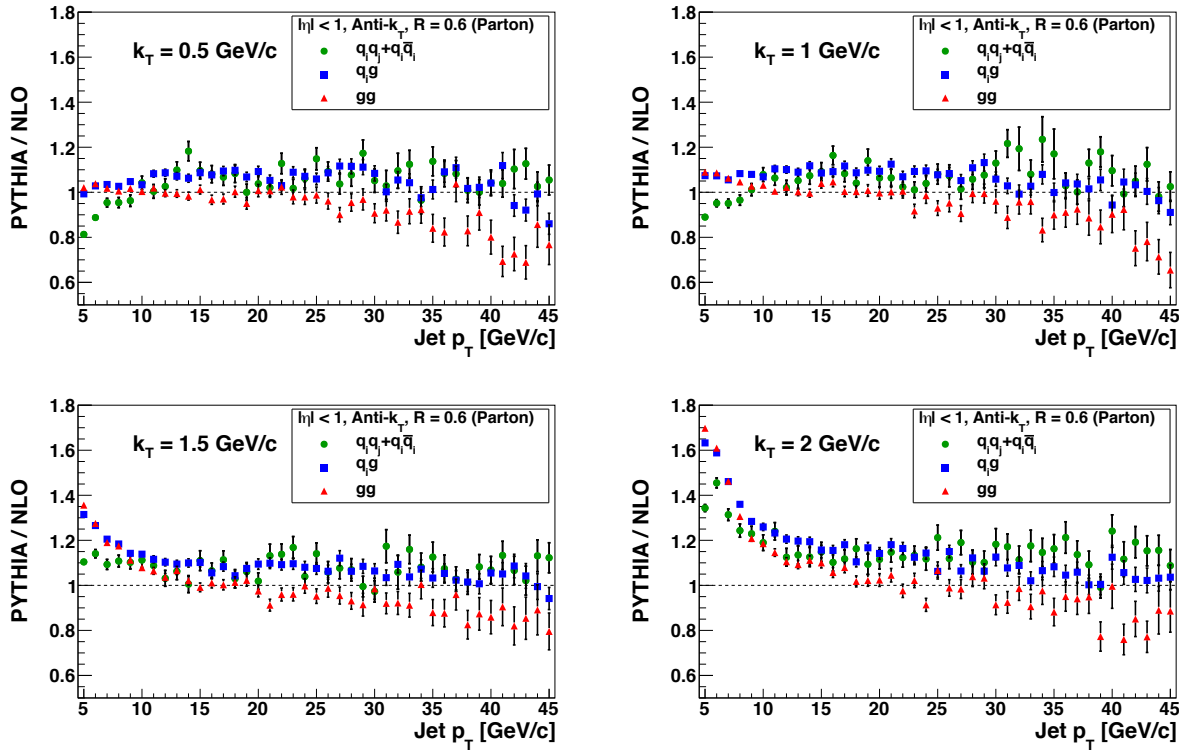


FIG. 3. Comparison of PYTHIA parton-jet cross sections to those of NLO. One can observe that as the primordial  $k_T$  parameter is dropped from 2 to 1  $\text{GeV}/c$ , the PYTHIA cross sections approach those of NLO.

### A. Tuning Intrinsic $k_T$

A comparison of PYTHIA to NLO reveals that at lower jet  $p_T$ , the PYTHIA cross sections are higher by a rather sizable factor (Fig. 3). This may not be so surprising, given that we do not run PYTHIA as an NLO generator at STAR. However, most jet observables from STAR are historically compared to predictions from NLO pQCD. Thus, it is advantageous to examine ways to tune simulations to mimic NLO as much as possible.

Figure 3 demonstrates that by tuning the primordial  $k_T$  parameter, PARP(91), the difference between PYTHIA and NLO can be reduced for all subprocesses. An optimal value of 1  $\text{GeV}/c$  was chosen for the present analysis. However, by the time of the PYTHIA-to-NLO study, the 2011 embedding sample had already been produced. Thus, it is necessary to reweight the events produced with the default value of 2  $\text{GeV}/c$  so that they mimic those

produced with intrinsic  $k_T = 1 \text{ GeV}/c$ .

In Fig. 4 one can see that there is very little apparent dependence upon parton species or partonic  $p_T$  in the distribution of  $p_x$  vs.  $p_y$  for PYTHIA particles 3 and 4. Moreover, the distributions appear consistent with symmetric, 2-D Gaussians with widths that vary predictably with primordial  $k_T$ . Figure 5 shows the results of fitting the  $p_x$  and  $p_y$  projections with Gaussians. Generally, the fits are of good quality. The centroids are all consistent with zero. The widths relate to the primordial  $k_T$  parameter as  $\sigma = k_T/\sqrt{2}$ . There is no dependence at all on parton species, particle 3 vs. 4,  $p_x$  vs.  $p_y$ , or partonic  $p_T$  bin.

The results of Figs. 4 and 5 suggest that one can reweight the embedding produced with  $k_T = 2 \text{ GeV}/c$  to simulate  $k_T = 1 \text{ GeV}/c$ . The weight factor is the product of four factors, one for each of  $p_x$  and  $p_y$  for particles 3 and 4. The factors are calculated as

$$w = \frac{\sigma_2}{\sigma_1} e^{-\frac{1}{2} p_i (\sigma_1^{-2} - \sigma_2^{-2})}, \quad (5)$$

where  $\sigma_n = n/\sqrt{2}$  and  $p_i$  is the  $i$ -component of the momentum.

## B. Simulation Trigger Thresholds

It has been observed that there are some differences between the FEE simulator and the hardware monitoring. Namely, the hardware response shows a number of active trigger patches with pedestals almost exclusively at zero, as opposed to the nominal of one (see Fig. 6 for an example). The simulator shows a few cases of active patches with zero pedestal, but not nearly to the extent of the hardware. Figure 7 shows an example of the simulated trigger response for the 2012 510 GeV run. The right-hand panel shows the difference between data and simulation for the 2012 case. At the level of  $\sim 0.1\%$  the trigger patch value from the hardware and that from the FEE simulator show one-count fluctuations. The channels with large negative differences probably arise from high gain towers. The smaller number with large positive differences are still not understood. There are, finally, the significant number of channels ( $\sim 20$ ) where the FEE simulator essentially always reports a single count higher than the hardware. These are the active patches that had zero pedestal online. The explanation appears to be that the run-by-run calorimeter configuration software did not reprogram the look-up tables (LUTs) for FEE channels with a masked tower. A

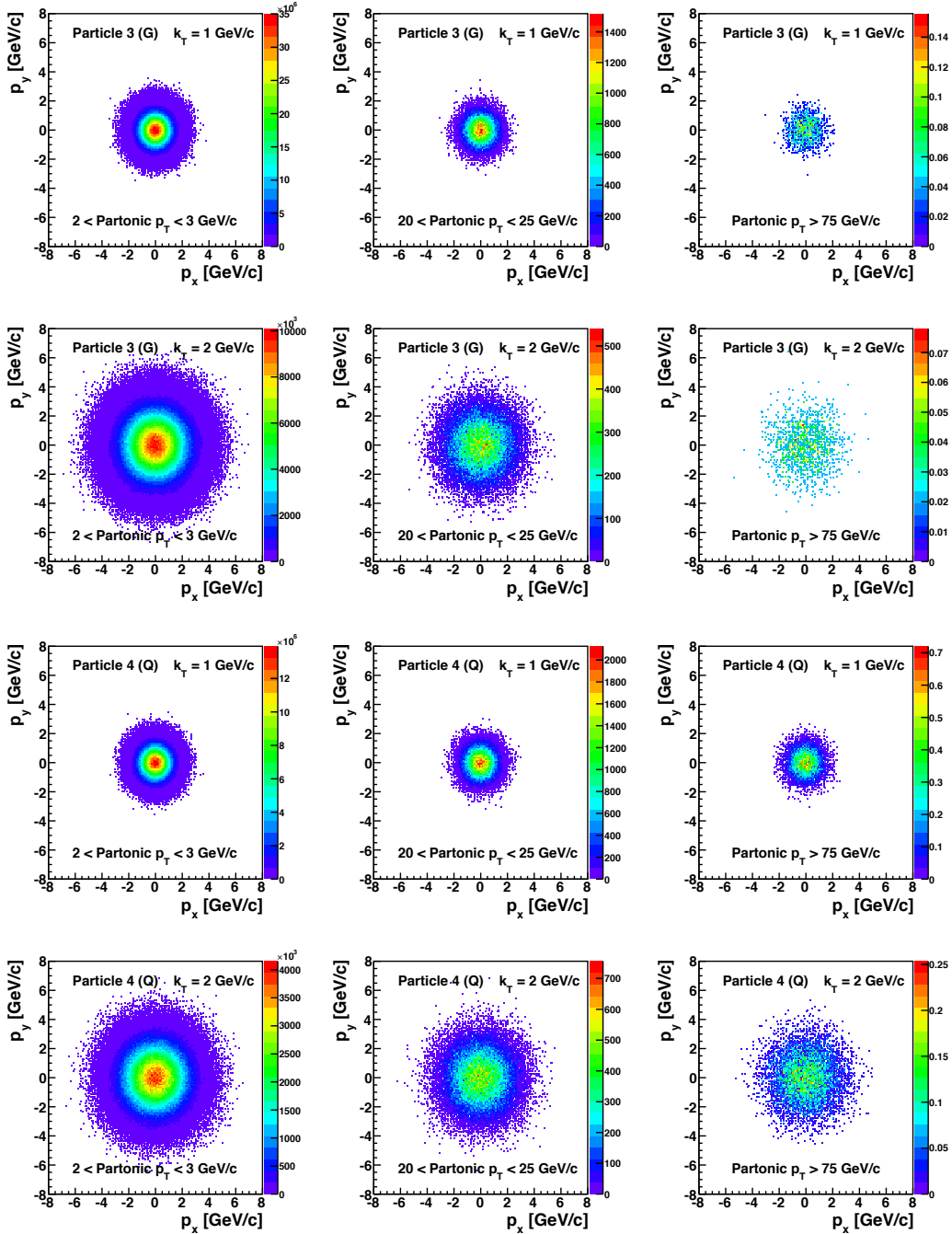


FIG. 4.  $p_x$  vs.  $p_y$  for PYTHIA particles (top two rows) 3 and (bottom two rows) 4 for two values of primordial  $k_T$  and three bins of partonic  $p_T$ . One observes that the distributions are qualitatively similar for like  $k_T$  and Gaussian in nature with widths depending upon  $k_T$ .

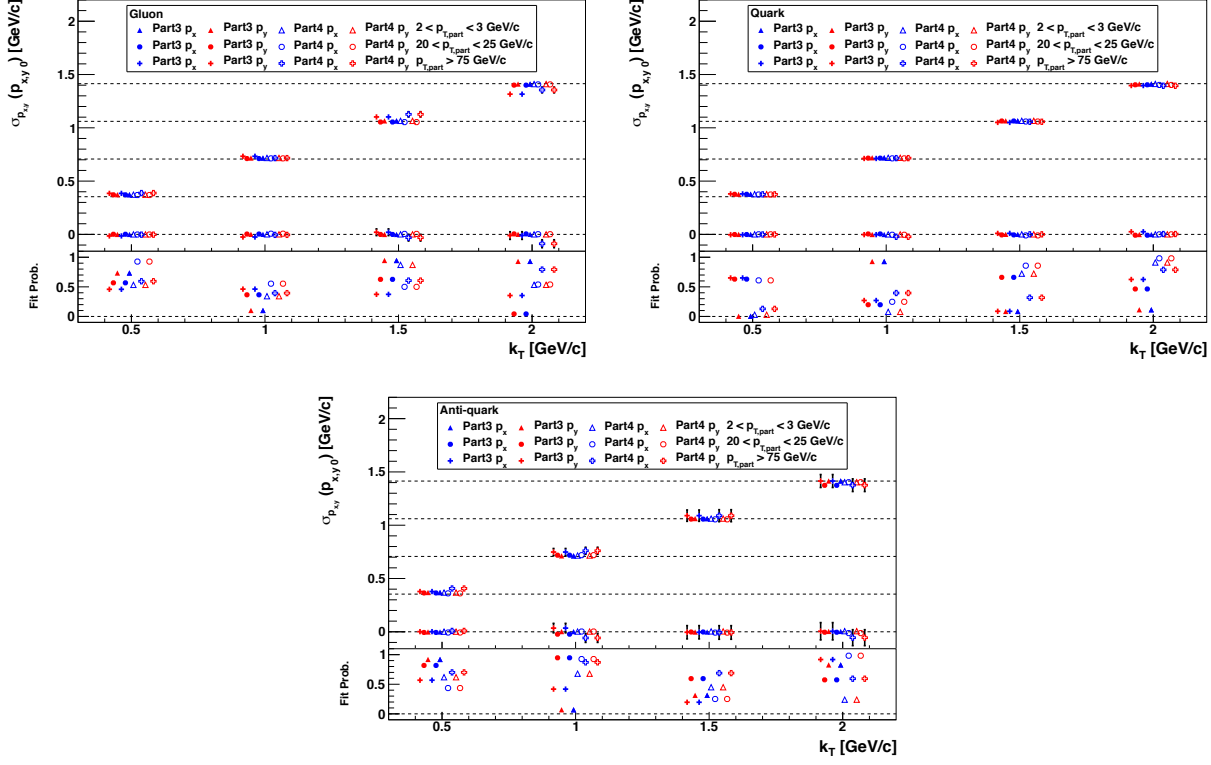


FIG. 5. Widths, centroids, and  $\chi^2$ -probabilities for Gaussian fits to  $p_x$  and  $p_y$  distributions of PYTHIA particles 3 and 4 for three bins of partonic  $p_T$ . Results are shown separately for gluons, quarks, and anti-quarks.  $\chi^2$  probabilities are generally acceptable, and centroids are all consistent with zero. The widths follow the pattern of  $\sigma = k_T/\sqrt{2}$ , shown by dashed lines.

robust fix is currently being implemented for the runs 11-14 trigger simulator. The present analysis proceeds as-is with systematics assigned to cover the issue.

The way ROOT calculates the means, the averages in Fig. 7 should be 0.5; while they are observed to be 0.5843. Since there are 25 trigger patches in a jet patch, one can estimate the average simulated jet-patch sum to be larger than the hardware sum by  $0.0843 \times 25 = 2.1$ . This should be an underestimate, since the mean value is pulled down by the masked hot towers.

Figure 8 shows the  $\chi^2$  probabilities for constant fits to data-to-embedding ratios. The probabilities are plotted as a function of integer increments to the nominal trigger threshold and separated into the different jet-patch triggers. One observes that JP0 and JP2 strongly

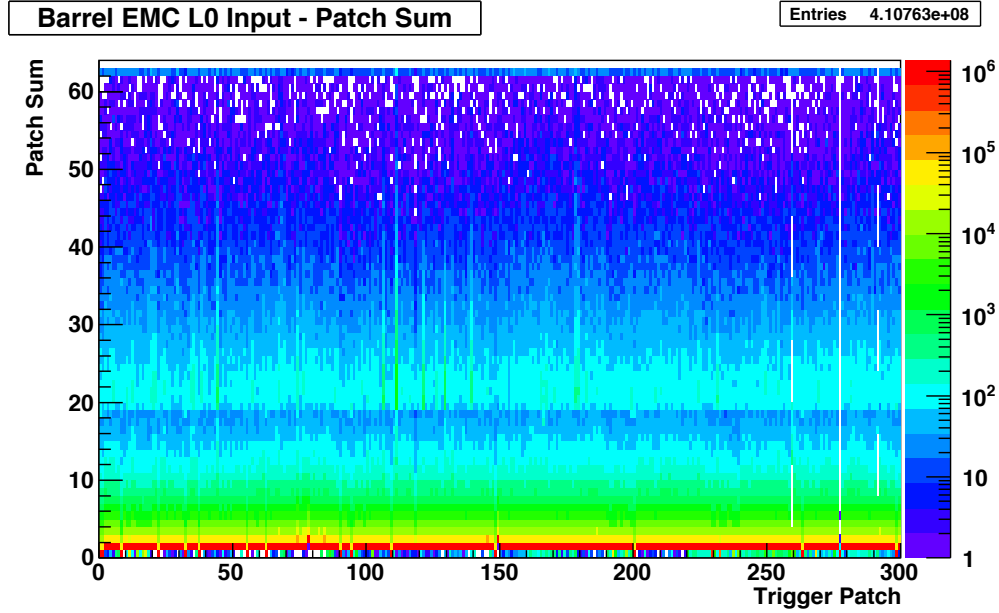


FIG. 6. L0 monitoring plot for run 1209002, from March 31, 2011. While most of the patches show pedestals of 1, a few show pedestals of 0. The effect of the zero pedestals is to raise the threshold of the trigger.

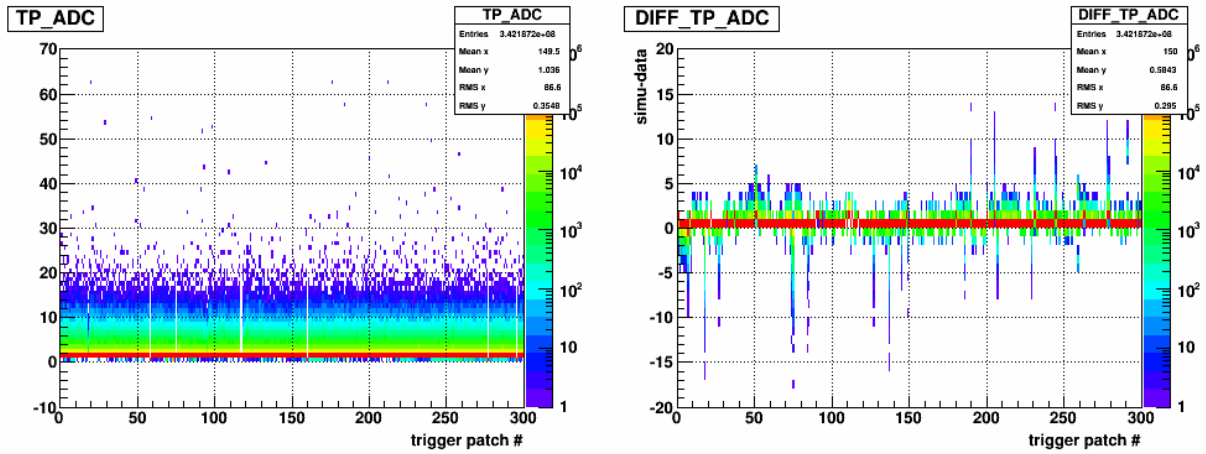


FIG. 7. An example from 2012 of the (left) FEE simulator response and (right) the difference between the hardware and simulated FEE response. There are  $\sim 20$  channels that nearly always read one count higher in the simulator than the hardware.

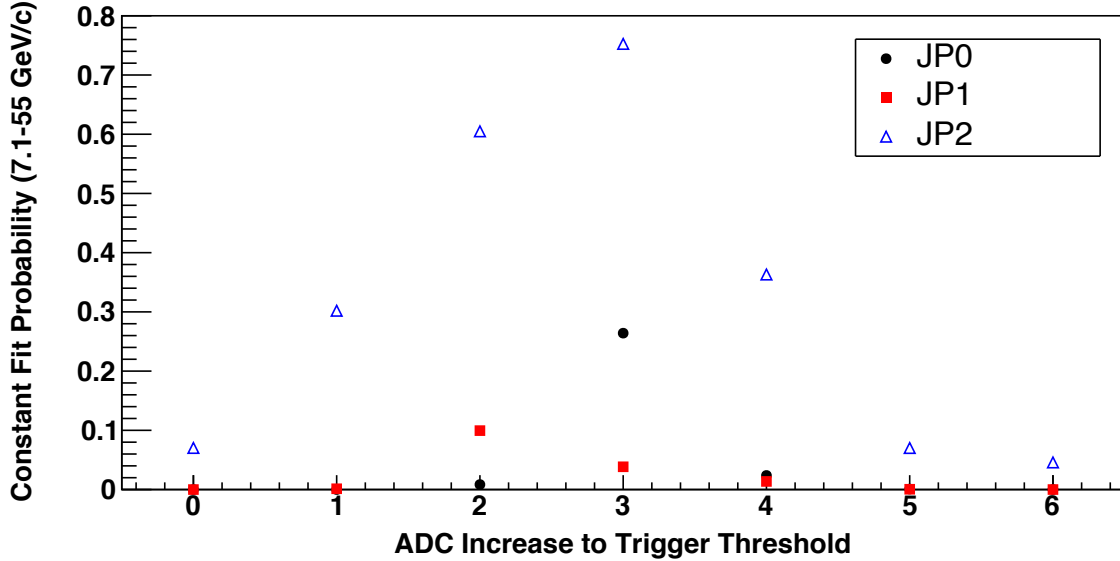


FIG. 8. The  $\chi^2$  probability for constant fits to the ratios of data-to-embedding  $p_T$  distributions. The distributions are fit across the full range of active bins for the relevant trigger. The fit probability is shown as a function of increment to the trigger threshold. JP0 and JP2 prefer an increment of 3 while JP1 prefers an increment of 2.

prefer an increment of three, while JP1 prefers an increment of, perhaps, closer to 2. This is qualitatively consistent with the expectation from the above back-of-the-envelope estimate.

In Fig. 9 the comparison of data to embedding is shown for the various jet-patch triggers, each with the nominal trigger threshold in simulation and a threshold incremented by three counts. The embedding distributions have been normalized to match the data event counts over the range of  $16.3 < p_T < 45$  GeV/ $c$ . One can clearly see that the incremented trigger threshold generates much more favorable comparisons. Since the cause for the hardware-simulator discrepancy is not understood, it is important to include a reasonable estimate of the associated systematic uncertainties.

### C. Minimum Bias Trigger and Level-2 Algorithm

The trigger emulator is not currently configured to simulate the VPDMB trigger. Thus, in the present analysis, satisfying VPDMB in the trigger simulator is not required for an event

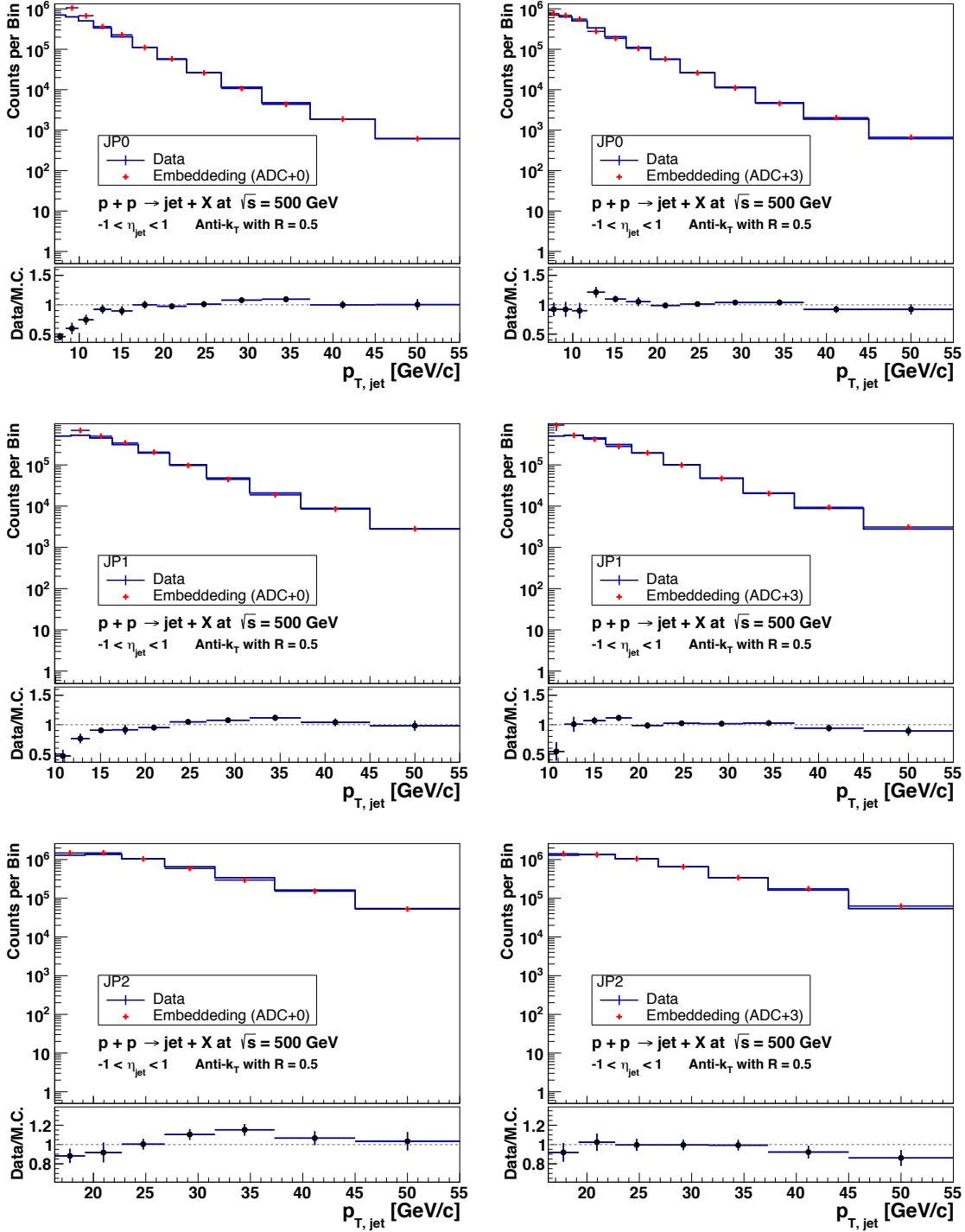


FIG. 9. Comparison of data to embedding for (top) JP0, (middle) JP1, and (bottom) JP2 triggers with (left) nominal trigger threshold and (right) incrementing the embedding trigger thresholds by three counts. Embedding distributions are normalized to match the number of data counts across the range  $16.3 < p_T < 45 \text{ GeV}/c$ .

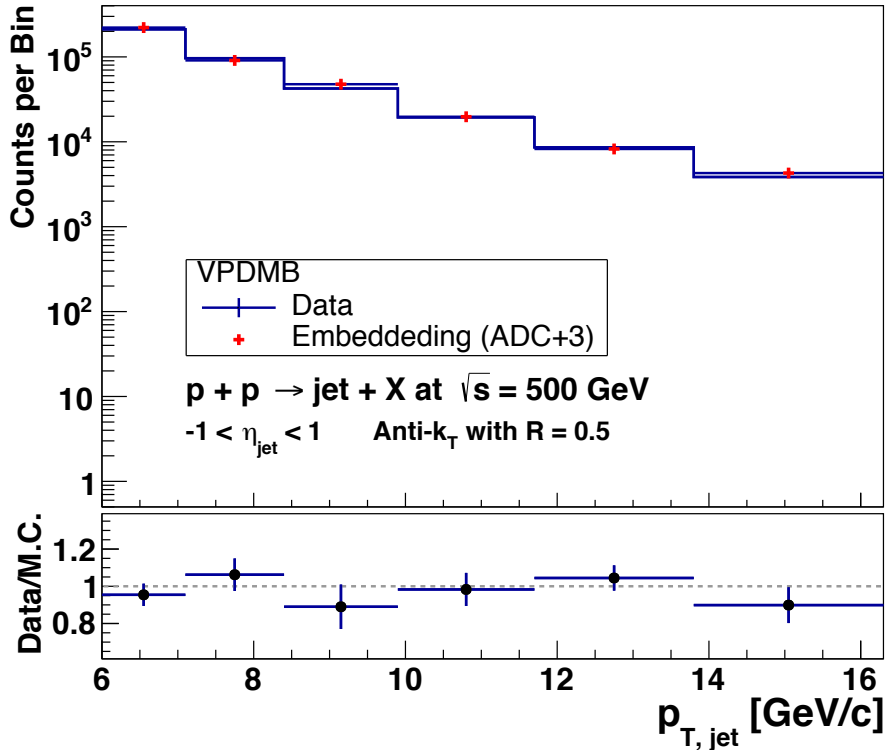


FIG. 10. Comparison of data to embedding for VPDMB events. Embedding distributions are normalized to match the number of data counts across the full range of  $p_T$ . No trigger simulation is applied for the embedding or the data.

to be assigned to VPDMB. The data require a match between the TPC vertex and the VPD vertex for a VPDMB trigger assignment. In the absence of simulated VPD vertices, this requirement is emulated in the embedding by enforcing a match between the reconstructed vertex and the simulated vertex (within 2 cm). In the embedding analysis, an additional requirement of  $p_{T,\text{jet}} < 16.3 \text{ GeV}/c$  is implemented for jets to be assigned to VPDMB. This is to avoid issues of inefficiencies at high- $p_T$  that may be present in the data but not simulated in the embedding. It is also a negligible cut, as the data yield is dominated by jet-patch triggers above  $7 - 8 \text{ GeV}/c$ . The comparison of data to embedding for VPDMB triggers is shown in Fig. 10. The shapes of the jet  $p_T$  distributions are in very good agreement.

During the 2011 transverse run, the level-2 (L2) jet algorithm was active and filtering for JP2\*L2JetHigh triggers. This algorithm filters events based on jet-like clusters of transverse

energy in the EMCs and accepts events for mono jets, dijets, or “random accept.” In the 2009  $p+p$  run, the L2 jet algorithm thresholds were strict and emulation of the algorithm was critical for proper trigger simulation. However, the thresholds were set quite low during the 2011 transverse run. For example, for runs 12046017 to 12046043 98.64% of events passed the L2 monojet filter and 98.78% of events passed any of the L2Jet filters. For runs 12097009 to 12098024 98.49% of events passed the L2 monojet filter and 98.79% passed any of the L2Jet filters [19]. Thus, the L2JetHigh filter is treated as inactive in the trigger simulator for the 2011 analysis. One can observe that perfectly reasonable agreement between data and simulation is achieved (Fig. 9), and this suggests that the effect of not including the L2JetHigh algorithm is negligible.

#### D. Data-Monte Carlo Comparisons

If simulations are to be used for corrections to data and evaluating systematic uncertainties, an important sanity-check is to compare the reconstructed simulation events to the data distributions. For the present, analysis the most important comparisons are for jet  $p_T$  and charged-particle  $z = p_\pi/p_{\text{jet}}$  and  $j_T$ , the charged-particle  $p_T$  relative to the jet axis.

The jet  $p_T$  distributions are shown in Figs. 9 and 10. One can see that for VPDMB and jet-patch triggers with the augmented trigger thresholds, the comparisons are quite nice over the full range of  $p_T$ . The lone exception would appear to be the first active bin of JP1 ( $9.9 < p_T < 11.7 \text{ GeV}/c$ ) which may simply be an unlucky fluctuation, given the limited embedding statistics, in particular, near the trigger threshold.

The distributions for pion  $z$  and  $j_T$  are shown in Fig. 11. Comparisons, again, are quite good until the kinematic limits, where statistics begin to run thin. For the present analysis, the most interesting regions of interest are  $0.1 < z < 0.3$  and  $j_T \sim 0.3 \text{ GeV}/c$ . Here, we find perfectly reasonable agreement between data and embedding with statistics that are more than adequate.

## VIII. SYSTEMATICS

Many of the systematic uncertainties for the present analysis overlap with previous jet analyses. The present analysis makes liberal use of the techniques developed for the 2009

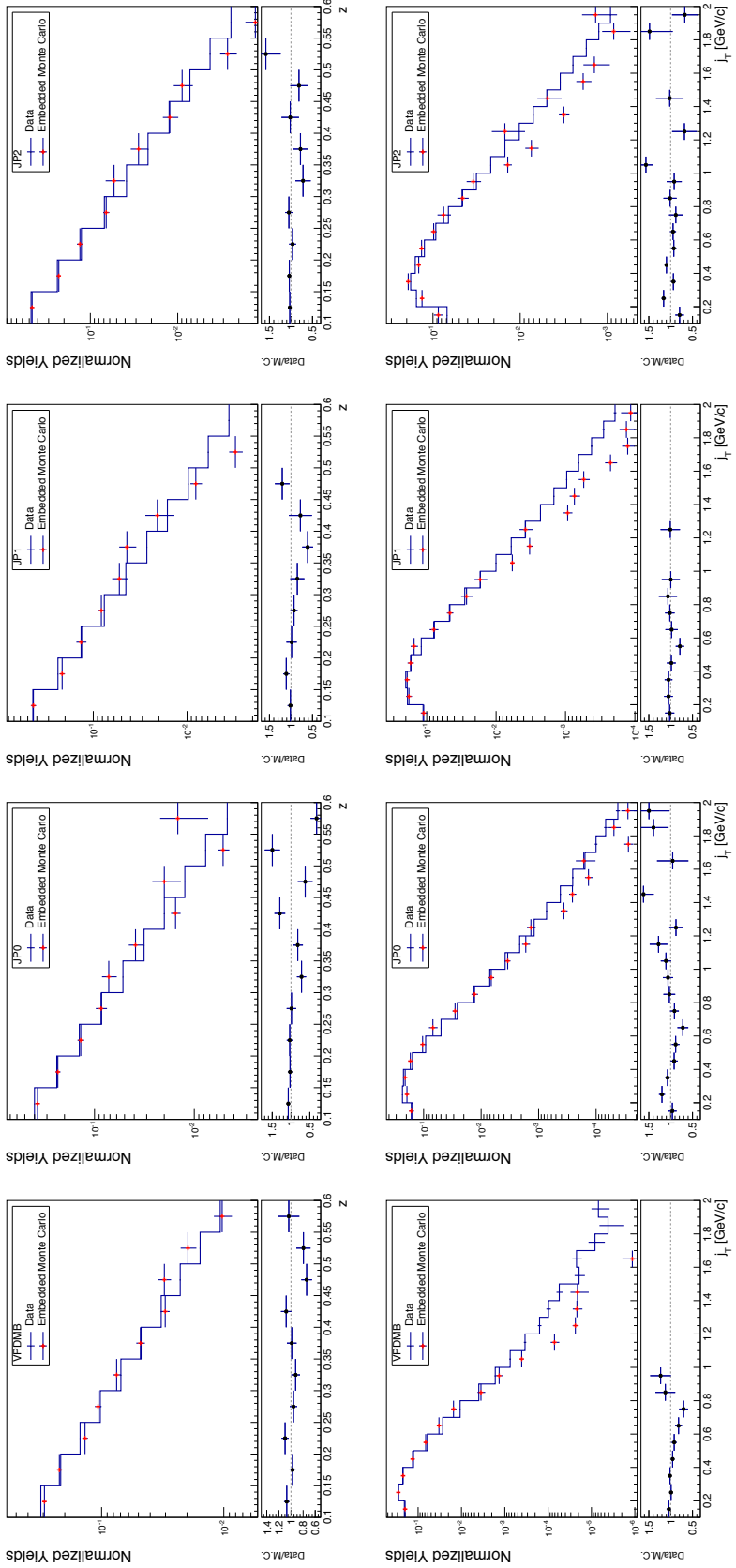


FIG. 11. Comparison of data to embedding for VPDMB, JP0, JP1, and JP2 triggers with embedding jet-patch trigger thresholds incremented by three counts. All distributions are normalized to unity.

[11], 2006 [20, 21], and earlier inclusive jet analyses.

### A. Kinematic Shifts

The reconstructed kinematics of jets and their hadrons can be shifted from the true values, due to such things as finite resolutions and reconstruction inefficiencies. To estimate these effects jets were reconstructed in the embedding simulations not only at the detector level (equivalent to the data) but also at the PYTHIA parton-jet and particle-jet levels. “Detector jets” are formed by running the jet algorithms on EMC towers and TPC tracks, as in the data. “Particle jets” are formed by running the jet algorithms on stable, hadronized, final-state particles from the PYTHIA record. “Parton jets” are formed by running the jet algorithms on fragmented partons from the PYTHIA record, excluding those from beam remnant and underlying event. Detector Jets could then be associated with those at the particle-jet and parton-jet levels and their respective kinematics compared. With this information detector-level kinematics can be corrected to their underlying, “true” values.

For the present analysis, detector jets in embedding are only analyzed for those associated with a particle-jet and a parton-jet in the event (“matched jets”). The association is defined as

$$\sqrt{(\eta_{\text{det. jet}} - \eta_{\text{part. jet}})^2 + (\phi_{\text{det. jet}} - \phi_{\text{part. jet}})^2} < 0.5. \quad (6)$$

Similarly, tracks from matched detector-jets are associated with particles at the particle-jet level. In the end, jet and pion kinematics are corrected back to their values at the particle-jet level. A summary of the corrected mean values of jet  $p_T$ , pion  $z$ , and pion  $j_T$  is presented bin-by-bin in Fig. 12.

#### 1. Jet $p_T$ Correction

For the jet  $p_T$  correction,  $\langle p_{T,\text{particle}} - p_{T,\text{detector}} \rangle$  is calculated from the embedding for each bin, trigger-by-trigger. These values are, then, added to  $\langle p_{T,\text{data}} \rangle$  to estimate the “true” jet  $p_T$  for the relevant trigger. The uncertainties from the embedding statistics are calculated

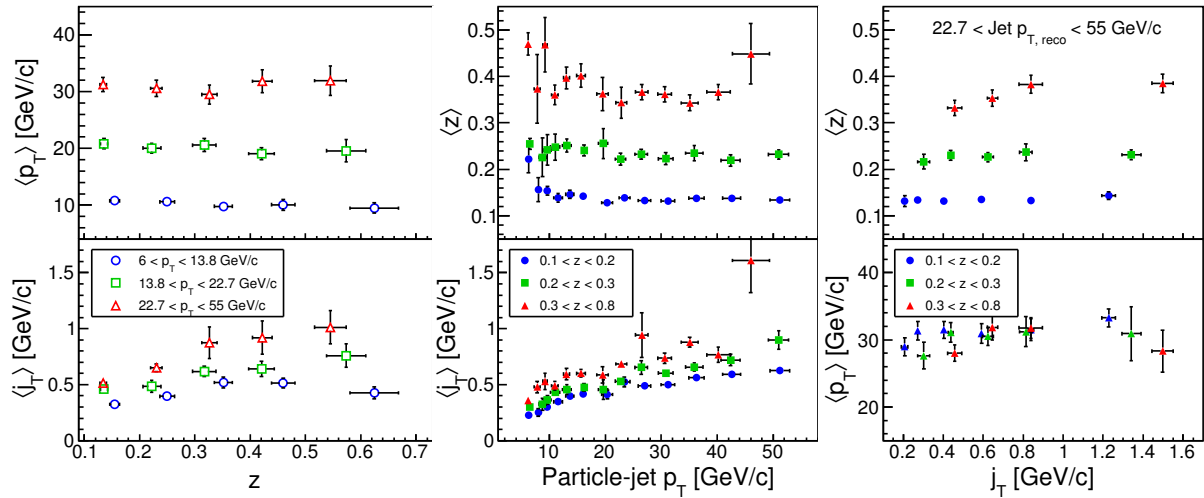


FIG. 12. A bin-by-bin summary of the mean kinematics for pions within jets. Kinematics are corrected to the PYTHIA particle-jet level. Events are separated into low (blue), mid (green), and high (red) pion- $z$  in the middle and right panels and jet  $p_T$  in the left panels. Uncertainties combine contributions from Monte Carlo statistics and systematic uncertainties.

as

$$\sigma_{p_T} = \frac{1}{\sum_i w_i} \times \sqrt{\sum_i w_i^2 \delta p_{T,i}^2 - 2\langle \delta p_T \rangle \sum_i w_i^2 \delta p_{T,i} + \langle \delta p_T \rangle^2 \sum_i w_i^2}. \quad (7)$$

This is critical to do by hand, as ROOT does not calculate the correct uncertainty on a weighted average, such as you find from a TProfile with weighted events. For each bin, the average corrected  $p_T$  is calculated by using the fractions each trigger contributes to the bin in the data. The statistical uncertainty is taken as that of the dominant trigger for the bin. This is done because in the simulation, events are associated with any and all triggers satisfied. Thus, the samples for each trigger are correlated, and removing the correlation piece from the statistical uncertainty is non-trivial. The present technique avoids the issue. Finally, the distribution of  $p_{T,\text{particle}}$  vs.  $p_{T,\text{detector}}$  is fitted with a quadratic. The fit is done over two separate  $p_T$  ranges:  $7.1 < p_{T,\text{detector}} < 16.3 \text{ GeV}/c$  and  $16.3 < p_{T,\text{detector}} < 55 \text{ GeV}/c$ . These correspond to the ranges where JP2 is inactive and active, respectively. The  $6 - 7.1 \text{ GeV}/c$  bin is solely VPDMB and is not included in the fit. Its corrected value is taken from the raw calculations, described above. For the bins with active jet-patch triggers, the fitted  $p_{T,\text{particle}}$  values are taken as the final, corrected values. The uncertainties, which

depend upon the covariance matrix,  $C$ , are

$$\begin{aligned}\sigma_{p_T}^2 = & C(0,0) + C(1,1)p_{T,\text{detector}}^2 + C(2,2)p_{T,\text{detector}}^4 \\ & + 2[C(0,1)p_{T,\text{detector}} + C(0,2)p_{T,\text{detector}}^2 + C(1,2)p_{T,\text{detector}}^3],\end{aligned}\quad (8)$$

which is just Eq. 7.27 in Bevington [22].

The systematic uncertainties associated with the shift in  $p_T$  are related to uncertainties in the EMC gains, the EMC response to charged particles, TPC tracking efficiencies, and uncertainties in the trigger emulator. Some of the involved quantities are summarized in Table VI. Many of these are based upon Refs. [23] and [24]. The BEMC gain uncertainty is chosen as 6.7%. This assumes a linear change from year-to-year with an observation of 3.7% from 2009 and a change of 4.2% from 2009 to 2012. First, the relative uncertainty from the BEMC energy scale,  $\sigma_{\text{BEMC scale}}$ , is estimated by combining the BEMC gain and efficiency uncertainties in quadrature. The total BEMC fractional uncertainty is

$$\frac{\sigma_{\text{BEMC tot}}}{p_{T,\text{jet}}} = R_T \times \sigma_{\text{BEMC scale}}, \quad (9)$$

where  $R_T$  is the observed neutral energy fraction. The relative uncertainty from the BEMC related to tracking is

$$\sigma_{\text{BEMC track}} = [S_{\text{neutral hadrons}} - (f_{\text{proj. tow.}} \mathcal{E}_{\text{track}})] \times \left( \mathcal{R}_{\text{BEMC track}} \frac{\sigma_{\mathcal{R}}}{\mathcal{E}_{\text{track}}} \right), \quad (10)$$

where  $S_{\text{neutral hadrons}}$  is the scale-up correction for neutral hadrons,  $f_{\text{proj. tow.}}$  is the fraction of a track deposited in the projected tower,  $\mathcal{E}_{\text{track}}$  is the tracking efficiency, and  $\mathcal{R}_{\text{BEMC track}}$  is the BEMC track response. The total BEMC track fractional uncertainty is estimated from

$$\begin{aligned}\left( \frac{\sigma_{\text{tot BEMC track}}}{p_{T,\text{jet}}} \right)^2 = & [(1 - R_T) * \sigma_{p_{\text{track}}}]^2 \\ & + \{\text{Max}[(1 - R_T), f_{\text{min. neutral}}] \times \sigma_{\text{BEMC track}}\}^2,\end{aligned}\quad (11)$$

where  $p_{T,\text{track}}$  is the fractional track momentum uncertainty and  $f_{\text{min. neutral}}$  is the minimum track fraction for neutral particles. Finally, the total uncertainty from the shift in the reconstructed  $p_T$  is estimated by combining in quadrature three quantities: the statistical uncertainty on the true  $p_T$  (Eq. 8), the change in the calculated true  $p_T$  when 7% of tracks are randomly rejected, and the change in the calculated true  $p_T$  when the nominal trigger thresholds are used in the simulation. The shifts and uncertainties are calculated separately

Contribution	Value
BEMC gain uncertainty	6.7%
BEMC efficiency uncertainty	1%
Track momentum uncertainty	1%
BEMC response to tracks	30%
BEMC track response uncertainty	9%
Track efficiency	65%
Fraction of track deposited in projected tower	0.5
Correction for neutral hadrons	1/0.86
Minimum track fraction for neutrals	0.5

TABLE VI. Various quantities contributing to the uncertainty in the values of the corrected kinematic variables. The BEMC response to tracks, its corresponding uncertainty, and the correction for neutral hadrons are chosen based on Ref. [23]. The tracking efficiency is an educated guess, based on Ref. [24]. The fraction of tracks deposited in a projected tower is a conservative estimate.

for jets produced with  $|\eta| < 0.5$  and  $0.5 < |\eta| < 1$  and their values are summarized in Tables VII and VIII, respectively.

The corrected jet  $p_T$  is also calculated for pions. The jet  $p_T$  is estimated in bins of pion  $z$ :  $0.1 < z < 0.2$ ,  $0.2 < z < 0.3$ , and  $0.3 < z < 0.8$ , denoted “low- $z$ ”, “mid- $z$ ,” and “high- $z$ ,” respectively. The results are summarized in Tables IX, X, and XI.

## 2. Pion $z$ Correction

The correction for pion  $z = p_\pi/p_{\text{jet}}$  is similar to that of the jet  $p_T$ , as described in Section VIII A 1. First, the “true”  $z$  is calculated by evaluating the underlying PYTHIA particles for reconstructed pions within jets. The detector-jets are required to match to particle-jets and parton-jets at the PYTHIA level, and the reconstructed pions are required to match to a particle at the PYTHIA level. The corrections are calculated trigger-by-trigger and averaged based upon the trigger yields in the data. The associated uncertainty is taken as that of the dominant trigger for the relevant bin. After the bin-by-bin uncertainties are calculated,

Bin Range [GeV/c]	Detect.-jet $p_T$ [GeV/c]	$R_T$	BEMC Rel. Uncert.	Track Rel. Uncert.	$p_T$ -shift Rel. Uncert.	Tot. Rel. Uncert.	Particle-jet $p_T$ [GeV/c]
6.0 – 7.1	6.47	0.302	2.0%	2.5%	1.9%	3.8%	6.34 ± 0.24
7.1 – 8.4	7.72	0.549	3.7%	1.8%	4.3%	6.0%	8.27 ± 0.46
8.4 – 9.9	9.10	0.531	3.6%	1.8%	3.8%	5.5%	9.70 ± 0.50
9.9 – 11.7	10.76	0.569	3.9%	1.8%	4.2%	5.9%	11.46 ± 0.64
11.7 – 13.8	12.68	0.538	3.6%	1.8%	3.7%	5.5%	13.54 ± 0.70
13.8 – 16.3	14.94	0.498	3.4%	1.8%	3.2%	5.0%	16.06 ± 0.74
16.3 – 19.2	17.72	0.624	4.2%	1.8%	3.0%	5.5%	20.11 ± 0.97
19.2 – 22.7	20.85	0.577	3.9%	1.8%	2.5%	5.0%	23.2 ± 1.0
22.7 – 26.8	24.56	0.524	3.5%	1.8%	2.4%	4.7%	27.0 ± 1.1
26.8 – 31.6	28.90	0.479	3.2%	1.9%	2.4%	4.4%	31.3 ± 1.3
31.6 – 37.3	34.03	0.447	3.0%	2.0%	2.1%	4.2%	36.4 ± 1.4
37.3 – 45.0	40.39	0.425	2.9%	2.1%	1.7%	3.9%	42.7 ± 1.6
45.0 – 55.0	48.77	0.414	2.8%	2.1%	1.7%	3.9%	50.9 ± 1.9

TABLE VII. Corrected jet  $p_T$  and uncertainties with their various contributions for  $|\eta_{\text{jet}}| < 0.5$ .

Bin Range [GeV/c]	Detect.-jet $p_T$ [GeV/c]	$R_T$	BEMC Rel. Uncert.	Track Rel. Uncert.	$p_T$ -shift Rel. Uncert.	Tot. Rel. Uncert.	Particle-jet $p_T$ [GeV/c]
6.0 – 7.1	6.47	0.294	2.0%	2.6%	1.9%	3.8%	6.34 ± 0.24
7.1 – 8.4	7.72	0.532	3.6%	1.8%	4.5%	6.0%	8.28 ± 0.47
8.4 – 9.9	9.10	0.509	3.5%	1.8%	2.9%	4.8%	9.72 ± 0.44
9.9 – 11.7	10.76	0.548	3.7%	1.8%	2.9%	5.1%	11.48 ± 0.55
11.7 – 13.8	12.68	0.514	3.5%	1.8%	2.8%	4.8%	13.56 ± 0.61
13.8 – 16.3	14.94	0.476	3.2%	1.9%	3.2%	5.0%	16.07 ± 0.74
16.3 – 19.2	17.71	0.595	4.0%	1.8%	2.9%	5.3%	20.12 ± 0.94
19.2 – 22.7	20.83	0.546	3.7%	1.8%	2.5%	4.8%	23.3 ± 1.0
22.7 – 26.8	24.55	0.496	3.4%	1.8%	2.4%	4.5%	27.0 ± 1.1
26.8 – 31.6	28.89	0.457	3.1%	2.0%	2.4%	4.4%	31.3 ± 1.3
31.6 – 37.3	34.01	0.430	2.9%	2.1%	2.1%	4.2%	36.4 ± 1.4
37.3 – 45.0	40.35	0.414	2.8%	2.1%	1.7%	3.9%	42.6 ± 1.6
45.0 – 55.0	48.75	0.410	2.8%	2.1%	1.7%	3.9%	50.9 ± 1.9

TABLE VIII. Corrected jet  $p_T$  and uncertainties with their various contributions for  $0.5 < |\eta_{\text{jet}}| < 1$ .

Bin Range	Detect.-jet	$R_T$	BEMC Rel.	Track Rel.	$p_T$ -shift Rel.	Tot. Rel.	Particle-jet $p_T$
[GeV/c]	$p_T$ [GeV/c]		Uncert.	Uncert.	Uncert.	Uncert.	[GeV/c]
6.0 – 7.1	6.47	0.324	2.2%	2.4%	2.5%	4.1%	6.24 ± 0.27
7.1 – 8.4	7.73	0.473	3.2%	1.9%	5.6%	6.7%	7.99 ± 0.52
8.4 – 9.9	9.11	0.456	3.1%	2.0%	5.7%	6.8%	9.63 ± 0.62
9.9 – 11.7	10.77	0.513	3.5%	1.8%	6.1%	7.3%	11.52 ± 0.78
11.7 – 13.8	12.69	0.469	3.2%	1.9%	4.8%	6.0%	13.63 ± 0.77
13.8 – 16.3	14.95	0.447	3.0%	2.0%	2.3%	4.3%	16.01 ± 0.64
16.3 – 19.2	17.73	0.564	3.8%	1.8%	3.6%	5.5%	20.34 ± 0.98
19.2 – 22.7	20.86	0.523	3.5%	1.8%	2.9%	4.9%	23.4 ± 1.0
22.7 – 26.8	24.56	0.458	3.1%	2.0%	2.6%	4.5%	27.0 ± 1.1
26.8 – 31.6	28.90	0.419	2.8%	2.1%	2.5%	4.3%	31.2 ± 1.2
31.6 – 37.3	34.00	0.405	2.7%	2.2%	2.3%	4.2%	36.3 ± 1.4
37.3 – 45.0	40.33	0.382	2.6%	2.2%	1.9%	3.9%	42.6 ± 1.6
45.0 – 55.0	48.70	0.336	2.3%	2.4%	1.5%	3.6%	51.2 ± 1.8

TABLE IX. Corrected jet  $p_T$  and uncertainties with their various contributions for pions with  $0.1 < z < 0.2$ .

Bin Range	Detect.-jet	$R_T$	BEMC Rel.	Track Rel.	$p_T$ -shift Rel.	Tot. Rel.	Particle-jet $p_T$
[GeV/c]	$p_T$ [GeV/c]		Uncert.	Uncert.	Uncert.	Uncert.	[GeV/c]
6.0 – 7.1	6.46	0.280	1.9%	2.6%	2.2%	3.9%	6.50 ± 0.25
7.1 – 8.4	7.72	0.443	3.0%	2.0%	7.8%	8.6%	8.75 ± 0.66
8.4 – 9.9	9.11	0.422	2.9%	2.1%	6.2%	7.1%	9.62 ± 0.65
9.9 – 11.7	10.77	0.465	3.2%	1.9%	6.9%	7.8%	11.00 ± 0.84
11.7 – 13.8	12.69	0.411	2.8%	2.1%	5.5%	6.5%	13.09 ± 0.82
13.8 – 16.3	14.95	0.397	2.7%	2.2%	2.5%	4.2%	16.18 ± 0.63
16.3 – 19.2	17.74	0.510	3.5%	1.8%	2.6%	4.7%	19.61 ± 0.84
19.2 – 22.7	20.87	0.496	3.4%	1.8%	2.1%	4.3%	22.72 ± 0.91
22.7 – 26.8	24.57	0.453	3.1%	2.0%	2.6%	4.5%	26.4 ± 1.1
26.8 – 31.6	28.89	0.412	2.8%	2.1%	3.0%	4.6%	30.8 ± 1.3
31.6 – 37.3	34.00	0.384	2.6%	2.2%	3.0%	4.6%	35.9 ± 1.6
37.3 – 45.0	40.30	0.359	2.4%	2.3%	2.5%	4.2%	42.4 ± 1.7
45.0 – 55.0	48.67	0.316	2.1%	2.5%	1.7%	3.7%	51.0 ± 1.8

TABLE X. Corrected jet  $p_T$  and uncertainties with their various contributions for pions with  $0.2 < z < 0.3$ .

Bin Range	Detect.-jet	$R_T$	BEMC Rel.	Track Rel.	$p_T$ -shift Rel.	Tot. Rel.	Particle-jet $p_T$
[GeV/c]	$p_T$ [GeV/c]		Uncert.	Uncert.	Uncert.	Uncert.	[GeV/c]
6.0 – 7.1	6.46	0.228	1.5%	2.8%	2.0%	3.8%	$6.19 \pm 0.24$
7.1 – 8.4	7.71	0.337	2.3%	2.4%	6.4%	7.2%	$7.80 \pm 0.55$
8.4 – 9.9	9.11	0.350	2.4%	2.4%	3.4%	4.7%	$9.20 \pm 0.43$
9.9 – 11.7	10.76	0.432	2.9%	2.1%	4.0%	5.4%	$10.94 \pm 0.58$
11.7 – 13.8	12.69	0.303	2.1%	2.5%	3.2%	4.6%	$13.04 \pm 0.58$
13.8 – 16.3	14.95	0.352	2.4%	2.3%	4.2%	5.3%	$15.64 \pm 0.80$
16.3 – 19.2	17.72	0.430	2.9%	2.1%	4.4%	5.7%	$19.5 \pm 1.0$
19.2 – 22.7	20.87	0.445	3.0%	2.0%	3.0%	4.7%	$22.8 \pm 1.0$
22.7 – 26.8	24.58	0.433	2.9%	2.1%	2.5%	4.3%	$26.5 \pm 1.1$
26.8 – 31.6	28.91	0.353	2.4%	2.3%	2.6%	4.2%	$30.6 \pm 1.2$
31.6 – 37.3	34.02	0.368	2.5%	2.3%	3.0%	4.5%	$35.1 \pm 1.5$
37.3 – 45.0	40.32	0.330	2.2%	2.4%	4.0%	5.1%	$40.2 \pm 2.1$
45.0 – 55.0	48.64	0.272	1.8%	2.6%	5.9%	6.8%	$46.0 \pm 3.3$

TABLE XI. Corrected jet  $p_T$  and uncertainties with their various contributions for pions with  $0.3 < z < 0.8$ .

the “true” vs. “reconstructed” distribution is fit with a quadratic, and the uncertainties are calculated using the form of Eq. 8 for  $z$  rather than jet  $p_T$ . Further, the data are binned in terms of reconstructed jet  $p_T$ :  $6 < p_T < 13.8 \text{ GeV}/c$ ,  $13.8 < p_T < 22.7 \text{ GeV}/c$ , and  $22.7 < p_T < 55 \text{ GeV}/c$ , defined as “low,” “medium,” and “high”  $p_T$ , respectively.

For the systematic uncertainties, the pion  $z$  has contributions from both the track momentum resolution and the jet momentum resolution, since

$$\left(\frac{\sigma_z}{z}\right)^2 = \left(\frac{\sigma_{p_\pi}}{p_\pi}\right)^2 + \left(\frac{\sigma_{p_{\text{jet}}}}{p_{\text{jet}}}\right)^2, \quad (12)$$

Uncertainties due to the jet energy scale are described at length in Section VIII A 1. The Track momentum uncertainty is taken as 1%, as described in Table VI. As with the jet  $p_T$  shifts, the final systematic is taken as the quadrature sum of the jet BEMC scale uncertainty, the jet scale uncertainty due to tracks, the  $z$  shift uncertainty (including the differences between the 0% and 7% track rejection and ADC+3 and ADC+0 trigger thresholds), and the addition of the single track momentum uncertainty. The results are summarized in Tables XII, XIII, and XIV.

### 3. Pion $j_T$ Correction

The correction for pion  $j_T$  follows the same logic as the jet  $p_T$  and pion  $z$  corrections, save the quadratic fit to “true” vs. “reconstructed” that does not produce a reasonable  $\chi^2$ . Since  $j_T$  is simply the pion  $p_T$  calculated from the NLS coordinates, i.e. relative to the jet axis, the jet energy scale uncertainty does not play a role. Instead, the systematic is estimated by the quadrature sum of the  $j_T$ -shift uncertainty (including the 0% vs. 7% track rejection and ADC+3 vs. ADC+0 trigger thresholds) and the track momentum uncertainty,  $j_{T, \text{reco.}} \times \sigma_{p_{T, \text{track}}}$ . The  $j_T$  data are binned in terms of both jet  $p_T$  (“low,” “mid,” and “high”) and pion  $z$ :  $0.1 < z < 0.2$ ,  $0.2 < z < 0.3$ , and  $0.3 < z < 0.8$ . The results are summarized in Tables XV, XVI, and XVII.

## B. Generator-level Associations

In particular at low  $p_T$  there is a non-negligible probability that a reconstructed jet arose not from the hard scattering process but either from the underlying event or from

Bin Range	$z_{\text{reco.}}$	$R_T$	BEMC Rel.	Track Rel.	$z$ -shift Rel.	Tot. Rel.	Particle-level $z$
			Uncert.	Uncert.	Uncert.	Uncert.	
0.1 – 0.2	0.142	0.471	3.2%	1.9%	4.9%	6.2%	$0.1552 \pm 0.0088$
0.2 – 0.3	0.242	0.415	2.8%	2.1%	3.9%	5.4%	$0.250 \pm 0.013$
0.3 – 0.4	0.342	0.377	2.6%	2.3%	3.1%	4.7%	$0.352 \pm 0.016$
0.4 – 0.5	0.443	0.289	2.0%	2.6%	3.5%	4.9%	$0.460 \pm 0.022$
0.5 – 0.8	0.585	0.216	1.5%	2.8%	6.7%	7.5%	$0.625 \pm 0.044$

TABLE XII. Corrected pion  $z$  and uncertainties with their various contributions for  $6 < p_{T,\text{jet}} < 13.8 \text{ GeV}/c$ .

Bin Range	$z_{\text{reco.}}$	$R_T$	BEMC Rel.	Track Rel.	$z$ -shift Rel.	Tot. Rel.	Particle-level $z$
			Uncert.	Uncert.	Uncert.	Uncert.	Uncert.
0.1 – 0.2	0.139	0.523	3.5%	1.8%	2.3%	4.7%	$0.1355 \pm 0.0066$
0.2 – 0.3	0.240	0.480	3.3%	1.9%	5.5%	6.8%	$0.222 \pm 0.016$
0.3 – 0.4	0.341	0.452	3.1%	2.0%	5.1%	6.3%	$0.317 \pm 0.022$
0.4 – 0.5	0.441	0.366	2.5%	2.3%	3.9%	5.3%	$0.421 \pm 0.023$
0.5 – 0.8	0.576	0.273	1.9%	2.6%	5.1%	6.1%	$0.574 \pm 0.035$

TABLE XIII. Corrected pion  $z$  and uncertainties with their various contributions for  $13.8 < p_{T,\text{jet}} < 22.7 \text{ GeV}/c$ .

Bin Range	$z_{\text{reco.}}$	$R_T$	BEMC Rel.	Track Rel.	$z$ -shift Rel.	Tot. Rel.	Particle-level $z$
			Uncert.	Uncert.	Uncert.	Uncert.	
0.1 – 0.2	0.139	0.430	2.9%	2.1%	2.2%	4.3%	$0.1340 \pm 0.0060$
0.2 – 0.3	0.241	0.421	2.9%	2.1%	2.3%	4.3%	$0.231 \pm 0.010$
0.3 – 0.4	0.341	0.419	2.8%	2.1%	1.9%	4.1%	$0.326 \pm 0.014$
0.4 – 0.5	0.441	0.318	2.2%	2.5%	2.2%	4.1%	$0.422 \pm 0.018$
0.5 – 0.8	0.570	0.265	1.8%	2.7%	3.8%	5.0%	$0.545 \pm 0.029$

TABLE XIV. Corrected pion  $z$  and uncertainties with their various contributions for  $22.7 < p_{T,\text{jet}} < 55 \text{ GeV}/c$ .

Bin Range [GeV/c]	$j_T$ , reco.	Track Rel. Uncert.	$j_T$ -shift Rel. Uncert.	Tot. Rel. Uncert.	Particle-level $j_T$
0.1 – 0.2	0.168	1.0%	9.7%	9.8%	$0.207 \pm 0.016$
0.2 – 0.3	0.253	1.0%	2.3%	2.5%	$0.2727 \pm 0.0064$
0.3 – 0.5	0.395	1.0%	1.5%	1.8%	$0.4035 \pm 0.0070$
0.5 – 0.7	0.590	1.0%	1.1%	1.5%	$0.5916 \pm 0.0087$
0.7 – 1.0	0.826	1.0%	1.2%	1.6%	$0.839 \pm 0.013$
1.0 – 2.0	1.239	1.0%	2.5%	2.7%	$1.228 \pm 0.033$

TABLE XV. Corrected pion  $j_T$  and uncertainties with their various contributions for  $22.7 < p_{T, \text{jet}} < 55 \text{ GeV}/c$  and  $0.1 < z < 0.2$ .

Bin Range [GeV/c]	$j_T$ , reco.	Track Rel. Uncert.	$j_T$ -shift Rel. Uncert.	Tot. Rel. Uncert.	Particle-level $j_T$
0.2 – 0.3	0.266	1.0%	11.2%	11.3%	$0.303 \pm 0.030$
0.3 – 0.5	0.402	1.0%	2.8%	3.0%	$0.437 \pm 0.012$
0.5 – 0.7	0.592	1.0%	4.7%	4.8%	$0.624 \pm 0.028$
0.7 – 1.0	0.827	1.0%	3.5%	3.7%	$0.813 \pm 0.030$
1.0 – 2.0	1.302	1.0%	3.5%	3.6%	$1.341 \pm 0.047$

TABLE XVI. Corrected pion  $j_T$  and uncertainties with their various contributions for  $22.7 < p_{T, \text{jet}} < 55 \text{ GeV}/c$  and  $0.2 < z < 0.3$ .

pile-up backgrounds. Underlying event contributions are demonstrated in Fig. 13 for jets with a parameter of  $R = 0.6$ . One can see that especially at low partonic  $p_T$  and low jet  $p_T$  there is a sizable probability that the PYTHIA particle jet does not match to a PYTHIA parton jet. For this purpose, a “match” is defined as an association in  $(\eta, \phi)$  space of  $\Delta R = \sqrt{(\eta_{\text{parton}} - \eta_{\text{particle}})^2 + (\phi_{\text{parton}} - \phi_{\text{particle}})^2} < 0.5$ . The matching probability is further degraded by such reconstruction effects as vertex misidentification and pile-up background. The situation can be somewhat mitigated by switching the  $R$  parameter from 0.6 to 0.5. Below this the degradation in statistics outweighs the gain in systematics. Thus,

Bin Range [GeV/c]	$j_T, \text{reco.}$	Track Rel. Uncert.	$j_T\text{-shift Rel.}$ Uncert.	Tot. Rel. Uncert.	Particle-level $j_T$
0.3 – 0.5	0.428	1.0%	8.1%	8.1%	$0.457 \pm 0.035$
0.5 – 0.7	0.598	1.0%	4.2%	4.3%	$0.646 \pm 0.026$
0.7 – 1.0	0.832	1.0%	6.9%	7.0%	$0.839 \pm 0.058$
1.0 – 2.0	1.306	1.0%	3.9%	4.0%	$1.498 \pm 0.053$

TABLE XVII. Corrected pion  $j_T$  and uncertainties with their various contributions for  $22.7 < p_{T,\text{jet}} < 55$  GeV/c and  $0.3 < z < 0.8$ .

for the final analysis, a parameter of  $R = 0.5$  is chosen. A summary of the matching probabilities for inclusive jet production is shown in Fig. 14 using the final parameter choice of  $R = 0.5$ . One observes that the matching probability increases steadily from around 70% at  $p_{T,\text{reco}} \sim 6$  GeV/c to approximately 97% at  $p_{T,\text{reco}} \sim 10$  GeV/c. Events are separated into the various trigger contributions and are correlated across the subsamples, as described in Section VIII A 1. One may expect that as the trigger becomes more restrictive the matching probability should increase. However, the small amount of statistics makes this difficult to observe in the present sample of Monte Carlo events. The deviations observed in the 10 GeV/c bin are likely the result of low statistics. The probabilities shown in Fig. 14 reflect the total probabilities, combining the likelihood of a mismatch between particle jets and parton jets, detector jets and particle jets, and between the reconstructed and thrown vertices. Vertex-matching probabilities typically range between  $\approx 90 - 95\%$  at the lowest  $p_{T,\text{reco}}$  and increase to unity for  $p_T > 10$  GeV/c. The vertex mismatch is eliminated entirely in VPDMB events due to the requirement of a match between the TPC and VPD vertices in data.

The parton-jet matching probabilities are also analyzed for pions within jets. Figures 15 and 16 show the probabilities as a function of reconstructed pion  $z$  for low- $p_T$  jets and detector-jet  $p_T$  in various bins of pion  $z$ . Above detector-jet  $p_T > 13.8$  GeV/c matching probabilities are consistent with unity.

For physics observables relevant for the present analysis, it is unclear what effects unassociated jets contribute. For the inclusive jet asymmetry, the pertinent mechanisms (twist-3

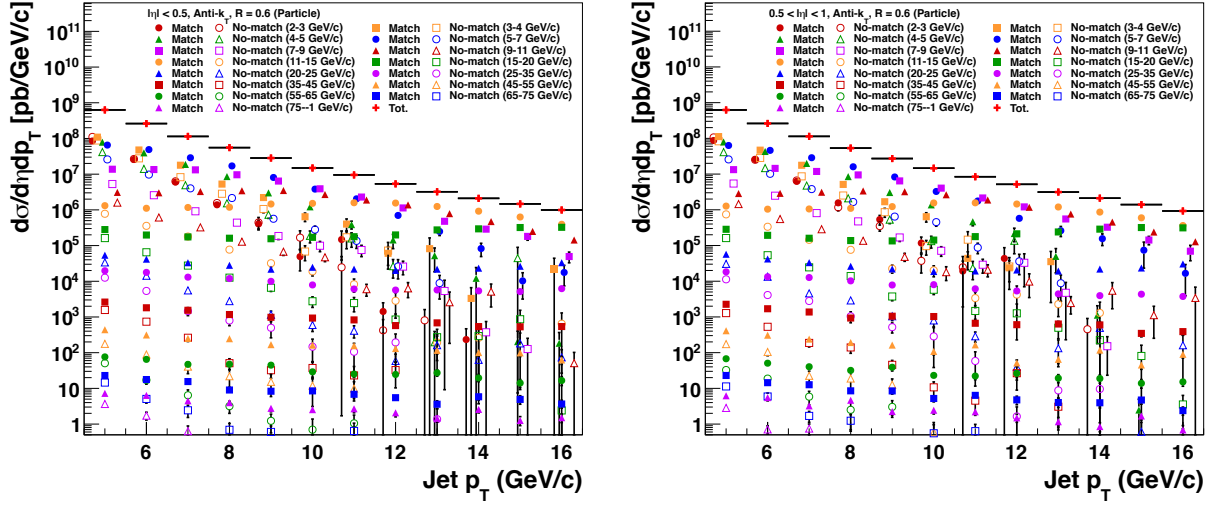


FIG. 13. PYTHIA particle-jet cross section as a function of jet  $p_T$ . Events are sorted into their partonic  $p_T$  bins and as to whether or not they match to a parton jet (defined as an match within  $\Delta R < 0.5$ ). One can see that for low partonic  $p_T$  and low jet  $p_T$  there is a sizable chance that the particle jet is not associated with a parton jet.

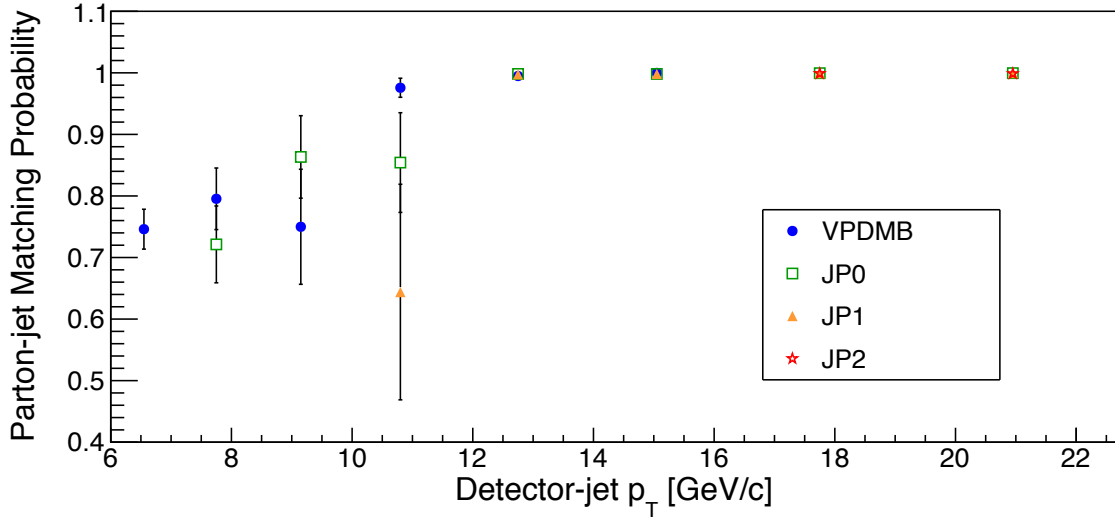


FIG. 14. Parton-jet matching probabilities as a function of detector-jet  $p_T$ . Points are plotted at the bin centers. Uncertainties are statistical. The matching probability increases with reconstructed jet  $p_T$  and is consistent with unity above  $\sim 12$  GeV/c.

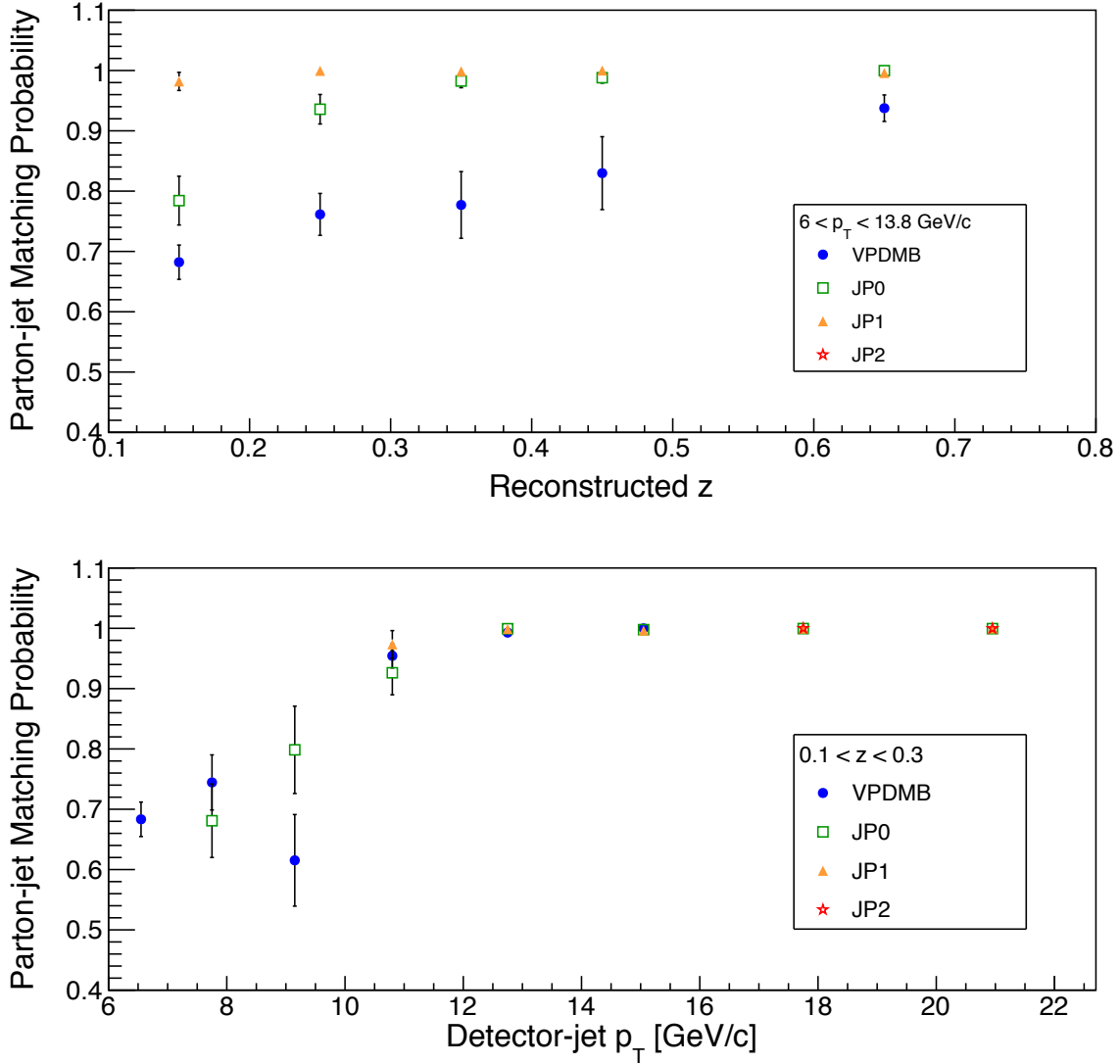


FIG. 15. Parton-jet matching probabilities as a function of (top) reconstructed pion  $z$  for detector jets with  $6 < p_T < 13.8 \text{ GeV}/c$  and (bottom) detector-jet  $p_T$  for pions reconstructed with  $0.1 < z < 0.3$ . Points are plotted at the bin centers. Uncertainties are statistical. There appears to be an increase in matching probability as both  $z$  and  $p_T$  increase.

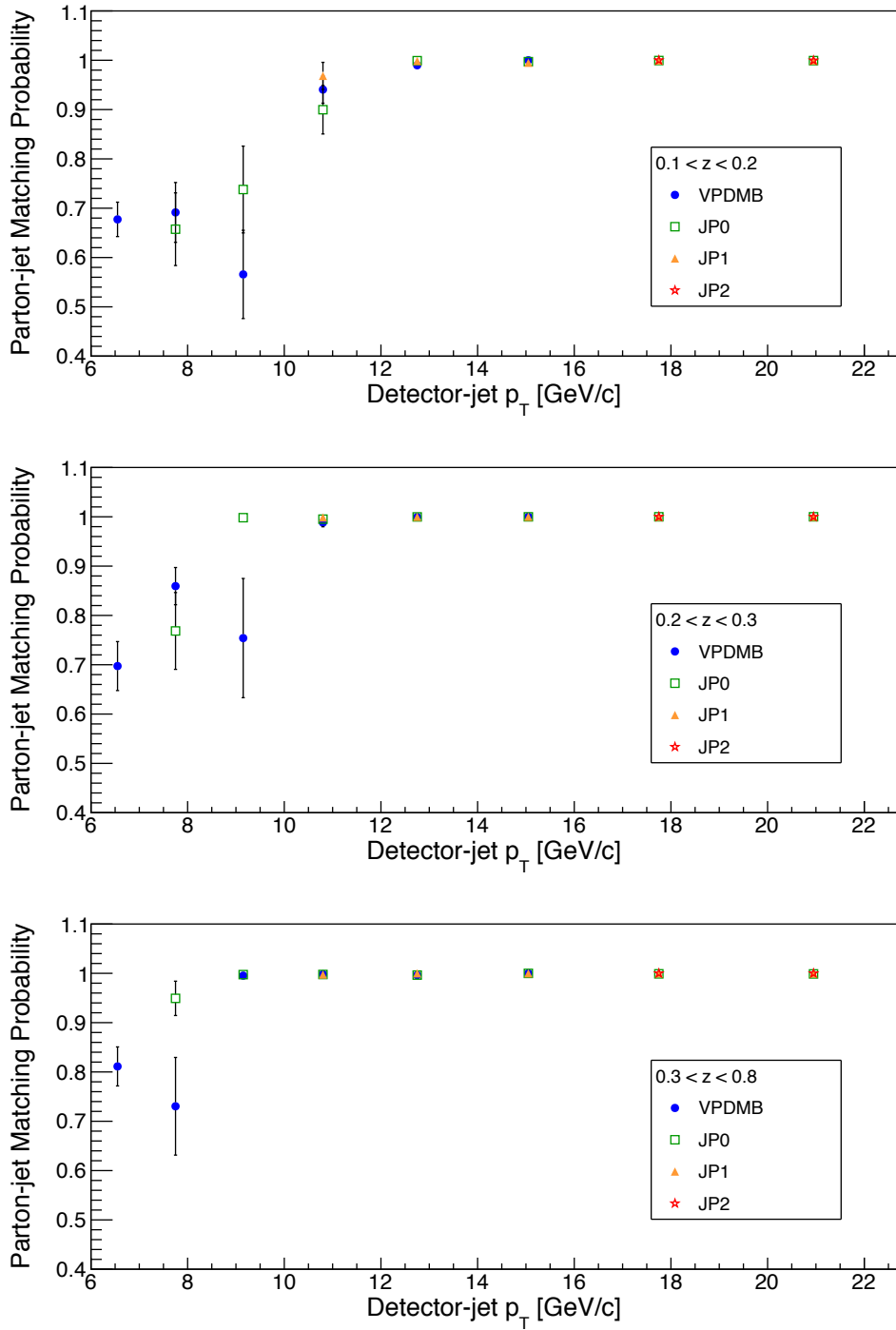


FIG. 16. Parton-jet matching probabilities as a function of detector-jet  $p_T$  in bins of reconstructed pion  $z$ . Points are plotted at the bin centers. Uncertainties are statistical. The matching probabilities appear to increase with jet  $p_T$  across the bins of  $z$ .

[4, 5] and Sivers [6] PDFs) are unconnected to hadronization, and thus parton-jets seem most relevant. For asymmetries of pions within jets, hadronization itself is a critical piece; and thus particle jets are relevant. However, the origins of the effects are still fundamentally linked to hard-scattered partons. Thus, it seems appropriate to classify unmatched jets as a sort of background to the signal. At the moment, however, no theoretical models are equipped to suggest what role the background would play. It seems unlikely that the effects would be more than a dilution, but it is unclear if dilution is the most appropriate assumption. For these reasons, we choose not to correct for the effects of unmatched jets. However, a systematic is applied which takes the full difference between the measured asymmetry and the value if a dilution correction had been applied. Since the matching is estimated trigger-by-trigger, the final matching probability systematic is estimated by averaging over the trigger-by-trigger asymmetries

$$\sigma_{\text{match}} = \frac{\sum_{\text{trig}} A_{\text{trig}} \times |1 - 1/f_{\text{trig}}| / \sigma_{A_{\text{trig}}}^2}{\sum_{\text{trig}} 1/\sigma_{A_{\text{trig}}}^2}, \quad (13)$$

where  $f_{\text{trig}}$  is the matching probability for the relevant trigger. This systematic is negligible for mid-to-high- $p_T$  jets but is a significant concern for low- $p_T$  effects such as the Collins-like asymmetry.

### C. Trigger Bias

The bias from the STAR jet-patch trigger has been well-documented (e.g. Refs. [20] and [11]). For a given jet  $p_T$ , in particular, at low  $p_T$ , the fixed size of the jet patches leads to a higher trigger efficiency for quark jets than less-collimated gluon jets. For the present analysis the effect will vary for the different observables. For the inclusive jet and Collins-like asymmetries, each of which are gluon-based effects, the bias will serve to suppress the effect, in other words, a more biased trigger should lead to a smaller asymmetry. For the Collins asymmetry, the bias should serve to enhance the effect, in other words, a more biased trigger should lead to a larger asymmetry. For the inclusive jet and Collins-like asymmetries, the prime kinematics are right where one expects the largest bias from the trigger. However, for the Collins asymmetries, the prime kinematics are above the region where one expects the trigger to be biased.

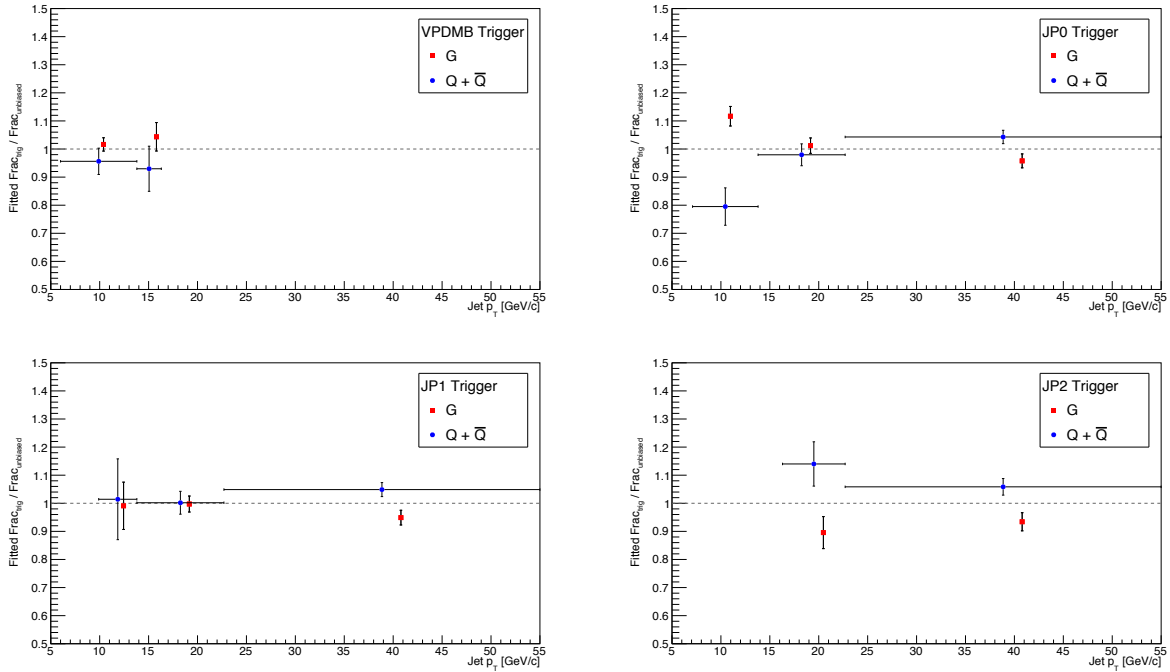


FIG. 17. Ratio of triggered to unbiased quark and gluon jet fractions as a function of reconstructed jet  $p_T$ . Events are separated into the various triggers. One expects the trigger to preference quark jets over gluon jets for fixed  $p_T$  and for the effect to disappear at high  $p_T$ .

For the present analysis, the effects of trigger bias are estimated with simulation. In the embedded Monte Carlo, detector jets are first matched to particle jets and parton jets. Then the jets are matched to lines 7 or 8 of the PYTHIA record (all associations use the minimum  $(\eta, \phi)$  distance and requiring it to be less than 0.5). These events are sorted into quark, anti-quark, and gluon jets. The same is done for the high-statistics PYTHIA sample, now, matching only particle jets to parton jets and lines 7 or 8. The embedding cuts on  $p_T$  and physics  $\eta$  are retained for the PYTHIA study, but all other cuts are released. The  $p_T$  dependence of the ratio of biased-to-unbiased fractions of quark, anti-quark, and gluon jets is analyzed. To extract the best precision possible from the modest statistics, the ratios are averaged across the ranges of “low,” “mid,” and “high”  $p_T$  bins. The results of this analysis are presented in Fig. 17

It is not expected that at high  $p_T$  the bias could be more than 2 – 3%. Unfortunately, the existing embedding sample is sufficiently limited to preclude firm conclusions beyond

$p_T$ Range [GeV/ $c$ ]	Collins Bias	Inclusive-jet and Collins-like Bias
6 – 13.8	17%	10%
13.8 – 22.7	8%	6%
22.7 – 55	3%	3%

TABLE XVIII. Trigger bias systematics for the three observables. The asymmetries are correlated across the full range of  $p_T$ .

this order. The quark bias is estimated as  $6\% \pm 3\%$  within available statistics. Since 6% is higher than expectation and not a significant deviation from expectation, 3% is chosen as an appropriate trigger bias systematic for the high- $p_T$  Collins analysis. For the inclusive-jet and Collins-like analyses, the gluon precision of 3% is also chosen as the systematic from trigger bias.

For mid- $p_T$  jets, a weighted average approach is utilized. Each of the biases from the fits is weighted by its respective fractions of the mid- $p_T$  data (VPDMB at 0.3%, JP0 at 13%, JP1 at 30%, and JP2 at 56%). The result is an 8% bias for quarks and 6% bias for gluons.

The low- $p_T$  JP0 deviations are quite a departure from the expectation of a biased trigger enhancing the relative quark fractions. The JP0 bias estimates for the standard augmented trigger threshold are compared to those with the nominal trigger threshold. The differences (0.10 for quarks and 0.060 for gluons) are folded in quadrature with the JP1 uncertainties (14% for quarks and 8% for gluons) for the final low- $p_T$  estimate: 17% for quarks and 10% for gluons. These are summarized in Table XVIII. The systematic is correlated, in this case, across the full range of  $p_T$ .

Relevant, also, for the present analysis is the range of  $x$  sampled by the data. For example, since transversity is known to depend strongly on  $x$ , knowledge of the present sensitivity would be quite useful. Further, for purposes of comparing to SIDIS or to STAR data at different  $\sqrt{s}$ , a rough idea of the active range of  $x$  could be quite important for drawing reasonable conclusions.

The active range of  $x$  will be somewhat distorted by the effects of reconstruction and trigger bias. To estimate this, the embedding simulations are analyzed, again, using the jets matched back to PYTHIA particles 7 and 8. For the present purpose, the events are further

required to have a flavor match to line 5 or 6. Events are separated based on trigger, jet  $p_T$ , parton species, and  $\eta$  calculated relative to lines 5 or 6. The embedding events can then be compared to the unbiased distributions using the high-statistics, pure PYTHIA sample. The results for two of the most interesting cases,  $x_G$  for low- $p_T$  VPDMB and  $x_Q$  for high- $p_T$  JP2, are shown in Fig. 18. One can see that the VPDMB distribution agrees quite well with the unbiased distribution. Since VPDMB is simulated as “take-all” the only deviations could be those from reconstruction effects or pile-up backgrounds. The JP2 distribution appears to deviate somewhat from the unbiased distribution. These deviations can come from both reconstruction and trigger bias. The largest bias is expected to arise from the JP0 trigger near the threshold, where the jets are less collimated. The low- $p_T$  JP0 distribution for gluons is shown with the mid- $p_T$  JP1 distribution for quarks in Fig. 19. One can see that the peaks for the triggered and unbiased JP0 distributions are shifted by about 10 – 20%. The peaks for JP1 also seem to be shifted, though, the embedding statistics are much lower.

#### D. Azimuthal Resolutions

Since the asymmetries of interest are extracted from the azimuthal dependence of the spin-dependent cross sections, finite azimuthal resolution leads to a systematic dilution of the true asymmetries. For the inclusive jet asymmetry the effects are relatively small and arise from imprecise reconstruction of the jet axis. The size of the smearing is estimated from the embedding simulation. First, the event-by-event deviations of the reconstructed jet azimuth,  $\delta\phi = \phi_{\text{reco}} - \phi_{\text{thrown}}$ , are binned trigger-by-trigger. Next, these histograms are convoluted with a sinusoid. The result is fit with a sinusoid of unit amplitude, and the new amplitude is taken as the size of the dilution due to finite azimuthal resolution. This dilution is used to correct the measured asymmetries and is applied trigger-by-trigger.

For asymmetries of pions within jets the procedure is analogous to what is listed above for the inclusive-jet asymmetry, using instead of the azimuthal angle of the jet axis, the Collins ( $\phi_S - \phi_H$ ) or Collins-like ( $\phi_S - 2\phi_H$ ) angles, as appropriate. However, there is the added complication of imprecise reconstruction of the orientation of the pion about the jet axis. This carries with it a dependence upon the proximity of the pion to the jet axis, denoted

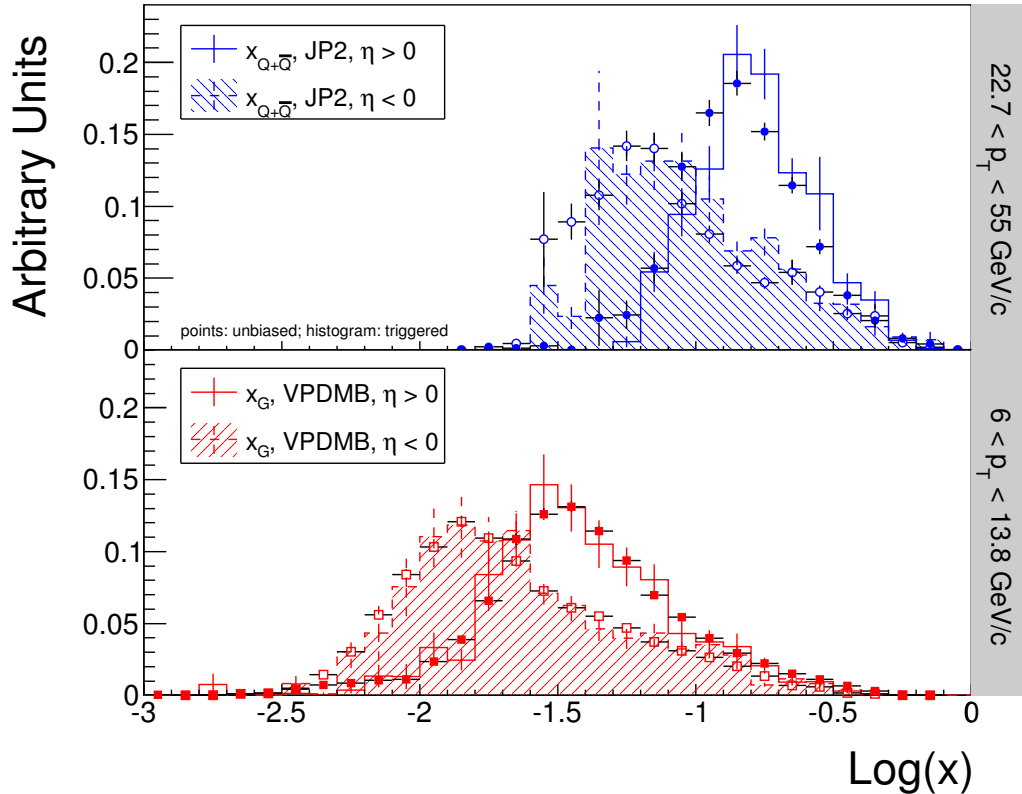


FIG. 18. Triggered (histogram) and unbiased (points) distribution of  $x$ . Low- $p_T$  VPDMB and high- $p_T$  JP2 events are compared to their respective unbiased distributions. For VPDMB, the only deviations should arise from reconstruction and pile-up effects. For JP2, the deviations can arise both from reconstruction effects and from bias in the event trigger.

here as

$$\Delta R = \sqrt{(\eta_{\text{jet}} - \eta_\pi)^2 + (\phi_{\text{jet}} - \phi_\pi)^2}. \quad (14)$$

To ensure robust reconstruction of the relevant angles, a minimum cut on  $\Delta R$  is imposed for the Collins and Collins-like asymmetries. The cut is optimized by the following procedure: First, the  $\delta\phi$  convolutions are evaluated for different lower limits on  $\Delta R$  (e.g. Fig. 20). Second, using the extracted dilutions, the  $\Delta R$ -dependence of projected asymmetry uncertainties are evaluated. Specifically, the projected relative uncertainties are calculated as

$$\frac{\sigma_{\text{cut}}}{\sigma_{\text{no cut}}} \approx \sqrt{\frac{N_{\text{no cut}} \times D_{\text{no cut}}^2}{N_{\text{cut}} \times D_{\text{cut}}^2}}. \quad (15)$$

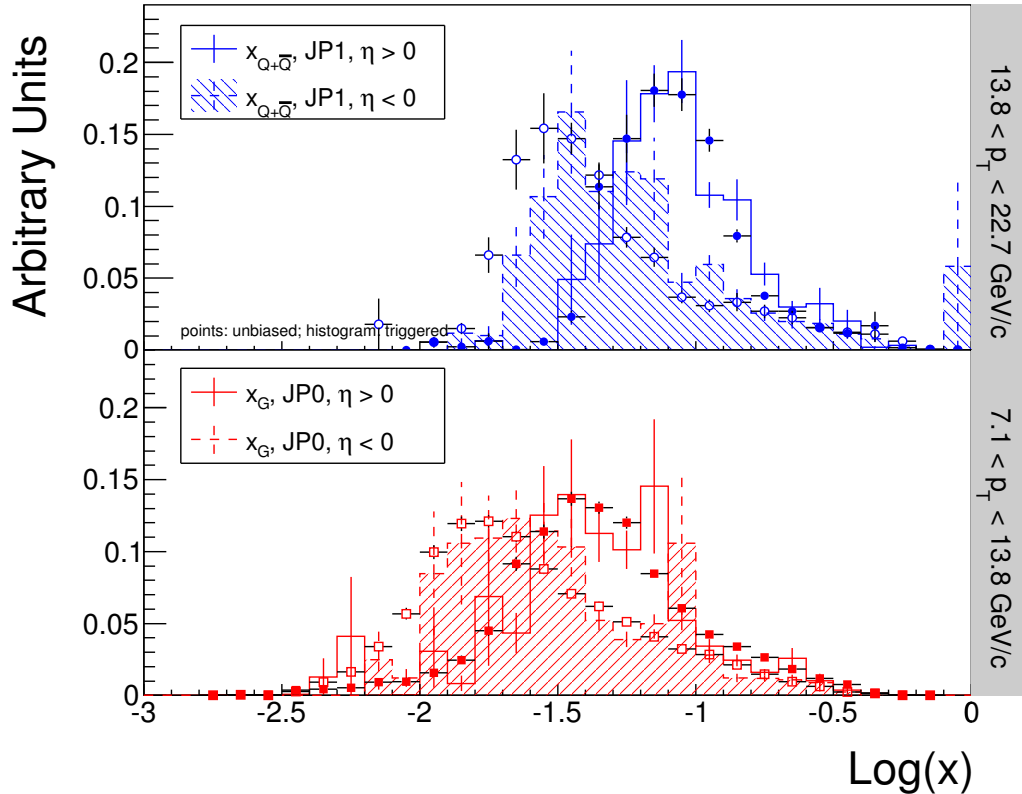


FIG. 19. Triggered (histogram) and unbiased (points) distribution of  $x$ . Low- $p_T$  JP0 and mid- $p_T$  JP1 events are compared to their respective unbiased distributions. The deviations can arise both from reconstruction effects and from bias in the event trigger.

Three of the more relevant examples are presented in Fig. 21. One can observe that for low jet  $p_T$  and low pion  $z$ , neither the dilutions nor the relative uncertainties show much dependence upon minimum  $\Delta R$ . The situation changes for high- $z$  events, in particular, at high jet  $p_T$ . While the dilution shows a fairly modest dependence upon minimum  $\Delta R$ , the yield drops much faster as a function of minimum  $\Delta R$ . Thus, for the final analysis cut  $\Delta R_{\min} = 0.04$  is chosen. One must also note that a relaxed  $\Delta R$  cut also opens up the  $(z, j_T)$  phase space, which becomes tightly correlated for more restrictive  $\Delta R$  cuts. This is of crucial importance to the Collins asymmetry measurement.

Two systematic uncertainties are estimated for the resolution correction and added in quadrature. The initial systematic accounts for fluctuations due to finite Monte Carlo statistics, while the second (only applied for the Collins and Collins-like asymmetries) accounts

for sensitivity to inaccuracies in the Monte Carlo simulation of the jet-axis smearing.

For the initial systematic uncertainty, the  $\delta\phi$  histograms are, first, fit with a triple-Gaussian function: two centered at zero and one centered at  $\delta\phi = \pm\pi$ . The log-likelihood method is used for this fit. The resulting function is, then, convoluted with a sinusoid to obtain an alternate dilution. The difference between the two dilutions is taken as a systematic uncertainty on the dilution from finite azimuthal resolution.

For the second systematic uncertainty some care is needed. Inclusive jet asymmetries are fairly insensitive to the jet thrust axis resolution (e.g.  $\sigma = 0.14$  produces a  $\sim 1\%$  dilution). For the Collins and Collins-like effects, the relevant thrust axis resolution is that between the detector-jet and particle-jet levels. Thus, the only concerns are uncertainties at the GEANT level, as opposed to the PYTHIA level. One expects the dominant contributions to the jet thrust-axis resolutions to arise from finite tracking and calorimeter efficiencies. Since the tracking efficiency is smaller than that of the calorimeter, moreover with the larger uncertainty, the level of sensitivity to the tracking efficiency should serve as a reasonable estimate of the sensitivity to simulation uncertainties. To estimate this sensitivity, the dilutions are calculated with the 93% tracking efficiency embedding sample. For high- $p_T$  jets, the 93% tracking dilutions differ from the nominal typically by 1% or less. For low- $p_T$  jets, the differences are typically on the order of 2 – 3% with a few bins reaching as high as  $\sim 10\%$ . The difference between the nominal dilution and the “93%” dilution is added in quadrature to the initial systematic uncertainty to estimate the total resolution systematic uncertainty.

Since the correction is applied trigger-by-trigger, the final systematic is averaged over the various triggers

$$\sigma_{\text{res}} = \frac{\sum_{\text{trig}} A_{\text{trig}} \times \left( \sqrt{(D_{\text{trig}} - D^{\text{alt}})^2 + (D_{\text{trig}} - D^{93\%})^2} / D_{\text{trig}} \right) / \sigma_{A_{\text{trig}}}^2}{\sum_{\text{trig}} 1/\sigma_{A_{\text{trig}}}^2}, \quad (16)$$

where  $D$ ,  $D^{\text{alt}}$ , and  $D^{93\%}$  are, respectively, the dilutions as calculated from the nominal histograms, the nominal triple-Gaussian fits, and the 93% tracking-efficiency histograms. A summary of the corrections and the associated relative uncertainties is presented in Appendix B.

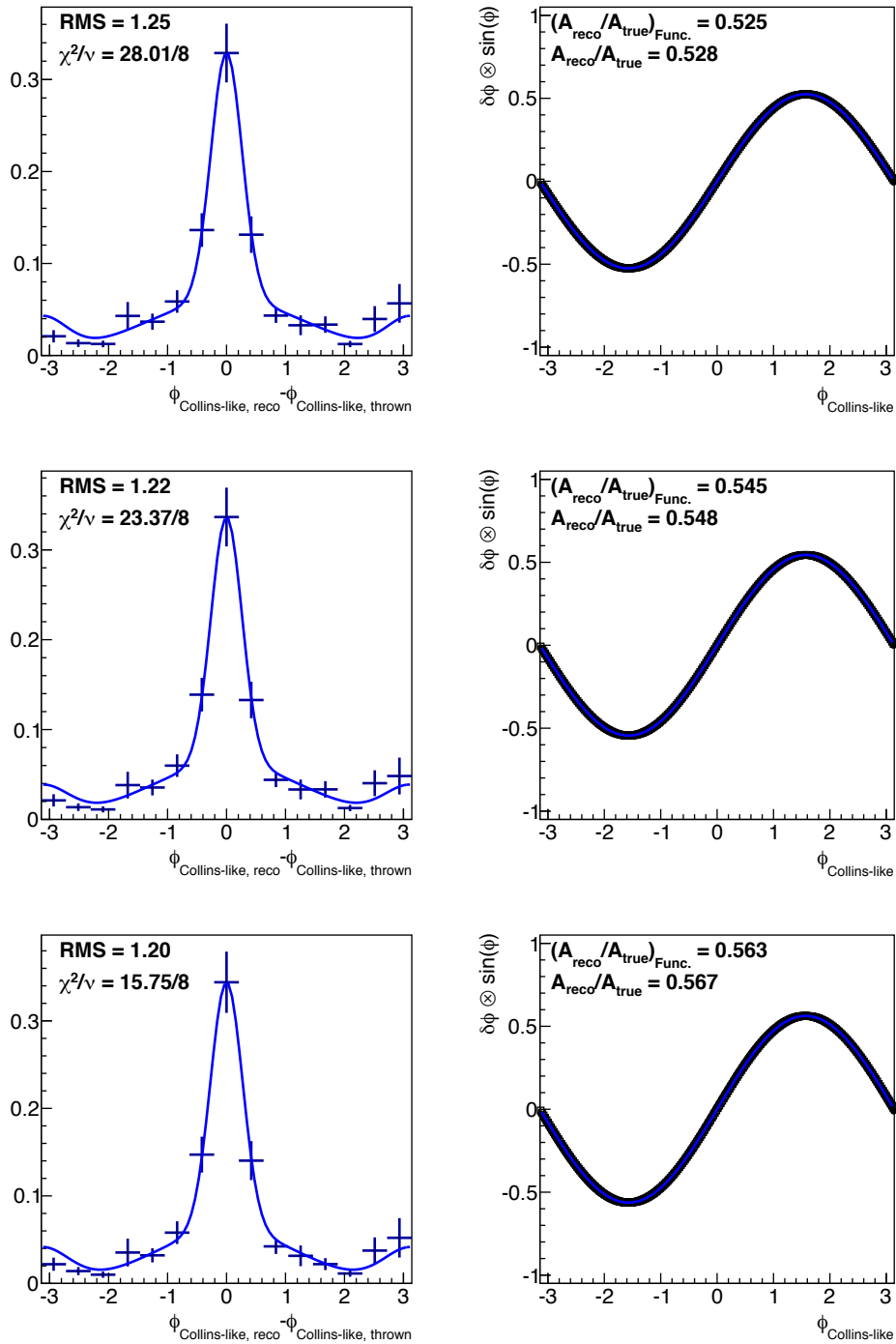


FIG. 20. Histograms and fits of  $\delta\phi$  and the resulting sinusoid convolutions for Collins-like with  $6 < p_T < 7.1$  GeV/c and  $0.1 < z < 0.3$ . Shown are the results for (top)  $\Delta R_{\min} = 0$ , (middle)  $\Delta R_{\min} = 0.04$ , and (bottom)  $\Delta R_{\min} = 0.1$ .

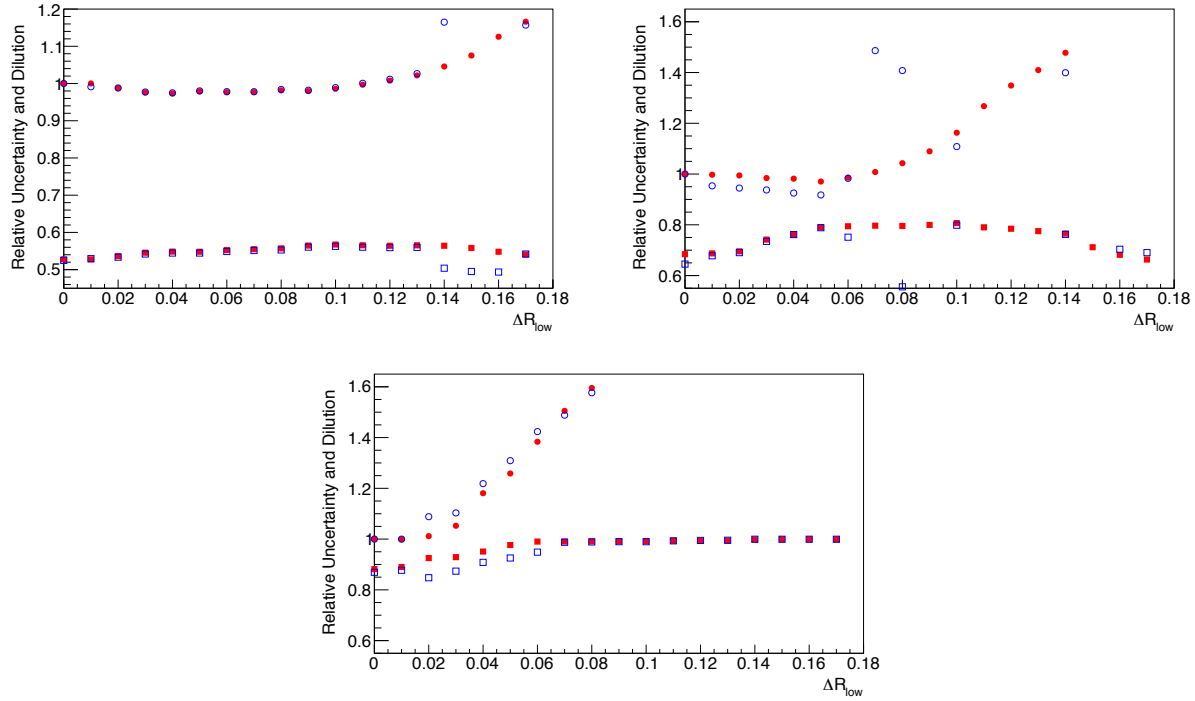


FIG. 21. Projected relative uncertainties and asymmetry dilutions as a function of minimum hadron radius  $\Delta R_{\min}$ . Dilutions are the lower series of points. In red are plotted the results of convoluting the raw  $\delta\phi$  histograms and in blue are plotted the results of convoluting the log-likelihood fit to the histogram. Shown are the projections for (upper left) Collins-like with  $6 < p_T < 7.1$  GeV/ $c$  and  $0.1 < z < 0.3$ , (upper right) Collins with  $7.1 < p_T < 8.4$  GeV/ $c$  and  $0.3 < z < 0.8$ , and (bottom) Collins with  $22.7 < p_T < 26.8$  GeV/ $c$  and  $0.3 < z < 0.8$ . One can observe that while the Collins-like dilutions and uncertainties are relatively independent of  $\Delta R_{\min}$  at low  $p_T$  and low  $z$ , the Collins dilutions and uncertainties at high  $z$  depend strongly on  $\Delta R_{\min}$ .

### E. Non-uniform Acceptance Effects

The jet and pion yields for the various spin states depend on contributions from all of the various modulations, specifically for the present case, the inclusive-jet, Collins, and Collins-like asymmetries. One can express the yields in the  $\alpha$  half of the detector in terms of the

detector acceptance,  $I$ ; beam luminosity,  $\mathcal{L}$ ; and unpolarized cross section,  $\sigma_0$ ,

$$\begin{aligned} N_\alpha^\uparrow(\phi_S, \phi_C, \phi_{CL}) &= \mathcal{L}^\uparrow I_\alpha(\phi_S, \phi_C, \phi_{CL}) \sigma_0 \\ &\times \left[ 1 + A_{UT}^{\sin \phi_S} \sin \phi_S + A_{UT}^{\sin \phi_C} \sin \phi_C + A_{UT}^{\sin \phi_{CL}} \sin \phi_{CL} \right], \end{aligned} \quad (17)$$

with similar expressions for other detector halves and beam polarizations. For example, if one integrates over the acceptance for  $\phi_S$  and  $\phi_{CL}$  to form cross ratios for the Collins asymmetry, one obtains in the limit of small physics and acceptance asymmetries

$$\epsilon(\phi_C) = A_{UT}^{\sin \phi_C} \sin \phi_C + A_{UT}^{\sin \phi_S} \mathcal{S}(\phi_C) + A_{UT}^{\sin \phi_{CL}} \mathcal{G}(\phi_C), \quad (18)$$

where terms  $\mathcal{S}$  and  $\mathcal{G}$  involve integrals over the detector acceptance of the form

$$\frac{1}{2} \frac{\int_{-\pi}^{\pi} \int_{-\pi/2}^{\pi/2} I_\alpha(\phi_S, \phi_C, \phi_{CL}) \sin(\phi_S) d\phi_S d\phi_{CL}}{\int_{-\pi}^{\pi} \int_{-\pi/2}^{\pi/2} I_\alpha(\phi_S, \phi_C, \phi_{CL}) d\phi_S d\phi_{CL}}, \quad (19)$$

and similarly for the  $\sin(\phi_{CL})$  modulation. In the limit of uniform acceptance,  $I$  factors out of the integrals; and  $\mathcal{S}$  and  $\mathcal{G}$  vanish. Thus, the cross ratio will isolate the Collins asymmetry, and analogous arguments hold for isolating the other effects. When detector acceptance is not uniform, the  $\mathcal{S}$  and  $\mathcal{G}$  terms will distort the azimuthal dependence of the desired asymmetry.

The shape of the distortion due to non-uniform acceptance, can be extracted from the data, itself, utilizing the method described in Ref. [15]. Taking the Collins asymmetry as an example, for each event in the data,  $\phi_C = \phi_S - \phi_H$  histograms are filled using the Collins angle as calculated for the event. Events are given weights of

$$w_0 = 1 + A_{in} \sin(\phi_{S, \text{true}}) \quad (20)$$

$$w_1 = 1 - A_{in} \sin(\phi_{S, \text{true}}), \quad (21)$$

where  $A_{in}$  is an input asymmetry and “true” denotes that  $\phi_S$  is calculated in the general case rather than the special case used to form the cross-ratios, as described in Section VI. Each event is binned twice, once for each spin state. The histogram for the actual event spin state is filled using weights of  $w_0$ , while the histogram for the opposite spin state is filled using weights of  $w_1$ . In this manner, an unpolarized sample is constructed (in the limit of vanishing luminosity asymmetries) removing any complications from actual physics coupling to the input asymmetries. Similar histograms are created for each of the desired

effects and their potential contaminations. For the Collins and Collins-like contaminations to the inclusive jet asymmetry, the weights are constructed by looping over all pions in the event and weighting by  $z$  or  $1 - z$  for the Collins or Collins-like case, respectively. For the Collins case, input asymmetries of opposite sign are constructed for  $\pi^+$  and  $\pi^-$ ; while for the Collins-like case, input asymmetries of the same sign are used for the different pion states. The cross ratios for the relevant asymmetries are calculated using the weighted-event histograms and are fit with a function of the form

$$\epsilon(\phi) = p_0 + p_1 \sin(\phi). \quad (22)$$

The  $\phi$ -bin-by- $\phi$ -bin cross ratio uncertainties are calculated according to

$$\begin{aligned} \sigma_\epsilon^2 = & \frac{1}{(A+B)^4} \left\{ \frac{B^2}{A^2} \left[ (\beta^\downarrow)^2 \sum_i (w_i^\uparrow)^2 + (\alpha^\uparrow)^2 \sum_j (w_j^\downarrow)^2 \right] \right. \\ & + \frac{A^2}{B^2} \left[ (\beta^\uparrow)^2 \sum_i (w_i^\downarrow)^2 + (\alpha^\downarrow)^2 \sum_j (w_j^\uparrow)^2 \right] \\ & \left. - 2 \left( \beta^\downarrow \beta^\uparrow \sum_i w_i^\uparrow w_i^\downarrow + \alpha^\uparrow \alpha^\downarrow \sum_j w_j^\uparrow w_j^\downarrow \right) \right\}, \end{aligned} \quad (23)$$

where  $w_i$  and  $w_j$  denote weights for the  $\alpha$  and  $\beta$  halves, respectively;  $\alpha = \sum_i w_i$ ;  $\beta = \sum_j w_j$ ;  $A^2 = \alpha^\uparrow \beta^\downarrow$ ; and  $B^2 = \alpha^\downarrow \beta^\uparrow$ . Examples of the fits for each of the observables and their potential contaminations are presented in Fig. 22

In principle the distortion to the asymmetry is solely from the  $p_1$  parameter of the fit. Thus, one could argue for only including  $p_1$  and  $\sigma_{p_1}$  in the systematic estimate. To be conservative the systematic is estimated as

$$\sigma_{\text{leak}} = \frac{\text{Max}(|A_{\text{leak}}|, \sigma_{A_{\text{leak}}})}{A_{\text{in}}} \times \text{Max}(|p_1|, \sigma_{p_1}), \quad (24)$$

where  $A_{\text{leak}}$  is the measured asymmetry for the ‘‘competing’’ effect and  $A_{\text{in}}$  is the asymmetry weighted into the data for the study. For each of the asymmetries of interest, the ‘‘leak-through’’ systematic is calculated for each of the competing effects and the two are added to find the total systematic.

One can see from Fig. 22 that the distortions to the inclusive-jet asymmetry are quite minimal. For the Collins ‘‘leak-through’’ this is aided by the fact that  $\pi^+$  and  $\pi^-$  asymmetries contribute with different signs and equal magnitudes. For Collins-like ‘‘leak-through’’ the

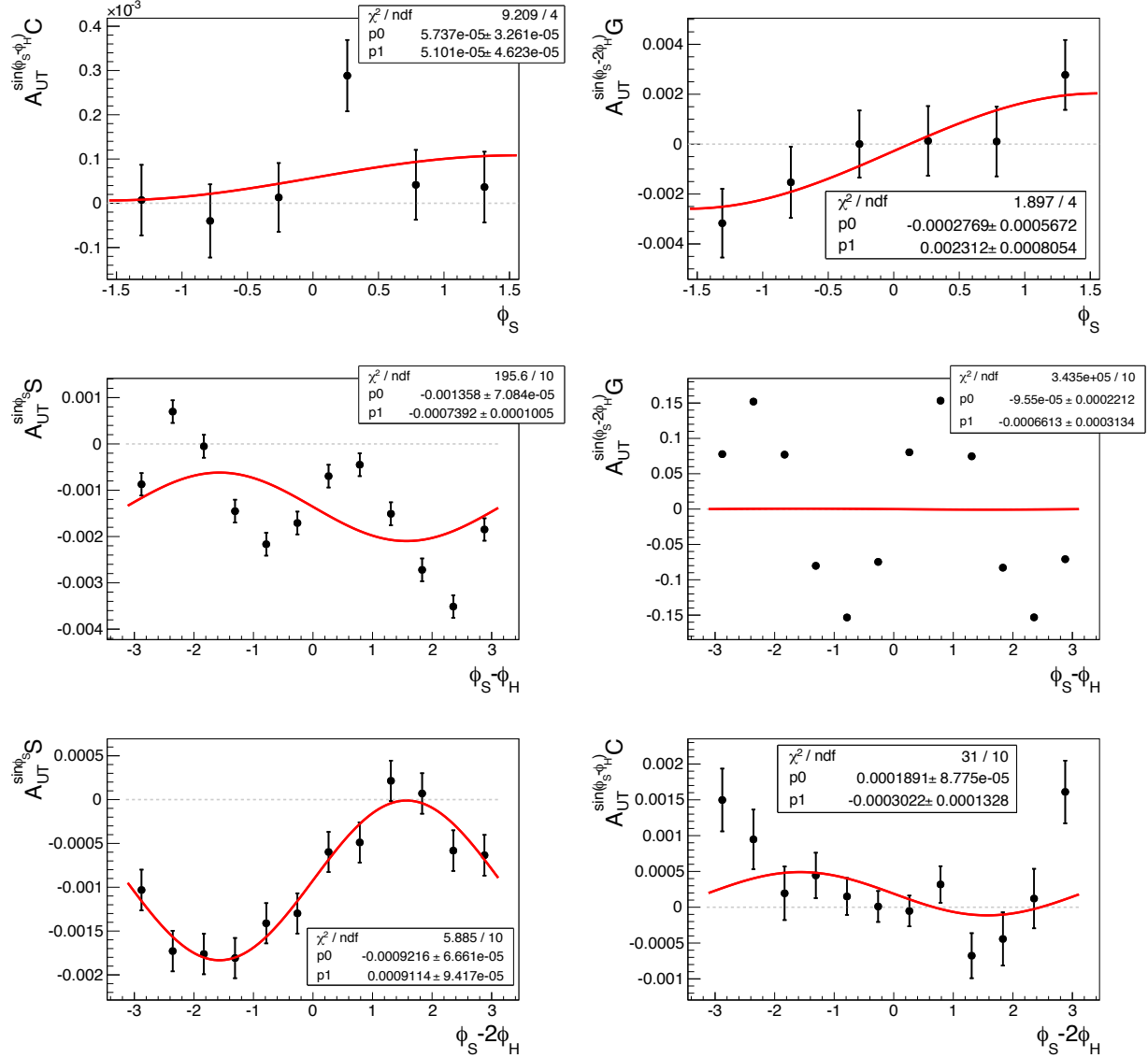


FIG. 22. Examples of the shape of “leak-through” effects for each of the physics observables. Input asymmetries are as follows: 0.10 for inclusive jet,  $\pm 0.25$  for  $\pi^\pm$  Collins (with linear  $z$ -dependence for distortion to inclusive jet), and 0.25 for  $\pi^\pm$  Collins-like (with  $(1 - z)$ -dependence for distortion to inclusive jet). Top are shown the (left) Collins and (right) Collins-like distortions to the inclusive-jet asymmetry for  $22.7 < p_T < 26.8$  GeV/ $c$  with  $0.5 < |\eta| < 1$  and  $6 < p_T < 7.1$  GeV/ $c$  with  $|\eta| < 0.5$ , respectively. Middle are shown the (left) inclusive-jet and (right) Collins-like distortions to the high- $p_T$   $\pi^+$  Collins asymmetry for  $0.1 < z < 0.2$  and  $0.2 < z < 0.3$ , respectively. Bottom are shown the (left) inclusive-jet and (right) Collins distortions to the low- $p_T$  Collins-like asymmetry ( $\pi^+$  and  $\pi^-$ , combined) for  $0.1 < z < 0.2$  and  $0.2 < z < 0.3$ , respectively.

asymmetry is assumed to have the same sign and magnitude for different pion states, however, the detector acceptance is nearly uniform, greatly suppressing the amount of distortion. For the distortions to the Collins asymmetry, in particular for the Collins-like “leak-through,” the shapes are often quite far from sinusoidal. This is due to the fact that the  $(\phi_C, \phi_{CL})$  acceptance is never uniform by virtue of the definitions of the angles. In fact, the distortions to the Collins (and similarly for Collins distortions to charge-separated Collins-like asymmetries) follow a  $\sin(2\phi)$ -type trend with an amplitude suppressed from the input asymmetry. However, in evaluating the systematic distortion in the extracted asymmetry, the  $\sin \phi$  moment is the relevant quantity, and the magnitude of this component is typically minuscule. As a further check on this distortion, one can analyze the  $\chi^2$  distribution of the sinusoidal fits. Finally, the present analysis benefits greatly from a convenient coincidence in the laws of nature. The gluon-based Collins-like effect should be significant only at low- $p_T$ , whereas the quark-based Collins effect should be significant only at high- $p_T$ . Thus, no matter the size of the distortion from acceptance, the final distortions will be highly suppressed by the small size of the competing asymmetries. Thus, the only possibly large distortions would arise from “leak-through” of the inclusive-jet asymmetry at low  $p_T$  and vice versa. As one observes, these distortions are far more well-behaved with amplitudes highly suppressed from relatively uniform acceptance.

A final acceptance-related systematic is dilution from finite bin-width. The asymmetry is extracted by fitting the  $\phi$ -dependence of the cross-ratios. The finite size of the bins will introduce a dilution to the extracted asymmetry. This is further complicated by acceptance non-uniformity within the bins. The size of this effect can be calculated using the infrastructure developed for the “leak-through” estimates. Now, instead of weighting events with input asymmetries for the competing effects, events are weighted with input asymmetries for the desired effect. The unpolarized construction, again, removes complications from the presence of real physics asymmetries. By fitting the resulting asymmetries, the extracted amplitude gives a fairly precise estimate of the dilution from finite binning. This dilution is found to be on the order of 1.5% and the values are used as a correction to the measured asymmetries.

## F. Contaminations to Pion Sample

For the present analysis, the desired events are inclusive jets and pions within jets. For inclusive jets, the background of main concern are those events at the detector-jet level which do not associate with a parton-jet. For pions within jets there is the additional background of contamination to the pion sample from protons, kaons, and electrons. Estimates of this contamination are predicated on the analysis of two types of data distributions:  $n_\sigma(\pi)$  and  $m^2$ . The former parameter is measured in the TPC and defined

$$n_\sigma(\pi) = \frac{1}{\sigma_{\text{exp}}} \ln \left( \frac{dE/dx_{\text{obs}}}{dE/dx_{\pi \text{ calc}}} \right), \quad (25)$$

where  $dE/dx_{\text{obs}}$  is the observed value for the event,  $dE/dx_{\pi \text{ calc}}$  is the expected mean  $dE/dx$  for pions, and  $\sigma_{\text{exp}}$  is the  $dE/dx$  resolution of the TPC [25]. The latter parameter is calculated as

$$m^2 c^4 = p^2 c^2 \left( \frac{1}{\beta^2} - 1 \right), \quad (26)$$

where  $p$  is the track momentum measured in the TPC, and  $\beta = v/c$  as measured by the TOF. The present analysis follows the standard procedure to fit  $n_\sigma(\pi)$  with a multi-Gaussian function to extract yield for pions, protons, kaons, electrons, and merged tracks, from which the pion signal fraction can be determined by integrating over the active  $n_\sigma(\pi)$  range. At the time this analysis is being conducted, the TOF simulator is not implemented; therefore an empirical fit procedure is used for the TOF  $m^2$  distributions. A multi-Voigt-profile is used to extract the pion, kaon, and proton yields, so chosen as it yields an apparently better description of the data than a multi-Gaussian distribution. Once the TOF simulator is implemented, a template-style fit based on Monte Carlo will undoubtedly yield a more accurate extraction. However, at the moment, the current procedure is more than adequate.

The  $n_\sigma(\pi)$  distributions are fairly unstable when fit with a multi-Gaussian function with all parameters allowed to float. Therefore, the fits are tuned, as follows: First, the data are parsed into bins of both jet  $p_T$  and pion  $z$ . Further, the  $0.1 < z < 0.2$  bin is split into two more bins:  $0.1 < z < 0.15$  and  $0.15 < z < 0.2$ . This is to ensure that the bins are sufficiently fine that the  $n_\sigma(\pi)$  distributions are not changing so rapidly within the kinematic bins. The expected centroid locations for the kaon, proton, and electron peaks are extracted by evaluating  $n_\sigma(\pi)$  as a function of  $n_\sigma(K)$ ,  $n_\sigma(p)$ , and  $n_\sigma(e)$ . An example is shown in

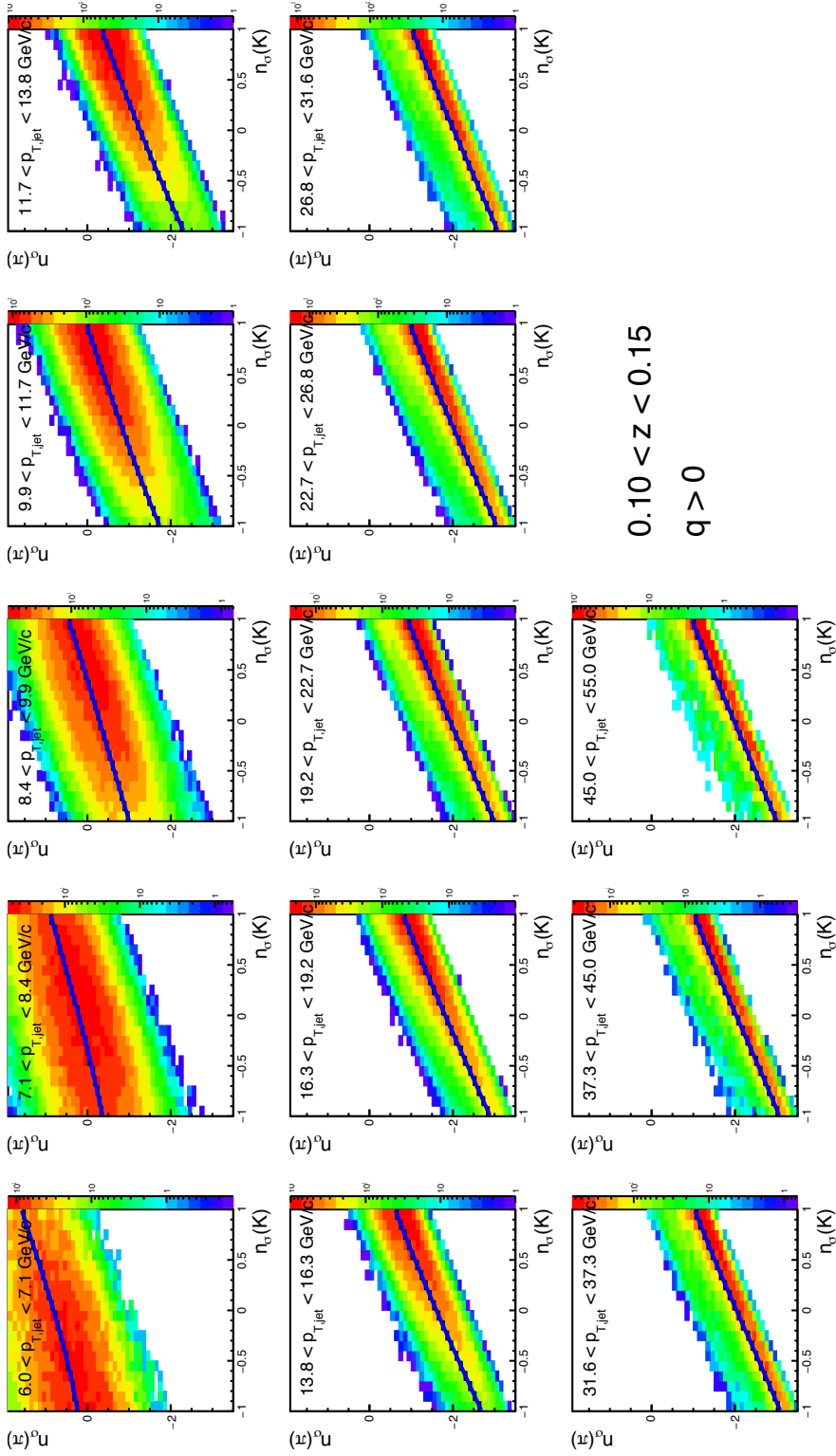


FIG. 23. Data distributions of  $n_\sigma(\pi)$  vs.  $n_\sigma(K)$ . Ideally, the kaon Gaussian centroid locations in  $n_\sigma(\pi)$  should occur where  $n_\sigma(K) = 0$ . These values are extracted by fitting a third-order polynomial to the distributions, shown by the blue curves.

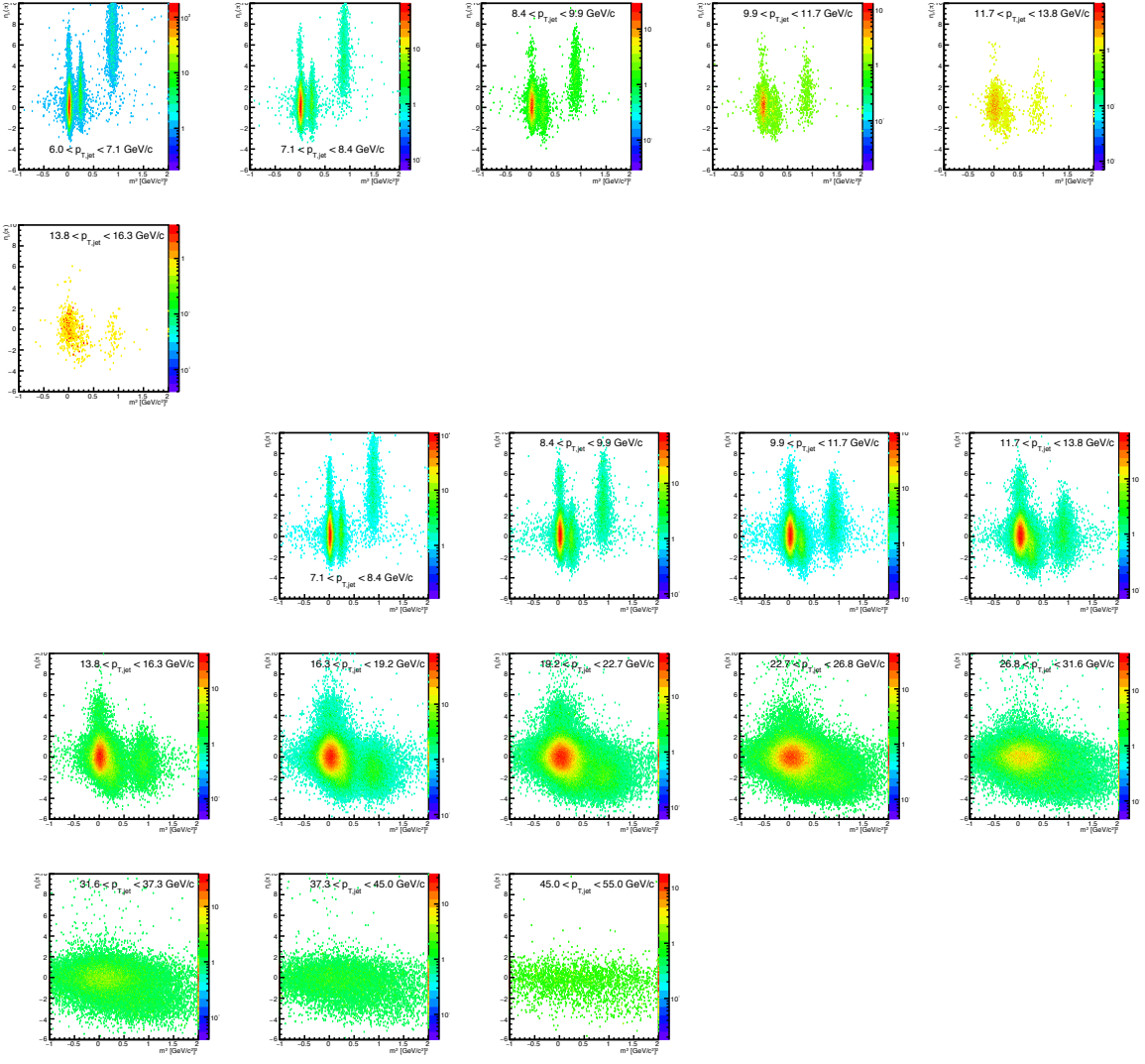


FIG. 24. Data distributions of  $n_\sigma(\pi)$  vs.  $m^2$  for VPDMB (top two rows) and JP0 (bottom three rows) as a function of jet  $p_T$  for particles with  $0.1 < z < 0.15$ .

Fig. 23 for kaons. The kaon centroids in  $n_\sigma(\pi)$  should fall at the values corresponding to  $n_\sigma(K) = 0$ , and similarly for protons and electrons at  $n_\sigma(p) = 0$  and  $n_\sigma(e) = 0$ . As pointed out in Ref. [26], there are corrections to these expectations that can be estimated by evaluating the centroids as a function of  $\beta\gamma$ . The present analysis does not have access to the high- $p_T$  kaon and proton-rich samples, as in Ref. [26]. At low momentum, fairly pure samples of pions, kaons, protons, and electrons can be constructed by selecting on TOF  $m^2$ . Figure 24 presents distributions of  $n_\sigma(\pi)$  versus  $m^2$  for VPDMB and JP0 events as functions of jet

$p_T$  with  $0.1 < z < 0.15$ . For  $6 < p_T < 13.8 \text{ GeV}/c$ , the peaks are separated enough so that pure samples can be fitted to extract the appropriate functional parameters for the  $n_\sigma(\pi)$  distributions. Above  $13.8 \text{ GeV}/c$  it becomes difficult to construct pure samples. However, the pion centroids can still be extracted from a full, multi-Gaussian fit to evaluate their deviation from the expected value of zero. The results are presented in Fig. 25. Similar to Ref. [26], the results are fit with a function of the form  $p_0 + p_1/(p_2 + x^2)$  across the range  $2 < \langle p_T \rangle / m < 5 \times 10^4$ . Below 2, the centroids deviate significantly from the trend. This is likely an artifact of the momentum bins being relatively coarse compared to the associated rate of change in  $dE/dx$  for protons and kaons at these kinematics. These bins are of no consequence to the background correction, since the present analysis uses TOF  $m^2$  for the estimates at low momentum. For systematics estimates, the low-momentum  $n_\sigma(\pi)$  fits can be fixed with the parameters directly from the pure-sample fits. In the range of the  $p_T/m$  fit, the low-momentum points stitch rather nicely with the high-momentum points. The values from the fitted curve are used as a correction to the expected centroid locations of the high-momentum multi-Gaussian  $n_\sigma(\pi)$  fits. To ensure further stability in the multi-Gaussian fits, the peak widths are evaluated as a function of  $p/m$  (e.g. Fig. 26). In principle the peak widths should be unity, however, previous studies have shown the fits tend to fall a bit below unity [26]. The present results qualitatively agree with this at higher values of  $p/m$ . At lower values, the results tend to be higher than unity. Again, this is likely due to the binning being somewhat coarse compared to the rate of change in  $dE/dx$  at these kinematics. The distribution is fit with a function of the form  $p_0 + p_1/(p_2 + x^2)$ . The pion, kaon, and proton Gaussian widths in the full  $n_\sigma(\pi)$  fits are set to the values corresponding to the fit function. The electron peak widths tend to fall systematically above the curve, thus, the electron peak widths are allowed to float.

An example of the multi-Gaussian  $n_\sigma(\pi)$  fits is shown in Fig. 27 for particles with  $0.1 < z < 0.15$ . One can clearly see the changing location of the peaks as a function of momentum. The kaon peak passes below the pion peak around the  $8.4 < p_T < 9.9 \text{ GeV}/c$  bin. The proton peak passes below the pion peak around the  $11.7 < p_T < 13.8 \text{ GeV}/c$  bin. The proton peak passes below the kaon peak around the  $22.7 < p_T < 26.8 \text{ GeV}/c$  bin. Therefore, the  $n_\sigma(\pi)$  distributions alone are not sufficient to estimate the contaminations to the pion yield at lower particle momenta. For this, the present analysis turns to TOF distributions.

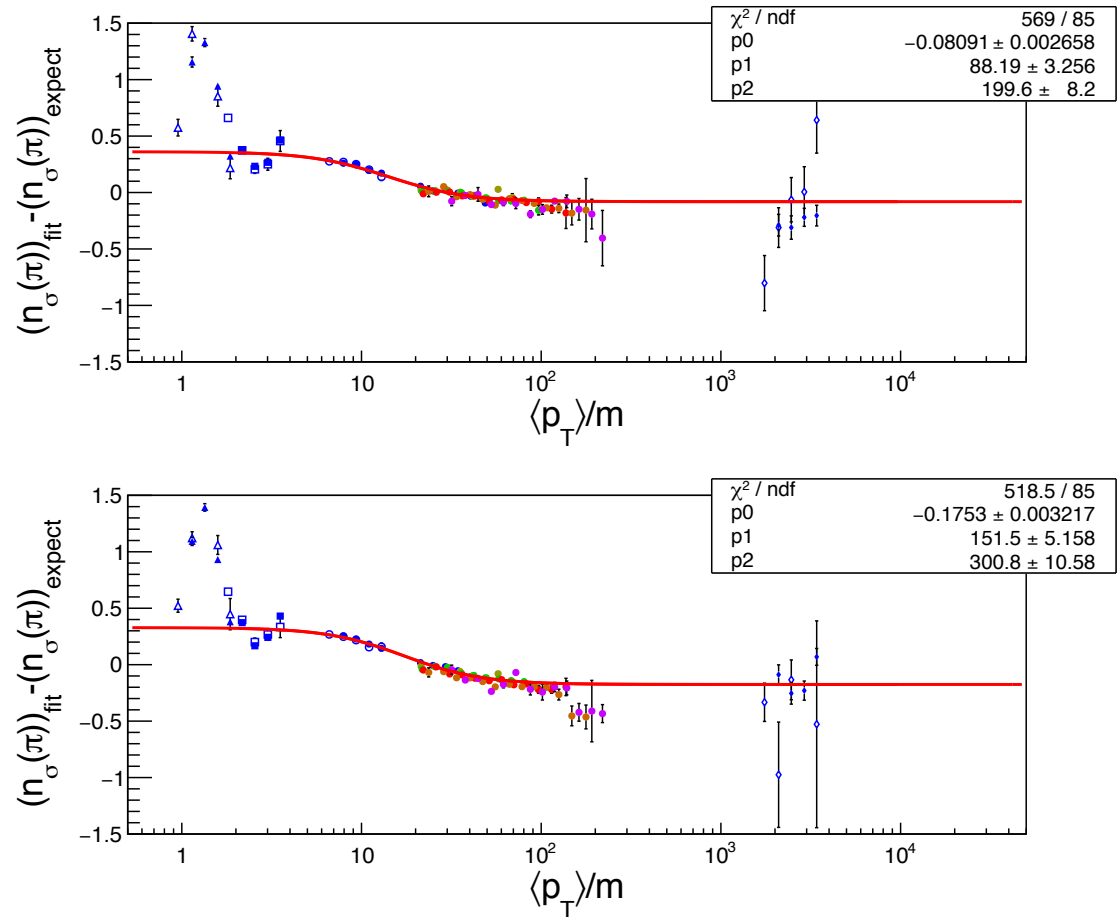


FIG. 25. Deviations from the expected centroids for  $n_\sigma(\pi)$  Gaussian peak fits as a function of track  $\langle p_T \rangle / m$  for (top) positive and (bottom) negatively charged particles. Blue triangles denote centroids from isolated proton distributions, blue squares denote centroids from isolated kaon distributions, blue diamonds denote electron centroids, and blue circles denote isolated pion centroids. Open points are VPDMB, while closed points are jet-patch triggered. The multi-colored points represent pion peak fits from higher kinematics where isolating the various samples is impractical, and the full ensemble of particles is fitted with the pion peak centroids allowed to float. The distribution from  $2 < \langle p_T \rangle / m < 5 \times 10^4$  is fit with a function of the form  $p_0 + p_1 / (p_2 + x^2)$ , following the approach of Ref. [26].

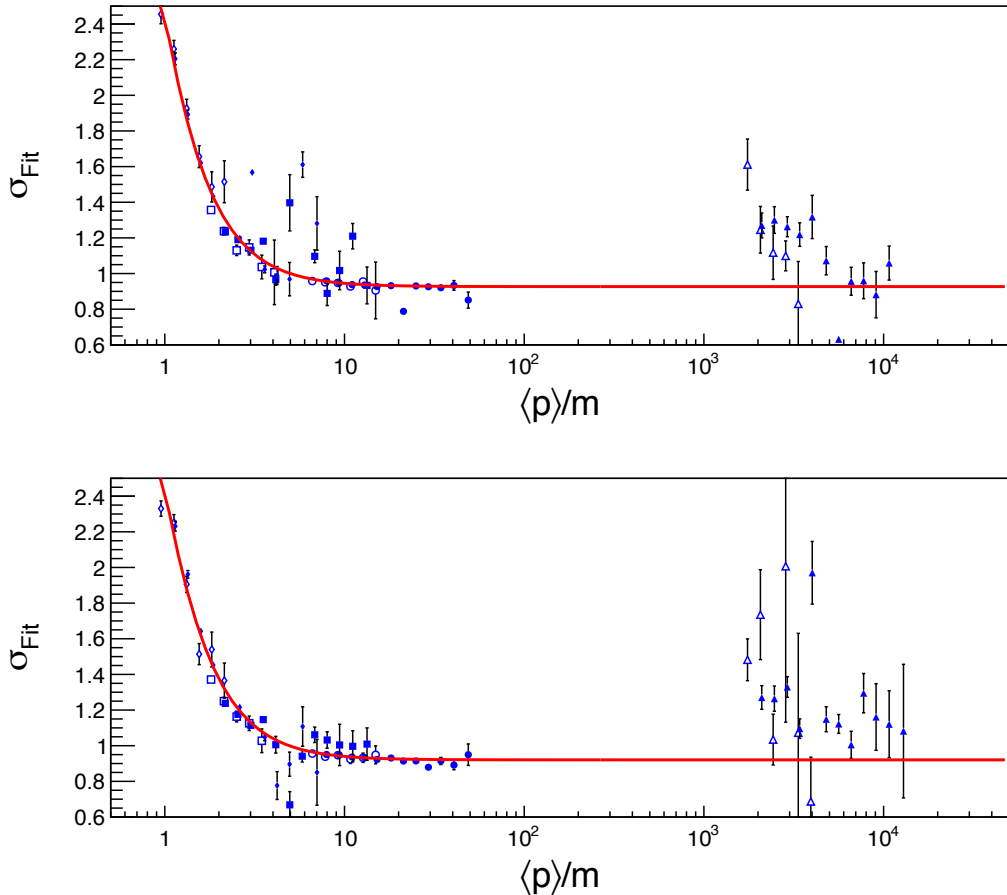


FIG. 26. Gaussian peak  $\sigma_s$  for  $n_\sigma(\pi)$  fits as a function of track momentum divided by mass for (top) positive and (bottom) negatively charged particles with  $0.1 < z < 0.15$ . Triangles denote protons, squares denote kaons, diamonds denote electrons, and circles denote pions. Open points are VPDMB, while closed points are jet-patch triggered. The distribution is fit with a function of the form  $p_0 + p_1 / (p_2 + x^2)$ .

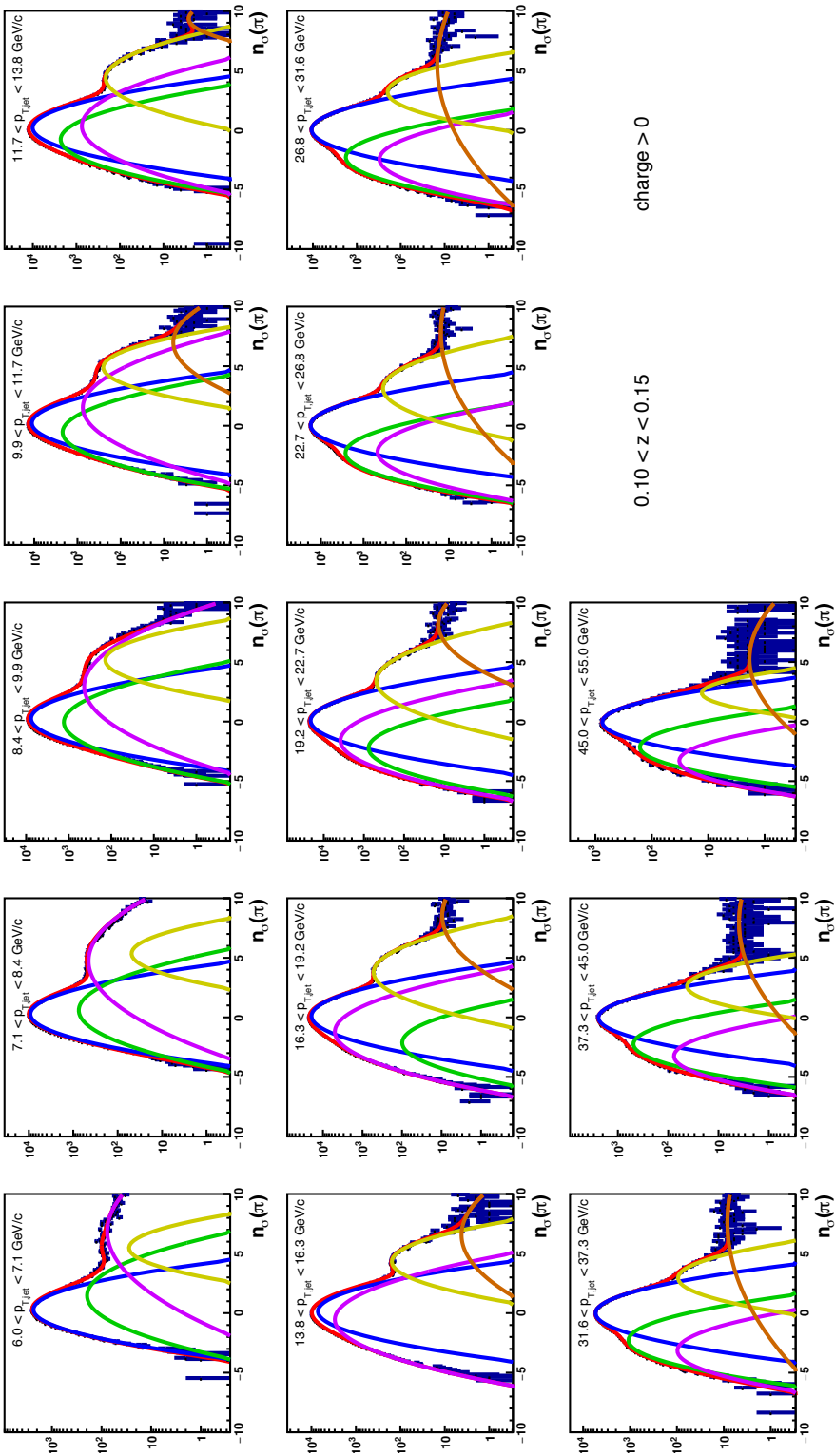


FIG. 27. Multi-Gaussian  $n_\sigma(\pi)$  fits as a function of jet  $p_T$  for positively charged particles with  $0.1 < z < 0.15$ . Individual peaks are shown for pions (blue), kaons (green), protons (violet), electrons (yellow), and merged tracks (orange). The overall fit is shown in red.

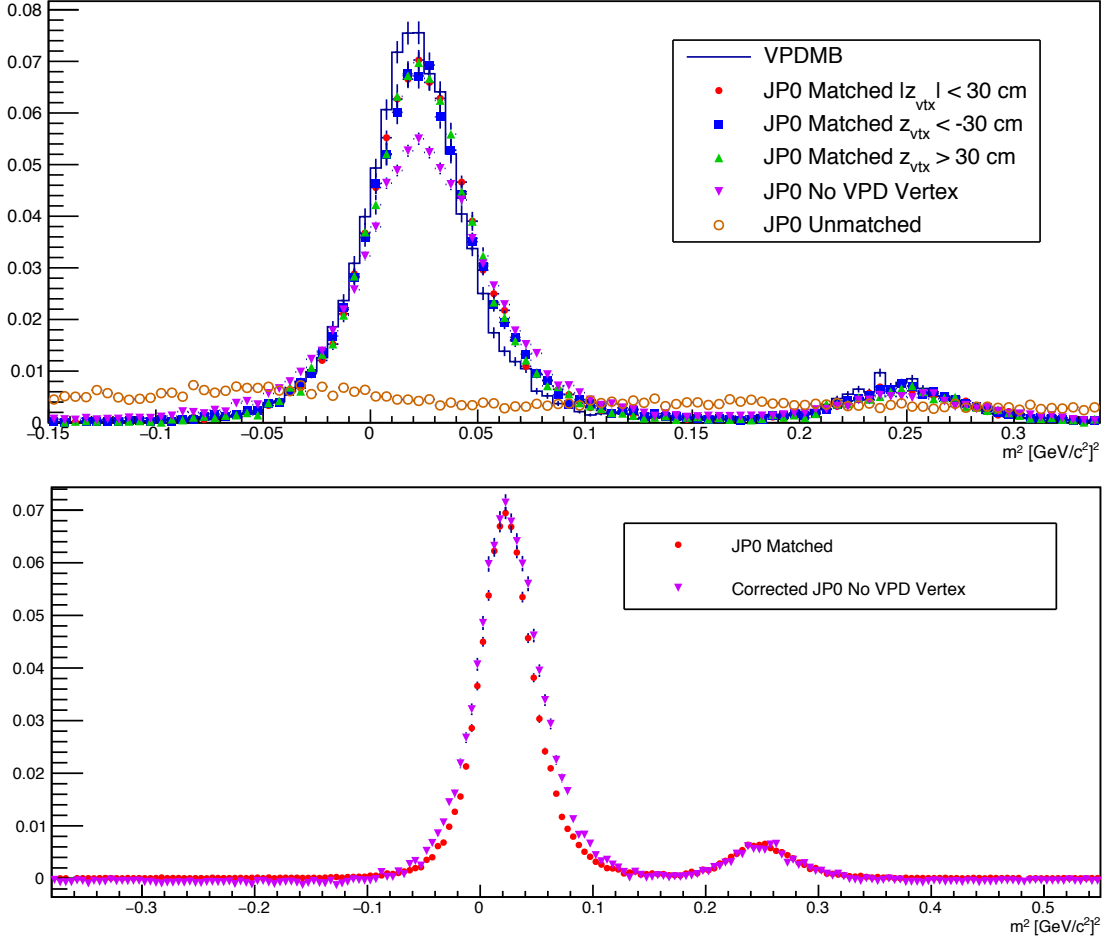


FIG. 28. TOF  $m^2$  distributions for positively charged particles with  $-1 < n_\sigma(\pi) < 2.5$  and  $0.1 < z < 0.15$  from jets with  $7.1 < p_T < 8.4$  GeV/ $c$ . Events are compared between VPDMB and JP triggers with different vertex requirements (top). The no-VPD-vertex events are corrected by renormalizing and subtracting the unmatched distribution. Histograms are normalized to unity.

TOF  $m^2$  distributions are systematically different for VPDMB events and jet-patch-triggered events. An example is shown in Fig. 28. JP distributions tend to be a bit wider than their VPDMB counterparts, even after requiring a matched vertex between the VPD and TPC with the same  $z_{\text{vertex}}$  selection requirements. For this reason, the TOF distributions are analyzed separately for VPDMB and JP events. As a sanity check, JP events reconstructed without a VPD vertex are compared to those with a VPD vertex match after correcting for unmatched vertex events. First, the unmatched distribution is renormalized

for the corresponding number of “no-VPD-vertex” events. Then, the unmatched distribution is subtracted from the no-VPD-vertex distribution. The resulting corrected distribution is compared to the “matched-vertex” distribution in the bottom panel of Fig. 28. The distributions compare very favorably with the corrected distribution slightly wider than the matched distribution. This is easily explained by the fact that the “no-VPD-vertex” events have hits on only a single side of the VPD, while the matched events have hits on two sides and, thus, better timing resolution. For purposes of background estimates only, JP events are required to contain a VPD vertex matched to the TPC vertex.

Ultimately the background correction is done using events from three different ranges of  $n_\sigma(\pi)$ . Therefore, the TOF  $m^2$  fits are done to samples from the three corresponding ranges of  $n_\sigma(\pi)$ . These ranges are chosen as a function of particle momentum and summarized in Table XIX. The ranges were tuned by optimizing the resulting statistical uncertainties for the asymmetries within the various bins. Factors contributing to this are not only the event yields for the three samples but also the associated purities that construct the  $3 \times 3$  matrix to be inverted for the background correction. If this matrix is not sufficiently close to diagonal, the inversion can lead to surprisingly enormous uncertainties. Thus, the tuning procedure is critical. The ranges stabilize once the  $dE/dx$  bands for kaons and protons level off as a function of momentum, thus, above particle momenta of  $\sim 2.1$  GeV/ $c$ , the  $n_\sigma(\pi)$  ranges converge to a single set of three, independent of jet  $p_T$  and pion  $z$ .

Examples of the TOF  $m^2$  fits are shown in Figs. 29, 30, and 31 for VPDMB events and Figs. 32, 33, and 34 for jet-patch triggered events. The fit functions are triple-Voigt-profiles: one each for pions, kaons, and protons. The electron peak is so close to the pions as to be impossible to separate. However, the electron fractions from the  $n_\sigma(\pi)$  fits can be used to correct the pion peaks from TOF. In most cases, the electron contamination is negligible. Each particle species is constrained to have a single set of centroid and width parameters independent of  $n_\sigma(\pi)$ , while the amplitudes are allowed to float. Since the bin yields are occasionally small, the log-likelihood flag is set in the ROOT fits. In cases where the fits will not converge after a few iterations, “analytic uncertainties” are used, where the bin uncertainties are set equal to  $\sqrt{N}$  with  $N$  equal to the value of the fit function rather than the bin entries. In these cases, the fit converges within a few iterations.

The species fractions are determined using both  $n_\sigma(\pi)$  and  $m^2$  distributions. The final

Pion $z$	Jet $p_T$ [GeV/ $c$ ]	Pion-rich $n_\sigma(\pi)$	Kaon-rich $n_\sigma(\pi)$	Proton-rich $n_\sigma(\pi)$
0.1 – 0.15	6 – 7.1	-5 to 1	2 to 6	6 to 10
0.1 – 0.15	7.1 – 8.4	-5 to 1	1.5 to 5	5 to 10
0.1 – 0.15	8.4 – 9.9	-1.5 to 2.5	-5 to -1.5	2.5 to 10
0.1 – 0.15	9.9 – 11.7	-0.7 to 2	-5 to -1.5	2.5 to 10
0.1 – 0.15	11.7 – 13.8	-1 to 1.5	-5 to -1	1.5 to 10
0.1 – 0.15	13.8 – 16.3	-0.5 to 2.5	-2.25 to -1	-5 to -2.25
0.1 – 0.15	16.3 – 19.2	-1 to 2.5	-2.5 to -1.5	-5 to -3
0.1 – 0.15	> 19.2	-1 to 2.5	-2.25 to -1	-5 to -2.25
0.15 – 0.2	6 – 7.1	-1.5 to 2.5	-5 to -1.5	2.5 to 10
0.15 – 0.2	7.1 – 8.4	-0.7 to 2	-5 to -1.5	2.5 to 10
0.15 – 0.2	8.4 – 9.9	-1 to 1.5	-5 to -1	1.5 to 10
0.15 – 0.2	> 9.9	-1 to 2.5	-2.25 to -1	-5 to -2.25
0.2 – 0.3	6 – 7.1	-1 to 1.5	-5 to -2	2 to 10
0.2 – 0.3	7.1 – 8.4	0.5 to 2.5	-3.5 to -0.5	-5 to -3.5
0.2 – 0.3	8.4 – 9.9	-0.1 to 2.5	-3 to -2.5	-5 to -3
0.2 – 0.3	> 9.9	-1 to 2.5	-2.25 to -1	-5 to -2.25
0.3 – 0.4	6 – 7.1	-0.1 to 2.5	-2.5 to -2	-5 to -2.5
0.3 – 0.4	> 7.1	-1 to 2.5	-2.25 to -1	-5 to -2.25
> 0.4	> 6	-1 to 2.5	-2.25 to -1	-5 to -2.25

TABLE XIX. Ranges of  $n_\sigma(\pi)$  for “pion-rich,” “kaon-rich,” and “proton-rich” samples as a function of the various bins of jet  $p_T$  and pion  $z$ .

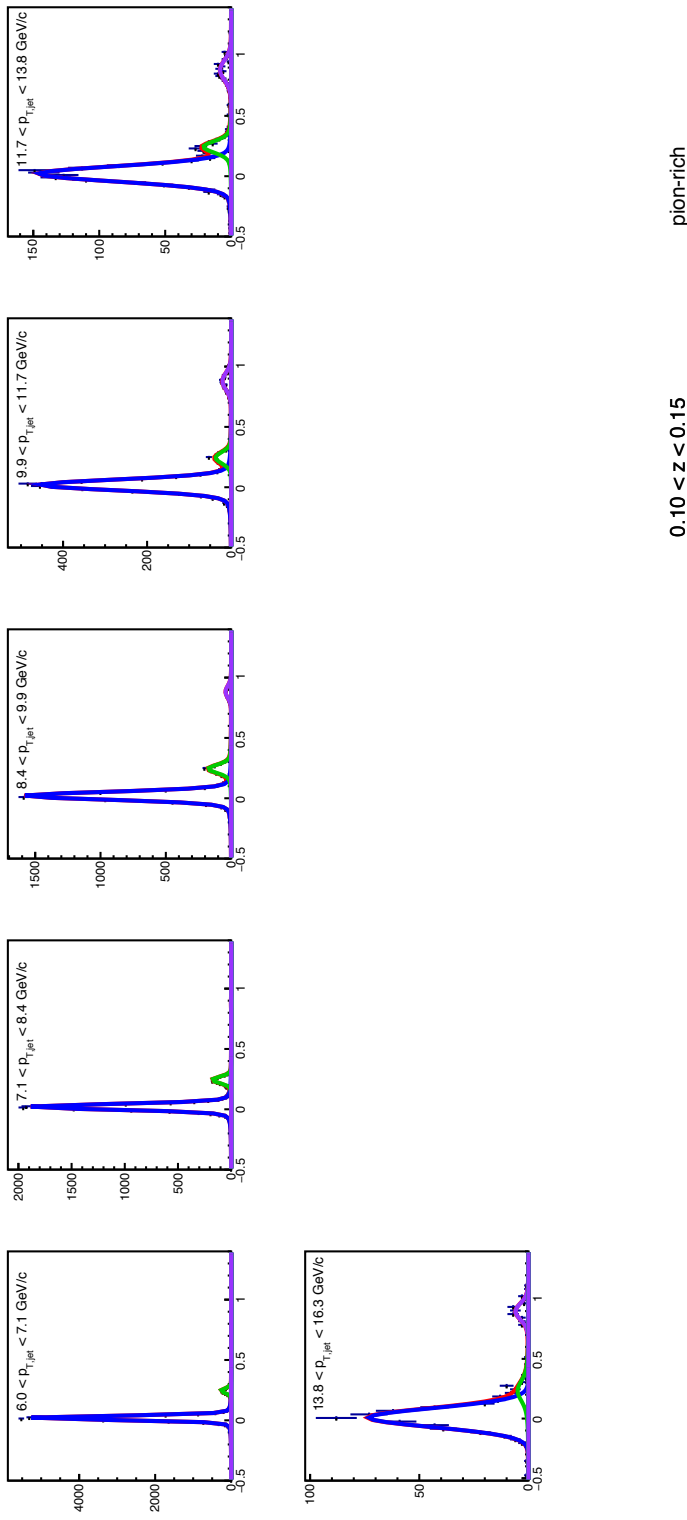


FIG. 29. VPDMB TOF  $m^2$  distributions as a function of jet  $p_T$  for positively charged particles with  $0.1 < z < 0.15$  in the “pion-rich”  $n_\sigma(\pi)$  region. Distributions are fit with a multi-Voigt-profile. Individual peaks are shown for pions (blue), kaons (green), and protons (violet). The overall fit is shown in red.

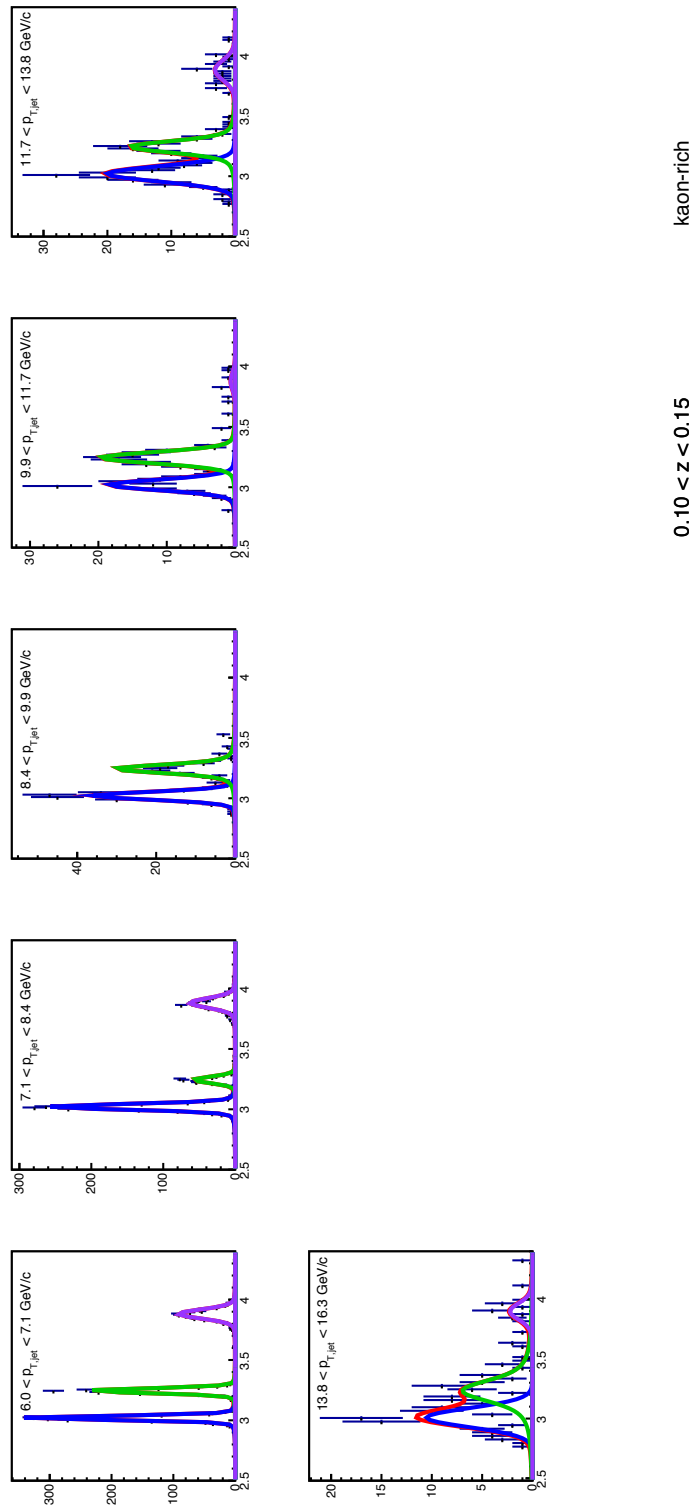


FIG. 30. VPDMB TOF  $m^2$  distributions as a function of jet  $p_T$  for positively charged particles with  $0.1 < z < 0.15$  in the “kaon-rich”  $n_\sigma(\pi)$  region. Distributions are fit with a multi-Voigt-profile. Individual peaks are shown for pions (blue), kaons (green), and protons (violet). The overall fit is shown in red.

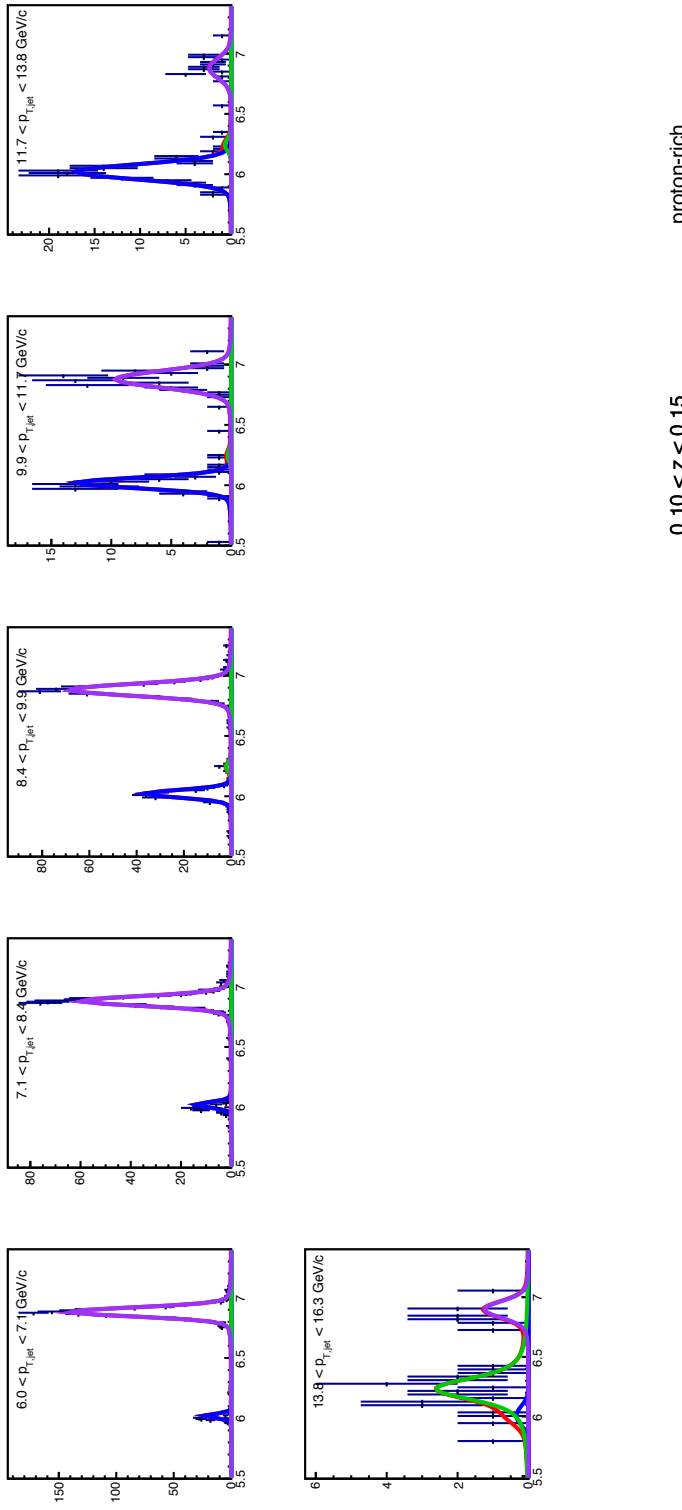


FIG. 31. VPDMB TOF  $m^2$  distributions as a function of jet  $p_T$  for positively charged particles with  $0.1 < z < 0.15$  in the “proton-rich”  $n_\sigma(\pi)$  region. Distributions are fit with a multi-Voigt-profile. Individual peaks are shown for pions (blue), kaons (green), and protons (violet). The overall fit is shown in red.

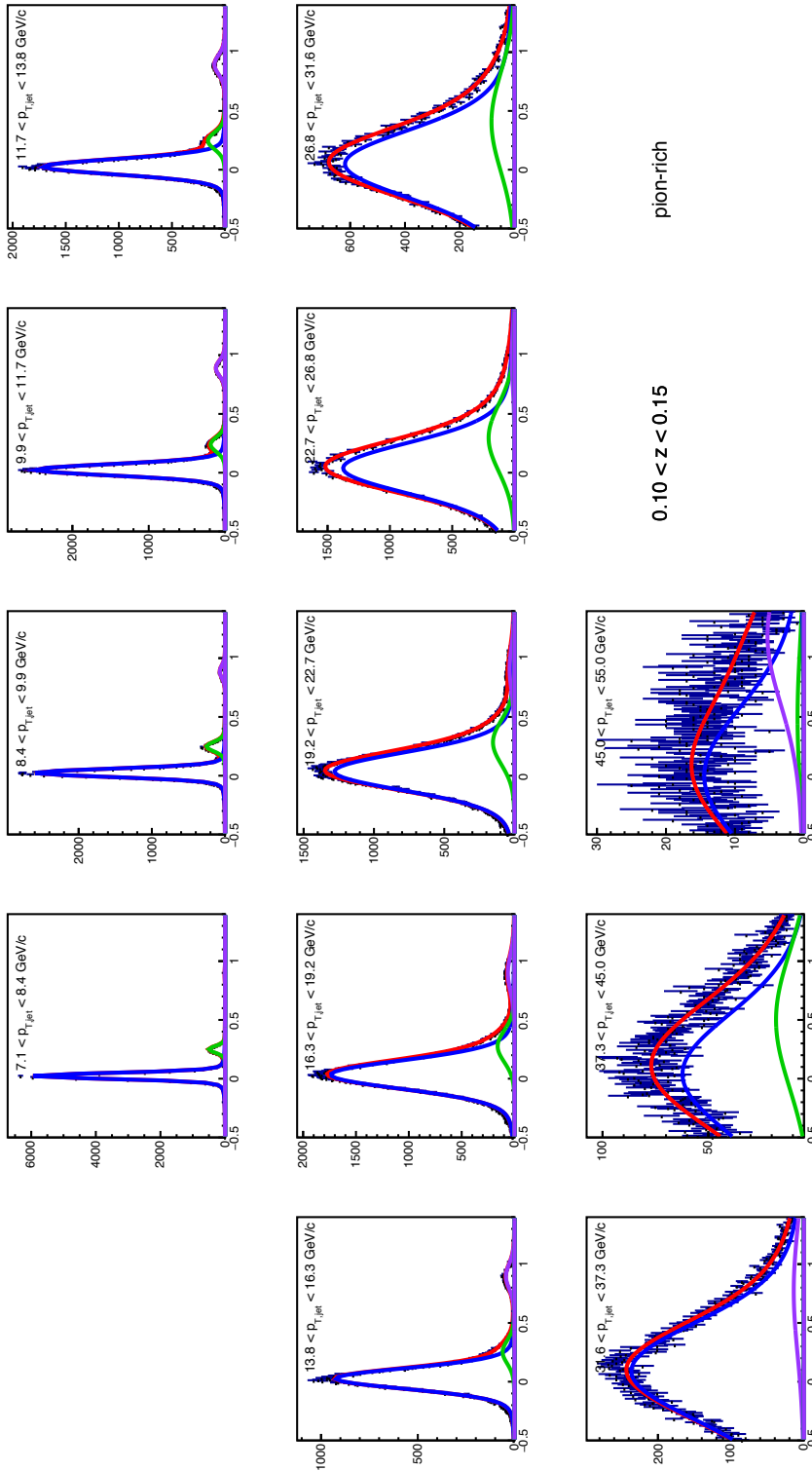


FIG. 32. Jet-patch triggered TOF  $m^2$  distributions as a function of jet  $p_T$  for positively charged particles with  $0.1 < z < 0.15$  in the “pion-rich”  $n_\sigma(\pi)$  region. Distributions are fit with a multi-Voigt-profile. Individual peaks are shown for pions (blue), kaons (green), and protons (violet). The overall fit is shown in red.

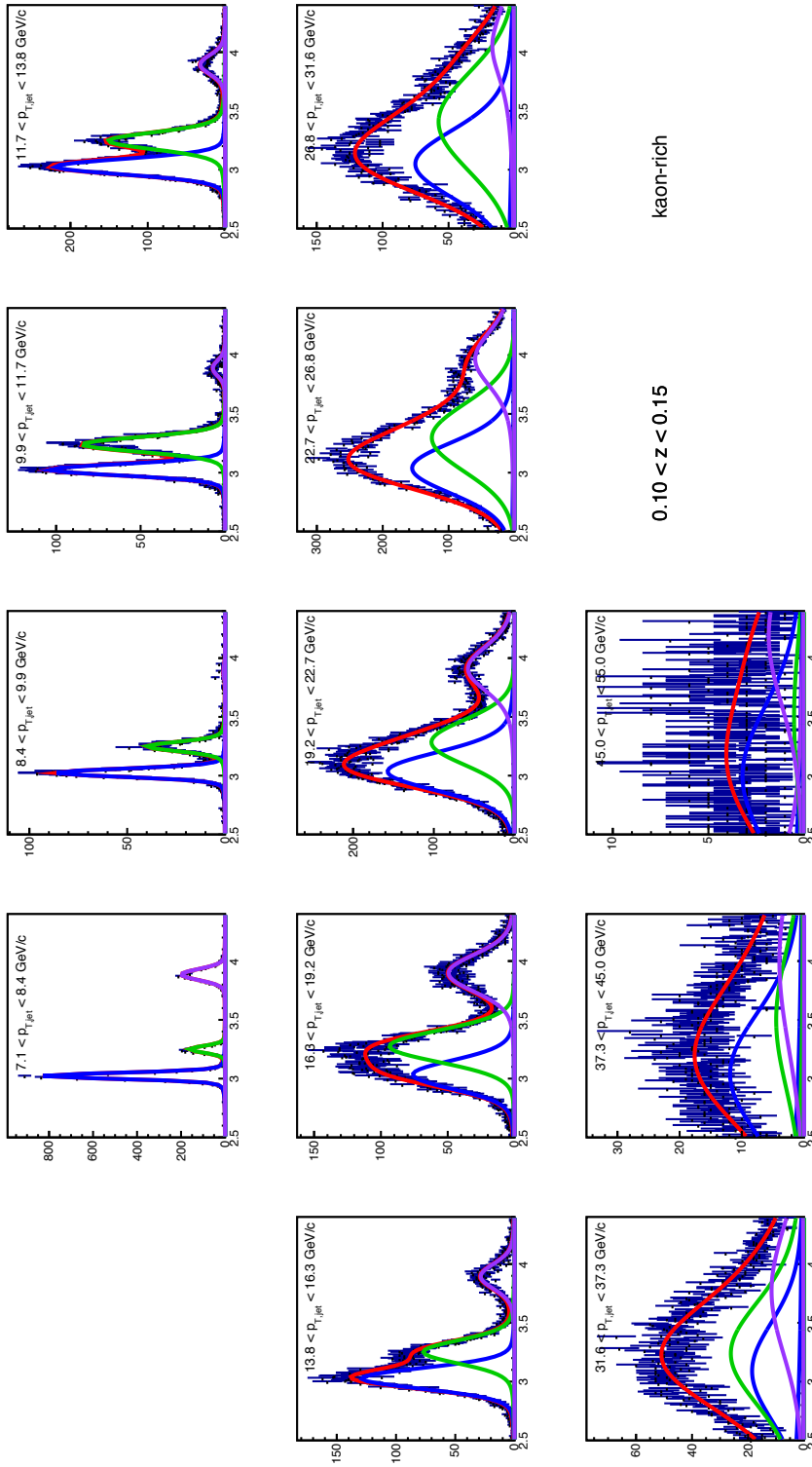


FIG. 33. Jet-patch triggered TOF  $m^2$  distributions as a function of jet  $p_T$  for positively charged particles with  $0.1 < z < 0.15$  in the “kaon-rich”  $n_\sigma(\pi)$  region. Distributions are fit with a multi-Voigt-profile. Individual peaks are shown for pions (blue), kaons (green), and protons (violet). The overall fit is shown in red.

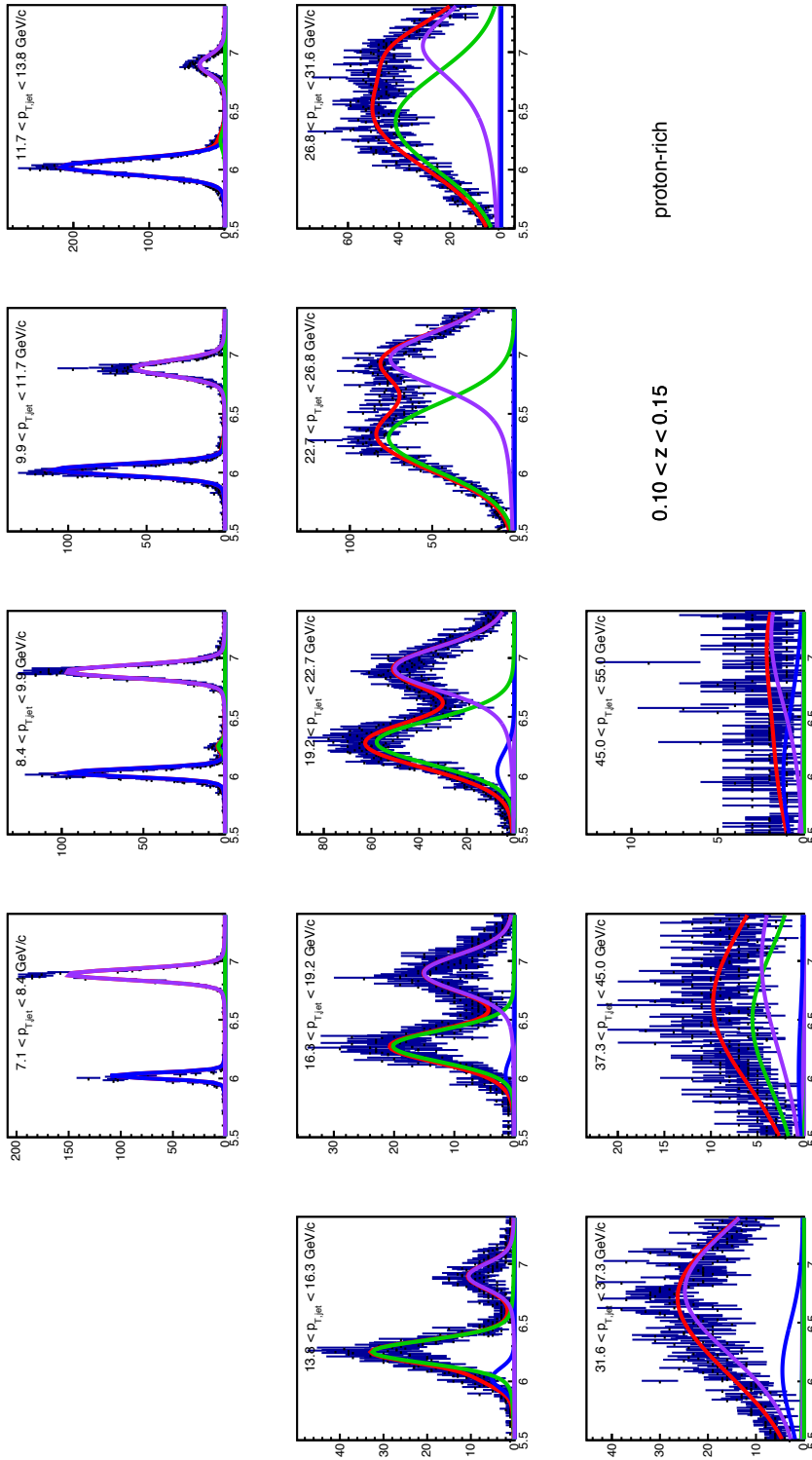


FIG. 34. Jet-patch triggered TOF  $m^2$  distributions as a function of jet  $p_T$  for positively charged particles with  $0.1 < z < 0.15$  in the “proton-rich”  $n_\sigma(\pi)$  region. Distributions are fit with a multi-Voigt-profile. Individual peaks are shown for pions (blue), kaons (green), and protons (violet). The overall fit is shown in red.

species fractions are determined by using the most reliable method for a given particle species in the given kinematic bin. Kaons and pions with a total momentum of  $1.1 \text{ GeV}/c$  experience the same  $dE/dx$  in the STAR TPC, and protons and pions have the same  $dE/dx$  at a total momentum of  $1.7 \text{ GeV}/c$ . The multi-Gaussian  $n_\sigma(\pi)$  fits are insufficient to determine the non-pion backgrounds in the vicinity of these crossovers. For bins of jet  $p_T$  and pion  $z$  corresponding to pion momenta below  $\sim 2.1 \text{ GeV}/c$ , the TOF  $m^2$  distributions are used exclusively to extract the pion, kaon, and proton fractions. For bins corresponding to pion momenta from  $\sim 2.1 - 3.5 \text{ GeV}/c$ , the pion  $dE/dx$  value are well separated from those of from kaons and protons. However, kaons and protons experience the same  $dE/dx$  at these kinematics in the STAR TPC. The  $m^2$  resolution of the STAR TOF is not sufficient to separate pions from kaons at these momenta. Thus, a hybrid approach is used. The  $n_\sigma(\pi)$  fits are used to extract the pion fractions and combined kaon and proton fractions. The isolated proton fractions are extracted from the  $m^2$  distributions, where they are still well separated from pions and kaons. The kaon fractions are then taken from the difference between the combined  $n_\sigma(\pi)$  kaon plus proton fractions and the  $m^2$  proton fractions. For momenta above  $\sim 3.5 \text{ GeV}/c$ , pion, kaon, and proton fractions are extracted exclusively from  $n_\sigma(\pi)$  fits. For all kinematics, electron fractions are determined from  $n_\sigma(\pi)$  fits. In the kinematic regions where the kaon and proton  $dE/dx$  values are similar to those for pions, the kaons and protons contribute a  $\sim 10\%$  background. Outside of these kinematic regions, the kaon and proton backgrounds are typically in the range of  $1 - 2\%$ . Electrons typically contribute  $1\%$  or less. The fractions are calculated in fine bins of  $z$  and jet  $p_T$  and weighted averages of these values are calculated for the appropriate final bins of the asymmetry analysis. For the  $j_T$  dependence, the average values from the appropriate  $z$  bin are used.

The asymmetries for the pion-rich, kaon-rich, and proton-rich ranges can be expressed

$$A_1 = f_1^\pi A_\pi + f_1^K A_K + f_1^p A_p \quad (27)$$

$$A_2 = f_2^\pi A_\pi + f_2^K A_K + f_2^p A_p \quad (28)$$

$$A_3 = f_3^\pi A_\pi + f_3^K A_K + f_3^p A_p. \quad (29)$$

Here,  $A_1$ ,  $A_2$ , and  $A_3$  are the pion-rich, kaon-rich, and proton-rich asymmetries, respectively;  $f_1^\pi$ ,  $f_1^K$ , and  $f_1^p$  are, respectively, the pion, kaon, and proton fractions from the pion-rich

sample;  $f_2^\pi$ ,  $f_2^K$ , and  $f_2^p$  are, respectively, the pion, kaon, and proton fractions from the kaon-rich sample; and  $f_3^\pi$ ,  $f_3^K$ , and  $f_3^p$  are, respectively, the pion, kaon, and proton fractions from the proton-rich sample. The fractions are summarized in Appendix C. The electrons are assumed to contribute no asymmetry. The corrected pion and kaon/proton asymmetries are calculated as

$$A_\pi = \frac{A_1(f_2^K f_3^p - f_3^K f_2^p) + A_2(f_3^K f_1^p - f_1^K f_3^p) + A_3(f_1^K f_2^p - f_2^K f_1^p)}{f_1^\pi f_2^K f_3^p + f_2^\pi f_3^K f_1^p + f_3^\pi f_1^K f_2^p - f_1^\pi f_3^K f_2^p - f_2^\pi f_1^K f_3^p - f_3^\pi f_2^K f_1^p} \quad (30)$$

$$A_K = \frac{A_1(f_2^p f_3^\pi - f_3^p f_2^\pi) + A_2(f_3^p f_1^\pi - f_1^p f_3^\pi) + A_3(f_1^p f_2^\pi - f_2^p f_1^\pi)}{f_1^\pi f_2^K f_3^p + f_2^\pi f_3^K f_1^p + f_3^\pi f_1^K f_2^p - f_1^\pi f_3^K f_2^p - f_2^\pi f_1^K f_3^p - f_3^\pi f_2^K f_1^p} \quad (31)$$

$$A_p = \frac{A_1(f_2^\pi f_3^K - f_3^\pi f_2^K) + A_2(f_3^\pi f_1^K - f_1^\pi f_3^K) + A_3(f_1^\pi f_2^K - f_2^\pi f_1^K)}{f_1^\pi f_2^K f_3^p + f_2^\pi f_3^K f_1^p + f_3^\pi f_1^K f_2^p - f_1^\pi f_3^K f_2^p - f_2^\pi f_1^K f_3^p - f_3^\pi f_2^K f_1^p}. \quad (32)$$

Thus, simultaneously, one may, in principle, extract the pion asymmetry, the kaon asymmetry, and the proton asymmetry from the same set of data. For the present data, the kaon and proton asymmetries do not give a particularly meaningful result in terms of statistical significance. They have been measured but are not proposed as a part of this paper. It should be noted, however, that given the STAR data collected in 2015 and 2017, kaon and proton asymmetries could be extracted at the level of the present pion precision. The statistical uncertainty for the pion result is calculated in two pieces: the piece due to statistical uncertainties on  $A_1$ ,  $A_2$ , and  $A_3$  and the piece due to statistical uncertainties on the species fractions. Both are taken from standard error propagation. The piece due to statistical uncertainties on the signal fraction estimates is somewhat involved to calculate, but it contributes a negligible amount to the total uncertainty.

The systematic uncertainty contribution from the signal fractions is taken by calculating the pion fractions with two different methods and taking the full difference. The uncertainty is then calculated

$$\sigma_{\text{corr}} = |A_{\text{corr}}| \frac{|f_{\pi \text{ comp}} - f_{\pi \text{ nominal}}|}{f_{\pi \text{ nominal}}}. \quad (33)$$

For the region below  $\sim 2.1$  GeV/ $c$ , TOF is used for the central values, thus, the systematic comes from the comparison to the fractions calculated with the  $n_\sigma(\pi)$  distributions. Above  $\sim 2.1$  GeV/ $c$ , the pion fractions are calculated with the  $n_\sigma(\pi)$  distributions and the TOF resolution has significantly degraded. Thus, the systematic comes from the comparison between the nominal fractions and those calculated from the multi-Gaussian fits where the

fit parameters are all allowed to float. In virtually all cases, the associated systematics from species fractions are well under control.

### G. Polarization Uncertainty

As mentioned in Section V, there is an overall systematic of 3.5% for uncertainty in the beam polarization with components from the overall scale and fill-to-fill scale and profile corrections. However, there is also a systematic uncertainty due to the radial component of the beam polarization. Given a polarization offset of  $\delta$ , the transverse asymmetry  $A$  has the following dependence:

$$A \sin(\phi + \delta) = A \cos(\delta) \sin(\phi) + A \sin(\delta) \cos(\phi). \quad (34)$$

Our methodology is to fit the cross-ratios  $\phi$ -bin-by- $\phi$ -bin with a function of the form

$$\epsilon(\phi) = p_0 + p_1 \sin(\phi), \quad (35)$$

where the  $p_1$  term is the extracted asymmetry,  $A$ , and  $p_0$  should scatter statistically about zero. In the presence of an offset,  $\delta$ , an appropriate fit function would be

$$\epsilon(\phi) = p_0 + p_1 \sin(\phi) + p_2 \cos(\phi). \quad (36)$$

In this scenario,  $p_0$  would again scatter about zero; but, now,  $p_1 = A \cos(\delta)$  and  $p_2 = A \sin(\delta)$ . In the limit of uniform acceptance, the event weights for the  $\phi$  bins will be essentially independent of  $\phi$  and the constant, sine, and cosine terms will be orthogonal. Thus, Eq. 35 will for  $p_0$  and  $p_1$  yield the same results as Eq. 36. So, the offset will yield a dilution of  $\cos(\delta) \approx 1 - \delta^2/2$ . The values for  $\delta$  are reported on the ZDC Scaler Polarimetry page [27], and are found to be generally quite small (typically, well within 0.1 radians). Thus, it is assumed that deviations due to non-uniform acceptance will dominate. These introduce a term linear in  $\delta$  which is scaled by a coefficient that approaches zero in the limit of uniform acceptance. If an upper-limit of 0.1 is assumed, this suggests that the radial polarizations cannot impact the asymmetry extraction by more than fractions of a percent. This systematic is, thus, considered negligible.

## IX. ASYMMETRY ANALYSIS

As discussed in Section VI the main asymmetry analysis involves calculating cross-ratio asymmetries for the relevant azimuthal angles in bins of kinematic variables. To facilitate this, events passing all cuts are binned in three sets of histograms: one set for each in bins of  $\phi_S$ ,  $\phi_S - \phi_H$ , and  $\phi_S - 2\phi_H$  (e.g. Fig. 35). From the polarization-weighted yields of these histograms, the desired cross ratios,  $\epsilon$ , are formed as functions of the azimuthal angles in the desired kinematic bins and separated into the various (orthogonal) trigger definitions. The raw asymmetries are extracted using fits of the form

$$\epsilon(\phi) = p_0 + p_1 \sin(\phi), \quad (37)$$

where  $p_1$  is taken as the raw asymmetry. The  $p_0$  term is expected to scatter statistically about zero. It is left in the fit as a useful statistical cross-check for hidden systematics. For instance, the “leak-through” discussed in Section VIIIE can manifest as a constant offset. Thus, including a constant term in the asymmetry extraction can further mitigate the effects of potential “leak-through.” Furthermore, in the ideal limits, the  $p_0$  and  $p_1$  terms are orthogonal; and, thus, nothing is lost statistically by including the parameter in the fits.

In order to be included in the fit each of the four combinations of yields—“spin-up, top-half”; “spin-down, bottom-half”; “spin-up, bottom-half”; and “spin-down, top-half”—are required to have at least 10 counts. Furthermore a kinematic bin is excluded from the fit if any of the azimuthal angle bins (6 total for inclusive jet and 12 total for Collins(-like)) are “unpopulated,” i.e. less than 10 counts in any of the four yield combinations.

As shown in Fig. 35, the cross-ratios can be constructed to calculate asymmetries in the physics observable, instrumental acceptance, and beam luminosity

$$\epsilon = \frac{\sqrt{N_\alpha^\uparrow N_\beta^\downarrow} - \sqrt{N_\alpha^\downarrow N_\beta^\uparrow}}{\sqrt{N_\alpha^\uparrow N_\beta^\downarrow} + \sqrt{N_\alpha^\downarrow N_\beta^\uparrow}} \quad (38)$$

$$\mathcal{I} = \frac{\sqrt{N_\alpha^\uparrow N_\alpha^\downarrow} - \sqrt{N_\beta^\downarrow N_\beta^\uparrow}}{\sqrt{N_\alpha^\uparrow N_\alpha^\downarrow} + \sqrt{N_\beta^\downarrow N_\beta^\uparrow}} \quad (39)$$

$$\mathcal{L} = \frac{\sqrt{N_\alpha^\uparrow N_\beta^\uparrow} - \sqrt{N_\alpha^\downarrow N_\beta^\downarrow}}{\sqrt{N_\alpha^\uparrow N_\beta^\uparrow} + \sqrt{N_\alpha^\downarrow N_\beta^\downarrow}}, \quad (40)$$

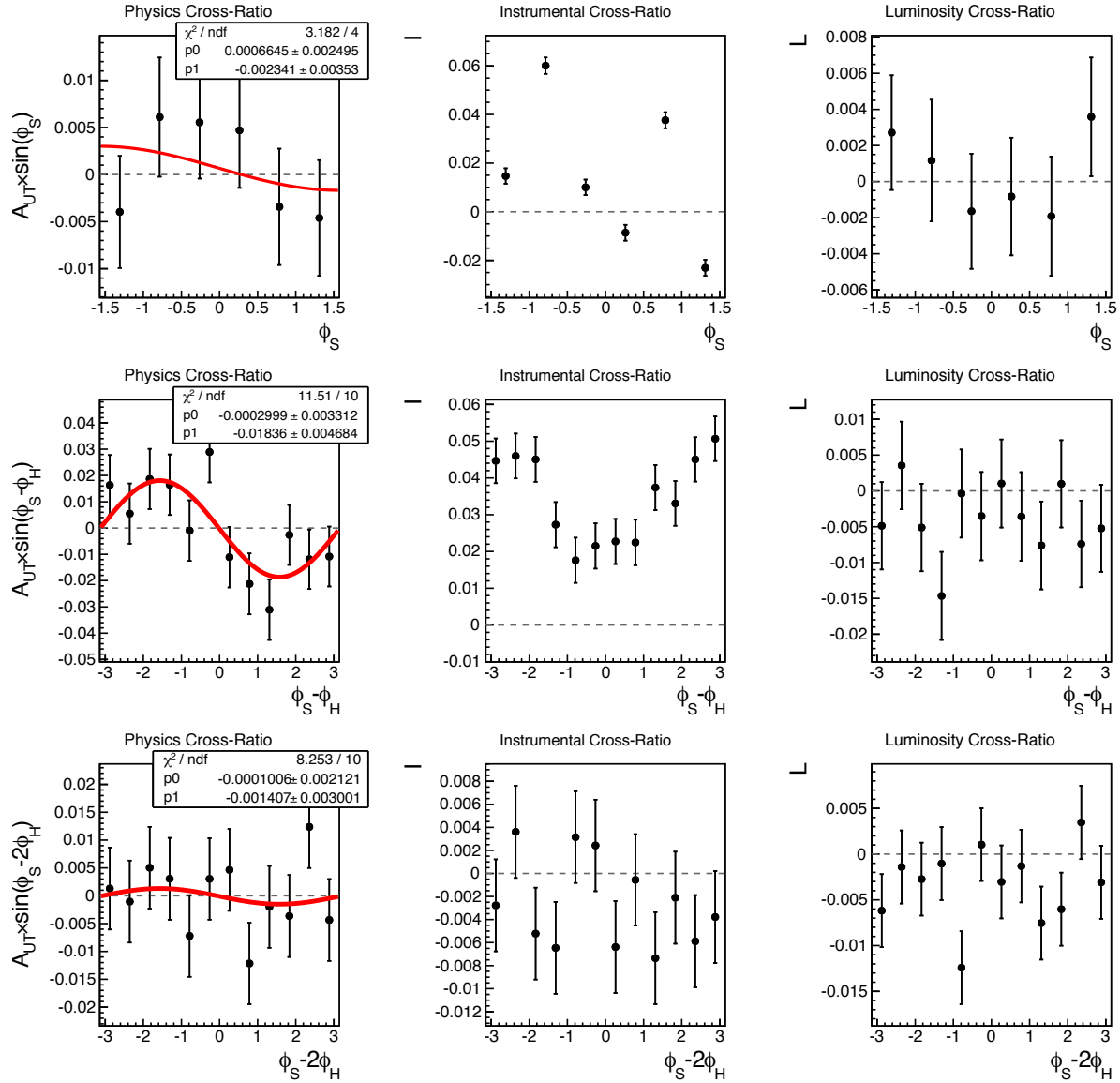


FIG. 35. Examples of physics, instrumental, and luminosity cross-ratios for (top) inclusive jets with JP2 triggers,  $22.7 < p_T < 26.8$  GeV/ $c$ , and  $0.5 < \eta_{\text{jet}} < 1$ ; (middle)  $\pi^+$  Collins with JP2 triggers,  $22.7 < p_{T \text{ jet}} < 55$  GeV/ $c$ ,  $0.5 < \eta_{\text{jet}} < 1$ , and  $0.2 < z < 0.3$ ; and (bottom)  $\pi^+ + \pi^-$  Collins-like with VPDMB triggers,  $6 < p_{T \text{ jet}} < 13.8$  GeV/ $c$ ,  $|\eta_{\text{jet}}| < 1$ , and  $0.1 < z < 0.2$ .

where  $\epsilon$ ,  $\mathcal{I}$ , and  $\mathcal{L}$  represent the physics, instrumental, and luminosity cross ratios, respectively.  $\mathcal{I}$  and  $\mathcal{L}$  can be used to evaluate assumptions about systematics that depend upon instrumental and luminosity effects, for example, as discussed in Section VIII E. For this purpose, while the physics cross ratios are polarization-weighted, the instrumental and luminosity cross ratios only utilize the unweighted yields. From the instrumental cross ratios, one observes that while the acceptance is not perfectly uniform, the bin-by-bin fluctuations fall below the level of 10%, indicating that assumptions about small instrumental asymmetries are well-justified. One expects that luminosity asymmetries should be relatively constant, but perhaps not exactly zero. From the luminosity cross ratios one observes effects below the level of  $\sim 1\%$ , and thus systematics depending upon asymmetries in luminosity are considered negligible.

The trigger-separated raw asymmetries are each corrected for dilution from finite azimuthal resolution. These resolution-corrected asymmetries are, then, combined in a weighted average over all the triggers. The averaged asymmetries are further corrected for finite binning dilutions and, in the case of Collins and Collins-like, dilutions from kaon/proton and electron contamination. These final asymmetries are, then, used to calculate the systematics from trigger bias and, where relevant, contamination to the pion sample.

### A. Statistical Cross-checks

For the final results, the asymmetry fits are performed trigger-by-trigger on data summing over all fills and TPC halves. This allows for the best statistical precision in the asymmetry extraction. Fits are only performed if all azimuthal angle bins for the relevant effect (12 for Collins and Collins-like; 6 for inclusive jet) are “populated,” and azimuthal angle bins are only populated if each of the four cross-ratio yields contain 10 events. Thus, parsing the data over TPC half and fill will systematically exclude events from shorter fills, especially closer to the higher kinematic limits where events become more scarce. However, examining the fits performed separately for fill and TPC half can enable useful statistical cross-checks for hidden systematic effects. The present analysis utilizes three statistical studies:  $\chi^2$  distribution of the asymmetry fits, residual distributions for the mean asymmetry, and residual distribution

for the mean  $p_0$  parameter of the asymmetry fit.

An example of the asymmetry fit  $\chi^2$  distribution is presented in Fig. 36 for the high- $p_T$  Collins asymmetry. For each fit performed in the analysis a histogram of the  $\chi^2$  values is stored. Combining the histograms for all fills, triggers, and TPC halves, one can determine if the distribution is consistent with what one expects for the given degrees of freedom,  $\nu$ , in the fit. To determine this, the  $\chi_{\text{Fit}}^2$  histogram is fit with a  $\chi^2$  function with floating parameters the overall scale and  $\nu$ . For the example shown in Fig. 36, the  $\chi_{\text{Fit}}^2$  values are distributed in a manner consistent with a  $\chi^2$  function, as evidenced by the probability of the fit to the  $\chi_{\text{Fit}}^2$  distribution. Furthermore, the values for  $\nu$  found by the fits are all consistent with the expectation of 10 from the number of angle bins (12) and the number of constraints in the asymmetry fits (2). The implications of this are that the data are statistically scattered about the asymmetry fit function,  $p_0 + p_1 \sin \phi$ , with uncertainties that do not appear to be underestimated. This suggests that it is unlikely that such effects as “leak-through” are distorting the sinusoidal dependence of the desired effects, and the presently assigned systematic should be more than sufficient. Similarly, for the inclusive jet asymmetry, the  $\chi^2$  distributions are well-behaved and consistent with the expectation of  $\nu = 4$ ; while the Collins-like distributions are well-behaved and consistent with the expectation of  $\nu = 10$ .

An example of the asymmetry residual distribution is shown in Fig. 37 for the high- $p_T$  Collins asymmetry for pions with  $0.2 < z < 0.3$ . One expects for a statistical scatter, the residual distribution can be described by a Gaussian function centered at zero with unit  $\sigma$ . For the high- $p_T$  Collins asymmetries and the inclusive jet asymmetries, this is indeed the case. For the Collins-like asymmetries at low- $p_T$ , there are a couple of bins for which the widths of the residual Gaussian appears to be larger than expected. For  $0.2 < z < 0.3$  and  $\eta_{\text{jet}} > 0$ , the weighted average returns  $\chi^2/\nu = 268.6/219$  for a probability of 0.012. The Gaussian fit to the residual distribution returns  $\sigma = 1.123 \pm 0.068$ . Similarly for  $0.3 < z < 0.4$  and  $\eta_{\text{jet}} < 0$ , the weighted average returns  $\chi^2/\nu = 112.6/83$  for a probability of 0.017. The Gaussian fit to the residual distribution returns  $\sigma = 1.215 \pm 0.191$ . This may suggest that the raw uncertainties are slightly underestimated for these two bins. These occur in a region where systematics are known to be a bit larger due to azimuthal angle resolution and underlying event effects. Thus, the current set of corrections and systematic uncertainties are likely sufficient to account for any underestimation in the raw uncertainties.

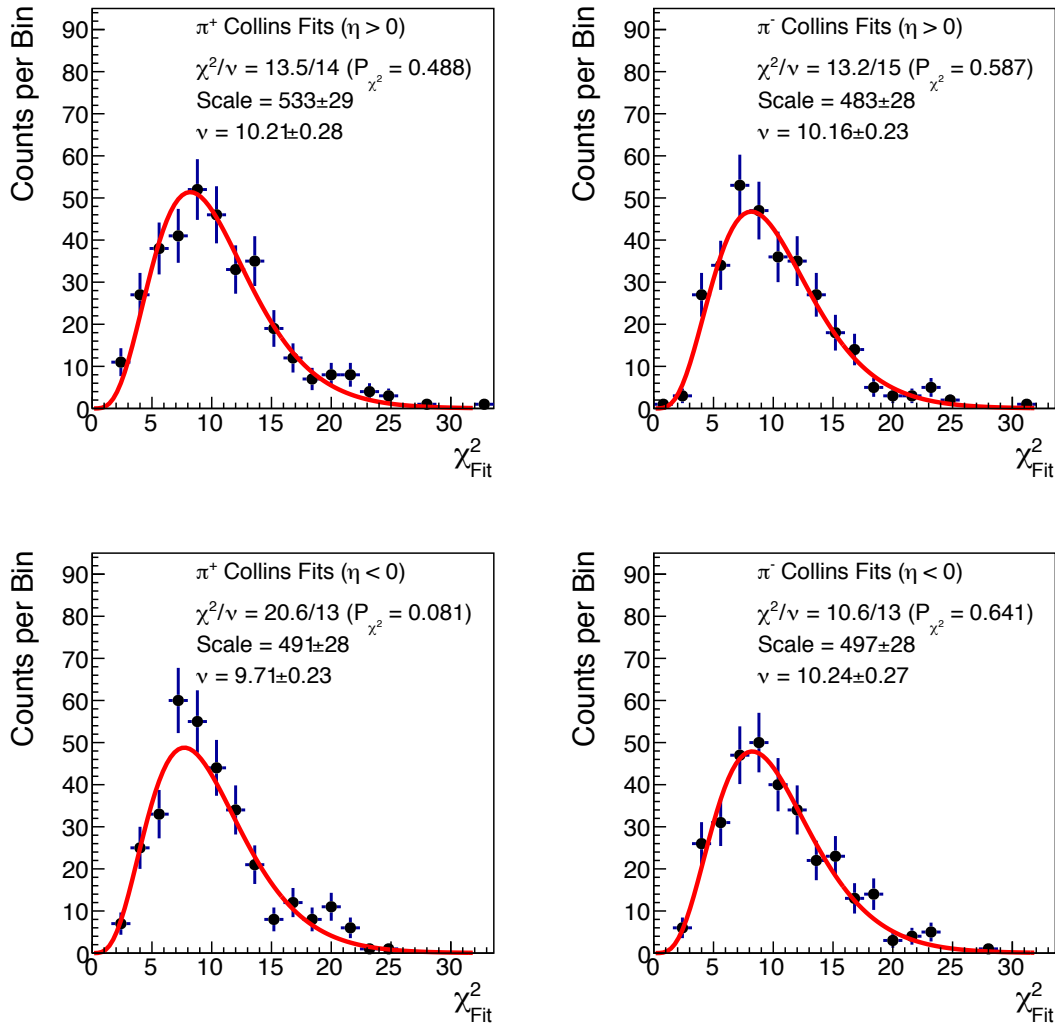


FIG. 36.  $\chi^2$  distributions for high- $p_T$  Collins asymmetry fits as a function of pion  $z$ . Fits are performed for events separated by fill, trigger, and TPC-half. The distributions are shown for (top left)  $\pi^+$ ,  $\eta_{\text{jet}} > 0$ ; (top right)  $\pi^-$ ,  $\eta_{\text{jet}} > 0$ ; (bottom left)  $\pi^+$ ,  $\eta_{\text{jet}} < 0$ ; and (bottom right)  $\pi^-$ ,  $\eta_{\text{jet}} < 0$ . The resulting  $\chi^2$  distributions are fit with a  $\chi^2$  function with floating parameters for the overall scale and the number of degrees of freedom,  $\nu$ . The  $\chi^2$  fits find values for  $\nu$  consistent with the expectation of 10 from the 12 azimuthal bins and two constraints from the asymmetry fit function.

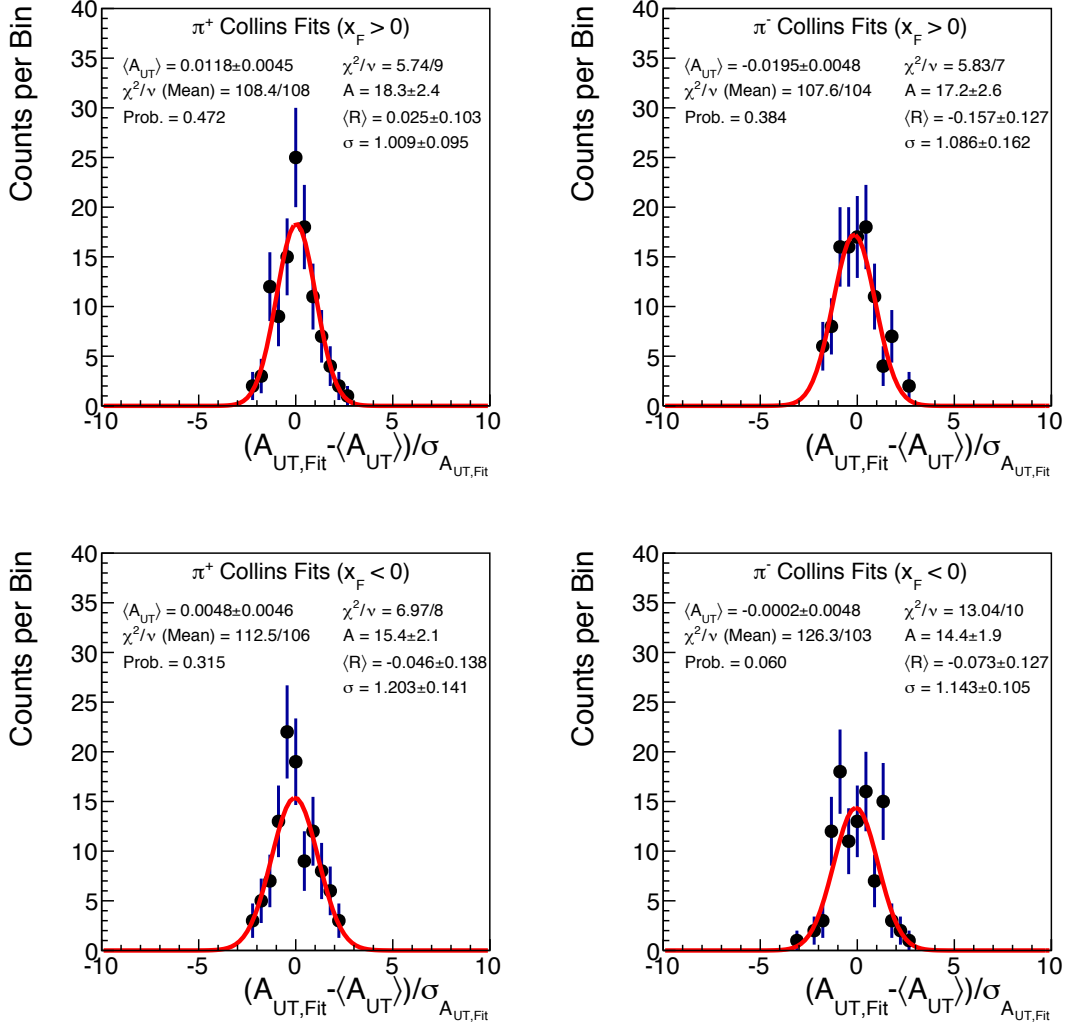


FIG. 37. Collins asymmetry residual distributions for pions with  $0.2 < z < 0.3$ . Fits are performed for events separated by fill, trigger, and TPC-half. The distributions are shown for (top left)  $\pi^+$ ,  $\eta_{jet} > 0$ ; (top right)  $\pi^-$ ,  $\eta_{jet} > 0$ ; (bottom left)  $\pi^+$ ,  $\eta_{jet} < 0$ ; and (bottom right)  $\pi^-$ ,  $\eta_{jet} < 0$ . The mean asymmetries,  $\chi^2$ , and  $\chi^2$ -probabilities are shown in text on the left side of the figures. The resulting residual distributions are fit with a Gaussian function with floating centroid and  $\sigma$ . The results of the Gaussian fits are shown in text on the right side of the figures.

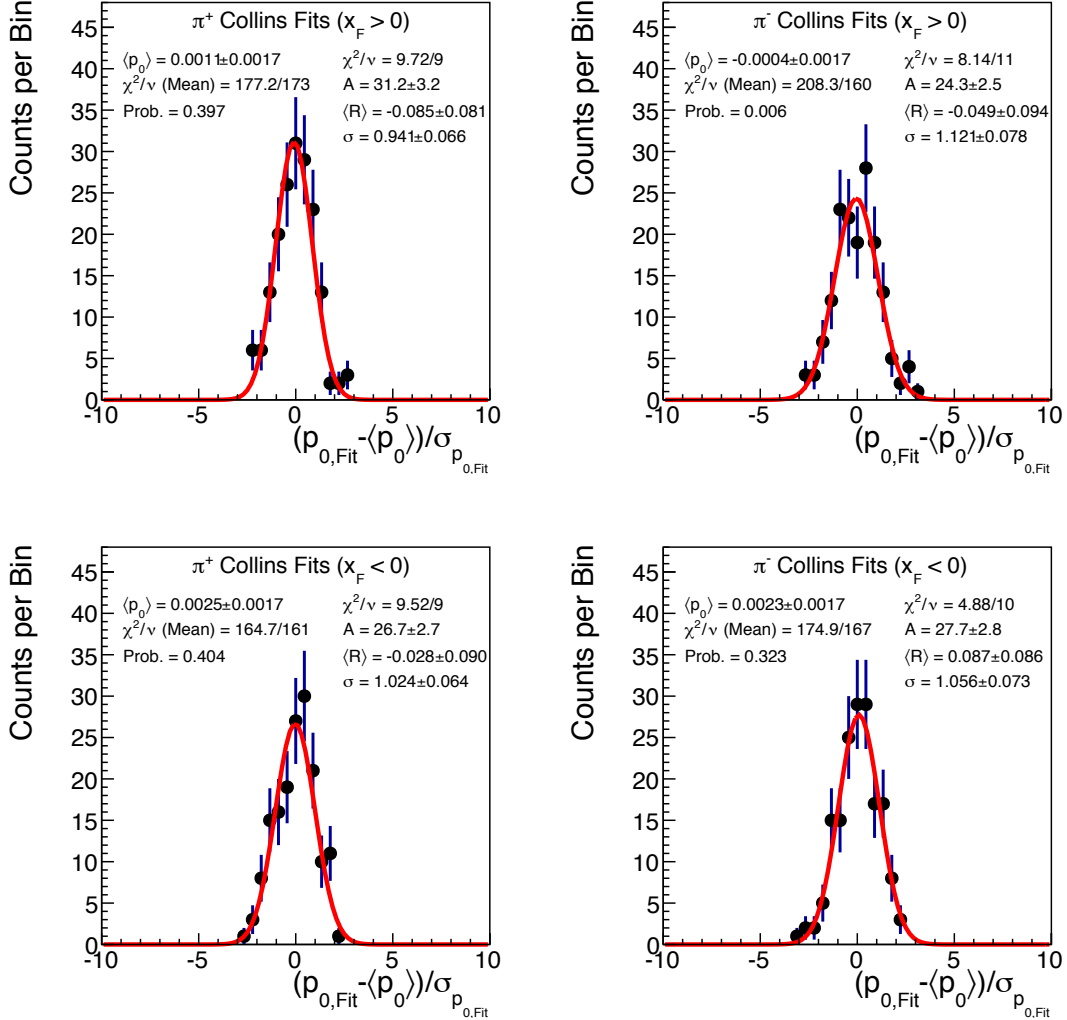


FIG. 38.  $p_0$  residual distributions for Collins asymmetry fits of pions with  $0.1 < z < 0.2$ . Fits are performed for events separated by fill, trigger, and TPC-half. The distributions are shown for (top left)  $\pi^+$ ,  $\eta_{jet} > 0$ ; (top right)  $\pi^-$ ,  $\eta_{jet} > 0$ ; (bottom left)  $\pi^+$ ,  $\eta_{jet} < 0$ ; and (bottom right)  $\pi^-$ ,  $\eta_{jet} < 0$ . The mean  $p_0$ ,  $\chi^2$ , and  $\chi^2$ -probabilities are shown in text on the left side of the figures. The resulting residual distributions are fit with a Gaussian function with floating centroid and  $\sigma$ . The results of the Gaussian fits are shown in text on the right side of the figures.

An example of the  $p_0$  residual distribution is shown in Fig. 38 for the high- $p_T$  Collins asymmetry for pions with  $0.1 < z < 0.2$ . Again, one expects for a statistical scatter, the residual distribution can be described by a Gaussian function centered at zero with unit  $\sigma$ . Further, one expects that the mean for the  $p_0$  should be consistent with zero, in the absence of systematic effects, such as “leak-through.” Across the board, fits for all effects return average  $p_0$ s consistent with zero. Occasionally, however, the residual distributions show widths slightly large than unity. One can see in Fig. 38 that the bin for  $\pi^-$  and  $\eta_{\text{jet}} > 0$  returns a large  $\chi^2$  for the weighted mean calculation and the Gaussian fit to the residual suggests a width a bit larger than unity. For the Collins-like asymmetries at low- $p_T$ , there are several bins with similar behavior, while the inclusive jet  $p_0$ s all behave as expected. This may, again, suggest that the raw uncertainties are slightly underestimated for the  $p_0$ s. In the ideal limits, however, the uncertainties for the  $p_0$ s and the asymmetry extractions should be uncorrelated. Furthermore, in cases where the  $p_0$ s are not well behaved, the asymmetries seem uniformly unperturbed. Thus, while these  $p_0$  features are perhaps suggestive of the presence of systematic effects, such as acceptance, it is not expected that these are contributing hidden systematics to the asymmetry extractions.

## B. Results

Final results for the inclusive-jet, Collins, and Collins-like asymmetries are presented in Figs. 39-46. In all plots, the statistical uncertainties are shown with error bars and systematic uncertainties are shown with shaded error boxes. The width of the boxes indicates the total uncertainty in the kinematic variables which are corrected to the PYTHIA “particle” level. For all results, the jet pseudorapidity is calculated relative to the polarized beam. In the case of Collins and Collins-like asymmetries  $\pi^+$  is shown with closed circles,  $\pi^-$  with open circles, and the combination in closed diamonds. An polarization uncertainty scale systematic of 3.5% for all measurements is not shown.

### 1. Inclusive Jet Asymmetry

In Fig. 39 the final inclusive jet asymmetries are presented. The asymmetries are binned in terms of the jet transverse momentum and presented in separate ranges of jet pseudorapidity,

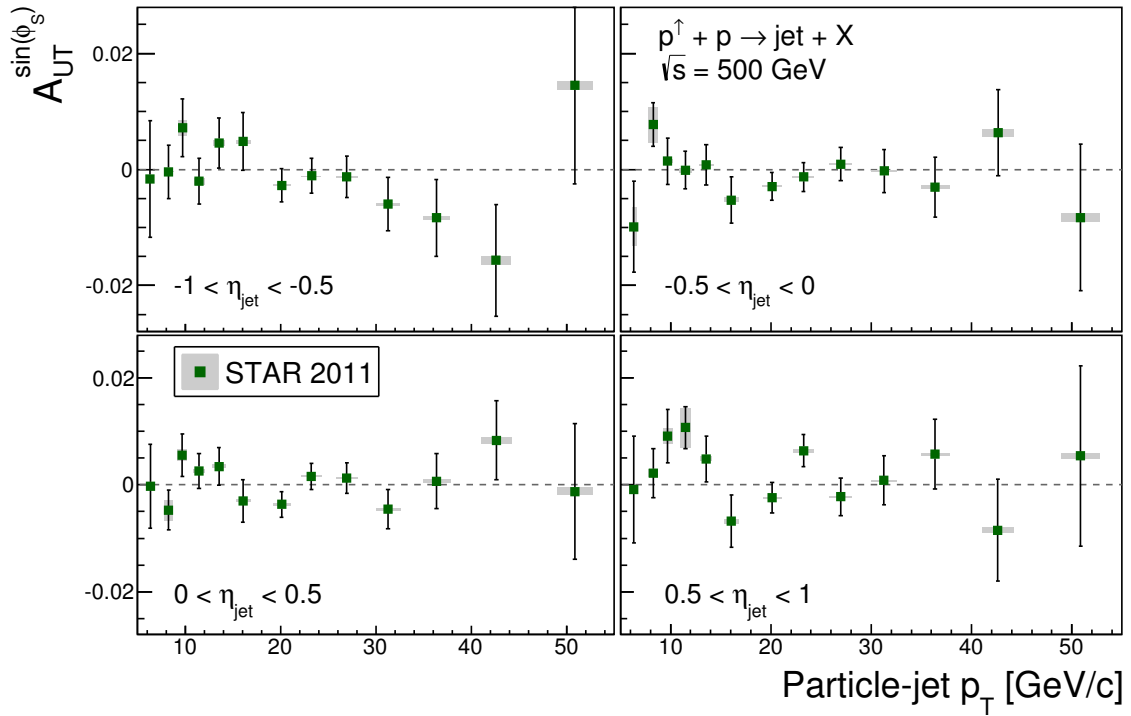


FIG. 39. Final inclusive jet asymmetries as a function of particle-jet  $p_T$ . Statistical uncertainties are shown as error bars, while systematic uncertainties are shown as shaded error boxes. Events are separated into different regions of jet  $\eta$ , calculated relative to the polarized beam.

as measured relative to the polarized beam. A dashed line at zero is provided to guide the eye. In all cases, the results are consistent with small asymmetries, as seen in previous inclusive jet asymmetries measured from  $\sqrt{s} = 200$  GeV collisions [20, 28]. The present data are statistics limited with dominant systematics arising from parton-jet matching probabilities at low values of  $p_T$ . At higher values of  $p_T$  contributions from “leak-through” and trigger bias play a more significant role, however, the effects are typically at or below 10% of the statistical uncertainty.

The inclusive-jet asymmetry is sensitive to the twist-3 PDF [4, 5] related to the  $k_T$ -integrated Sivers function [6, 7]. As the jet  $p_T$  increases, the sensitivity to partonic subprocesses changes [29]. At low jet  $p_T$ , the results are more sensitive to gluonic subprocesses, while sensitivity to quark-based subprocesses increases at high jet  $p_T$ . Thus the asymmetries at lower values of jet  $p_T$  should place constraints on twist-3 PDFs for gluonic interactions

(connected to the gluon Sivers function). As Fig. 18 indicates, the lowest jet  $p_T$  bins extend sensitivity to  $x_G \sim 0.01$ ; while the highest bins probe  $x_Q \sim 0.2$  for unpolarized  $x$ .

## 2. Collins-like Asymmetry

Final results for Collins-like asymmetries are presented in terms of particle-jet  $p_T$  (Fig. 40 and 41) and pion  $z$  (Fig. 42 and 43). Since the subprocess fraction changes as a function of jet  $p_T$ , it is informative to examine how the asymmetries depend on  $p_T$ . The Collins-like asymmetry is expected to arise from gluon linear polarization; thus, the best sensitivity should reside at lower values of jet  $p_T$ . Figure 40 shows the asymmetry as a function of jet  $p_T$  for different ranges of jet  $\eta$  and pion  $z$ . Across the board, the asymmetries are consistently small. The dominant uncertainties are statistical with systematics well under control. The dominant systematics arise from the parton-jet matching probabilities at low- $p_T$  and “leak-through” at mid-to-high values of  $p_T$ .

From Ref. [9], the maximized projections allow for the largest effects at lower values of both jet  $p_T$  and pion  $z$ . Furthermore, the maximized projections are similar for  $\pi^+$  and  $\pi^-$  and for  $\eta_{\text{jet}} > 0$  and  $\eta_{\text{jet}} < 0$ . Thus, in Fig. 41, the Collins-like asymmetries are presented as a function of jet  $p_T$  for  $0.1 < z < 0.3$  combining pion flavors and integrating over the full range of  $-1 < \eta_{\text{jet}} < 1$ . Again, the dominant uncertainties are from statistics with the leading systematic arising from parton-jet matching probability at low- $p_T$ . The size of the maximal projections tends to be around 2%. Combining the results of the first two bins of  $p_T$ , the measured asymmetry is  $0.0082 \pm 0.0050$ , setting the limit of the 95% confidence level at 0.0179.

In Fig. 42 the Collins-like asymmetries are shown as a function of pion  $z$  in bins of jet pseudorapidity and jet  $p_T$ . The data do not show large asymmetries at the present level of precision with systematics well under control.

Since, as discussed previously, models indicate the largest possible effects at low values of jet  $p_T$  the asymmetries are presented in Fig. 43 as a function of pion  $z$  for  $6 < p_{T,\text{jet}} < 13.8$  GeV/ $c$  combining  $\pi^+$  and  $\pi^-$  and integrating over the range  $-1 < \eta_{\text{jet}} < 1$ . The largest effects are expected to occur at lower values of  $z$  where the available statistics are quite large. Combining the results of the first two bins of  $z$ , the measured asymmetry is  $0.0039 \pm 0.0019$ ,

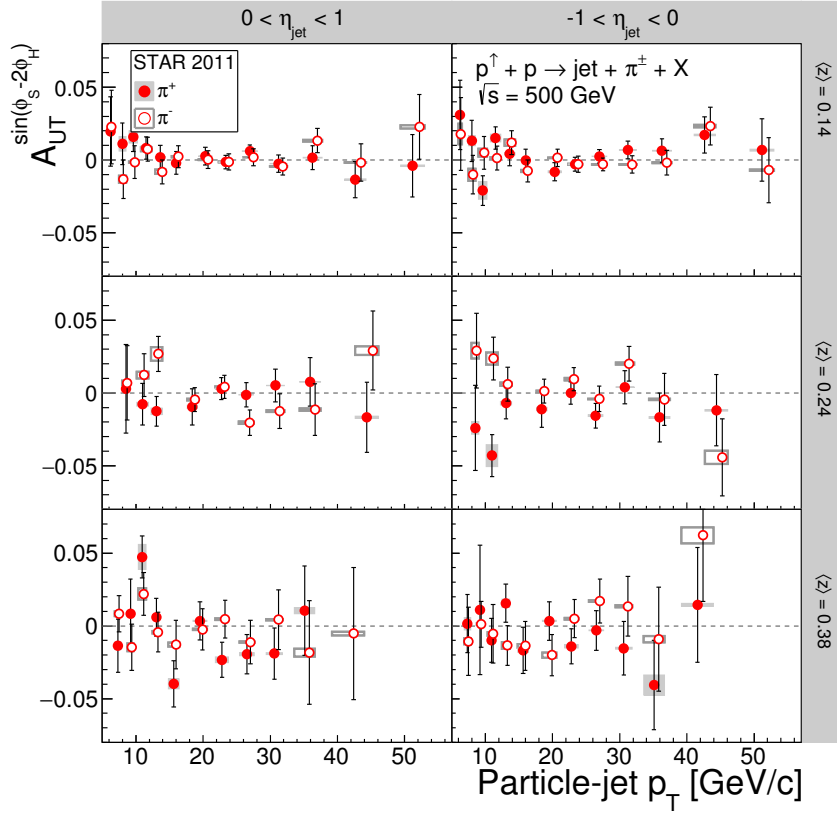


FIG. 40. Final Collins-like asymmetries as a function of particle-jet  $p_T$ . Asymmetries are shown separately for  $\pi^+$  and  $\pi^-$  for two bins of jet  $\eta$  (relative to the polarized beam) and three bins of pion  $z$ . Statistical uncertainties are shown as error bars, while systematic uncertainties are shown as shaded error boxes.

setting the upper limit of the 95% confidence level at 0.0076. It is worth pointing out that these are asymmetries with  $2\sigma$  deviations from zero. So, while by no means conclusive, the data suggest something interesting, making the 2017 data even more compelling.

### 3. Collins Asymmetry

Final results for Collins asymmetries are presented in terms of particle-jet  $p_T$  (Fig. 44), pion  $z$  (Fig. 45), and pion  $j_T$  (Fig. 46). In many ways, the Collins effect is the “inverse” of the Collins-like effect. The Collins asymmetry is expected to arise from quark transversity; thus, the best sensitivity should reside at higher values of jet  $p_T$ . Figure 44 presents the

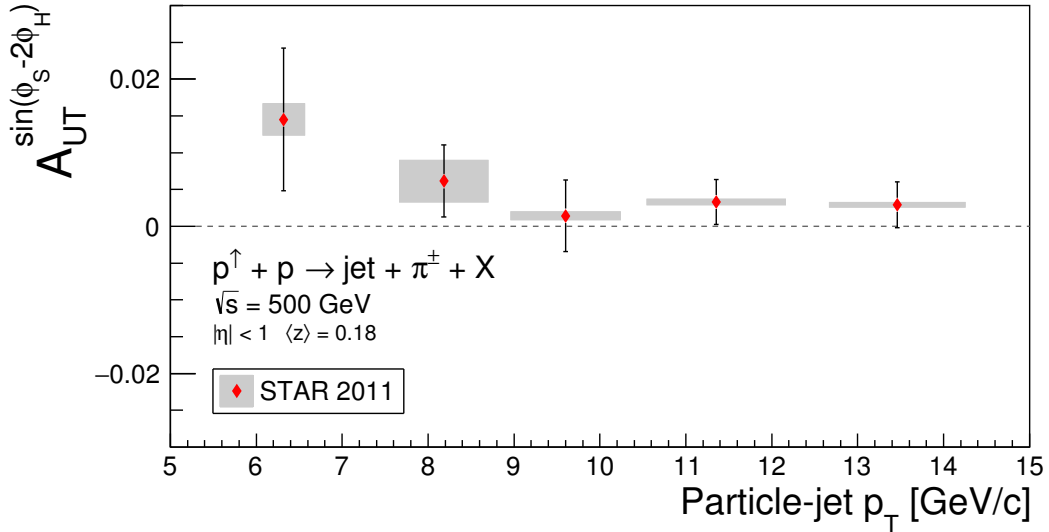


FIG. 41. Final Collins-like asymmetries as a function of particle-jet  $p_T$  for pions reconstructed with  $0.1 < z < 0.3$ . Asymmetries are shown combining  $\pi^+$  and  $\pi^-$  and integrating over the full range of jet pseudorapidity,  $-1 < \eta < 1$ . Statistical uncertainties are shown as error bars, while systematic uncertainties are shown as shaded error boxes.

asymmetry as a function of jet  $p_T$  for different ranges of jet  $\eta$  and pion  $z$ . A clear asymmetry is observed in jets with  $p_T \sim 20 \text{ GeV}/c$  or higher and  $\eta > 0$  relative to the polarized beam. The magnitude of the asymmetry also appears to rise from  $0.1 < z < 0.2$  to  $z > 0.2$ . The observed asymmetries are positive for  $\pi^+$  and negative for  $\pi^-$ . This is consistent with expectation for the Collins asymmetry and marks the first such observation in polarized proton collisions.

Uncertainties of the present data are dominated by statistics with systematics well under control. As with the Collins-like asymmetries, the dominant systematics at low  $p_T$  arise from the parton-jet matching probabilities. At higher values of  $p_T$ , the leading source of systematics arises from “leak-through” and trigger bias, though the systematic uncertainties are typically  $\sim 15\%$  of the statistical uncertainties.

There also appears to be a small effect in the lowest  $z$  bin at high jet  $p_T$  for jet  $\eta < 0$ . This is not consistent with the expectation from the Collins asymmetry, and the effect does not persist into higher bins of  $z$ . Thus, it is not expected that this effect is real. It is most likely an unlucky statistical fluctuation.

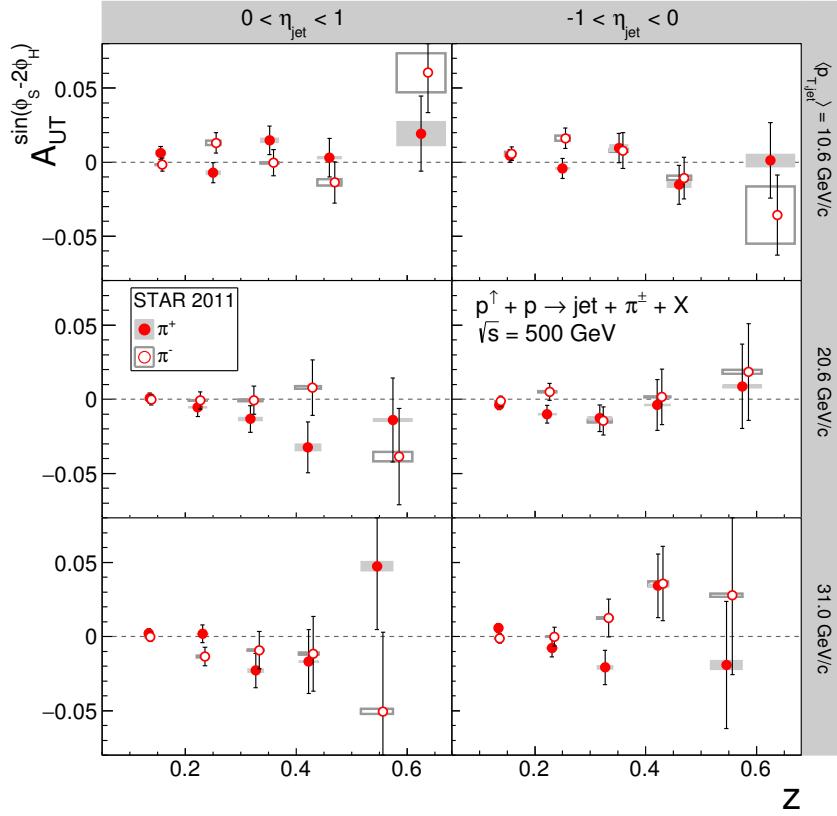


FIG. 42. Final Collins-like asymmetries as a function of pion  $z$ . Asymmetries are shown separately for  $\pi^+$  and  $\pi^-$  for two bins of jet  $\eta$  (relative to the polarized beam) and three bins of jet  $p_T$ . Statistical uncertainties are shown as error bars, while systematic uncertainties are shown as shaded error boxes.

In Fig. 45, the Collins asymmetries are shown as a function of pion  $z$  for three bins of jet  $p_T$  and two bins of jet  $\eta$  calculated relative to the polarized beam. The Collins asymmetry is expected to increase as a function of  $z$ , with near-linear dependence [30]. At high- $p_T$  the present data indicate asymmetries with such a dependence. For jets scattered backward relative to the polarized beam, as well as for jets with lower values of  $p_T$  there do not appear to be large signals present. This is also consistent with expectation.

The Collins effect depends upon non-zero transversity but also the presence of a polarized and transverse-momentum-dependent fragmentation function. Thus, while it is informative to examine the jet- $p_T$  and  $z$  dependences of the Collins effect, it is also important to examine the  $j_T$  dependence of the Collins effect. This study examines the how the asymmetry depends

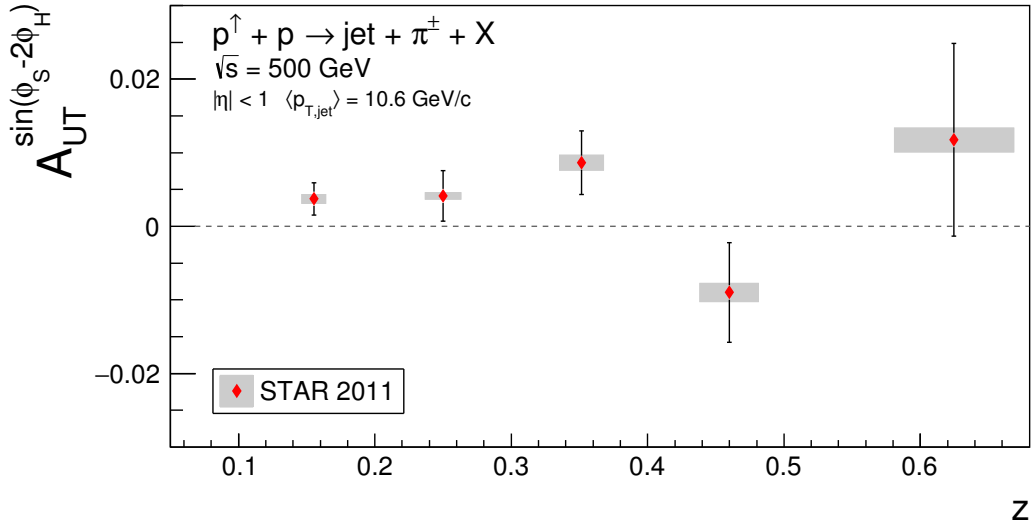


FIG. 43. Final Collins-like asymmetries as a function of pion  $z$  for jets reconstructed with  $6 < p_T < 13.8$  GeV/c. Asymmetries are shown combining  $\pi^+$  and  $\pi^-$  and integrating over the full range of jet pseudorapidity,  $-1 < \eta < 1$ . Statistical uncertainties are shown as error bars, while systematic uncertainties are shown as shaded error boxes.

upon the relative transverse momentum of the pion, i.e. the pion  $p_T$  relative to the jet axis. The final results for the present data are presented in Fig. 46 for jets with  $22.7 < p_T < 55$  GeV/c in three bins of pion  $z$ . The asymmetries appear largest around  $j_T \sim 0.3 - 0.4$  GeV/c. As discussed in Section VIII D, for a given minimum  $\Delta R$  and there is a correlation between  $z$  and  $j_T$ . As the  $\Delta R$  threshold is relaxed, a wider range of  $j_T$  may be spanned within a bin of  $z$ . However, this must be balanced with the degradation in azimuthal resolution as the pion moves closer to the jet axis. One observes that the yield drops quickly toward lower values of  $j_T$  within each of the bins of  $z$ . Thus, without proper tuning of the  $\Delta R$  cut, the most interesting regions of phase space would be lost. Fortunately for the present analysis, enough phase space is open for the most interesting effects to present themselves in a region clear of systematic complications.

Integrating over all bins of  $z$  at high- $p_T$ , the Collins asymmetries show an effect of greater than  $5.5\sigma$  significance. Thus, the present data represent the first observation of the Collins effect in polarized proton collisions. The results should be of particular relevance to a number of on-going efforts. First, as indicated by unpolarized Monte Carlo simulations, the

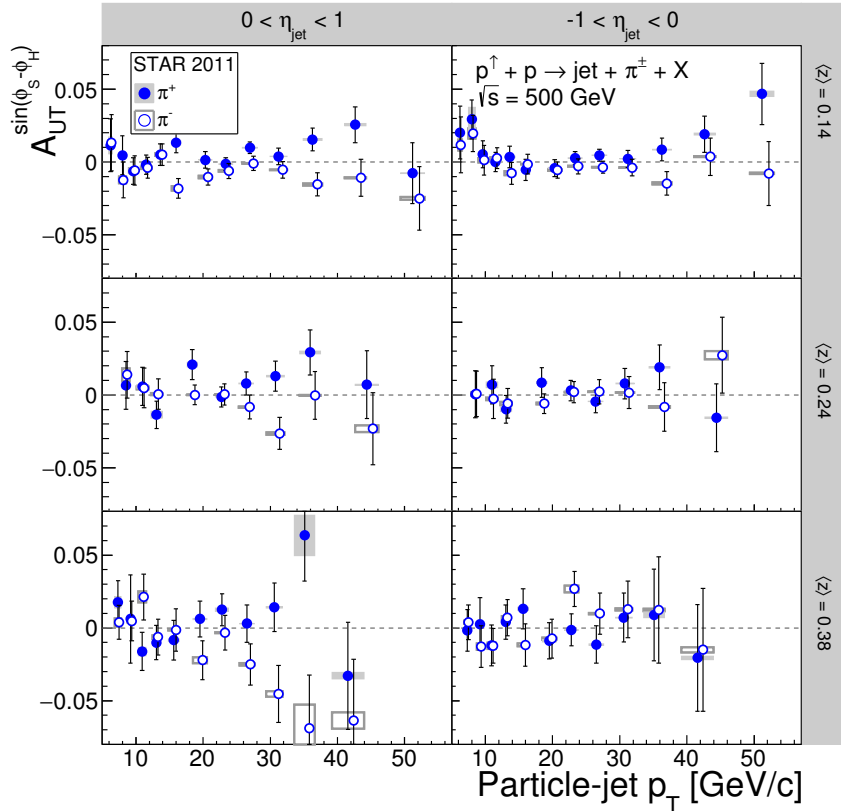


FIG. 44. Final Collins asymmetries as a function of particle-jet  $p_T$ . Asymmetries are shown separately for  $\pi^+$  and  $\pi^-$  for two bins of jet  $\eta$  (relative to the polarized beam) and three bins of pion  $z$ . Statistical uncertainties are shown as error bars, while systematic uncertainties are shown as shaded error boxes.

present data span a range of  $x_Q$  which complements existing SIDIS measurements and current transversity extractions. Second, the present results combined with existing STAR data on dihadrons [31, 32] can address existing theoretical questions concerning universality and the size of possible TMD factorization-breaking effects in polarized proton collisions. Further, the combination of the present results with existing STAR data of Collins asymmetries in polarized proton collisions at  $\sqrt{s} = 200$  GeV [21, 33], may yield insight into questions such as TMD evolution.

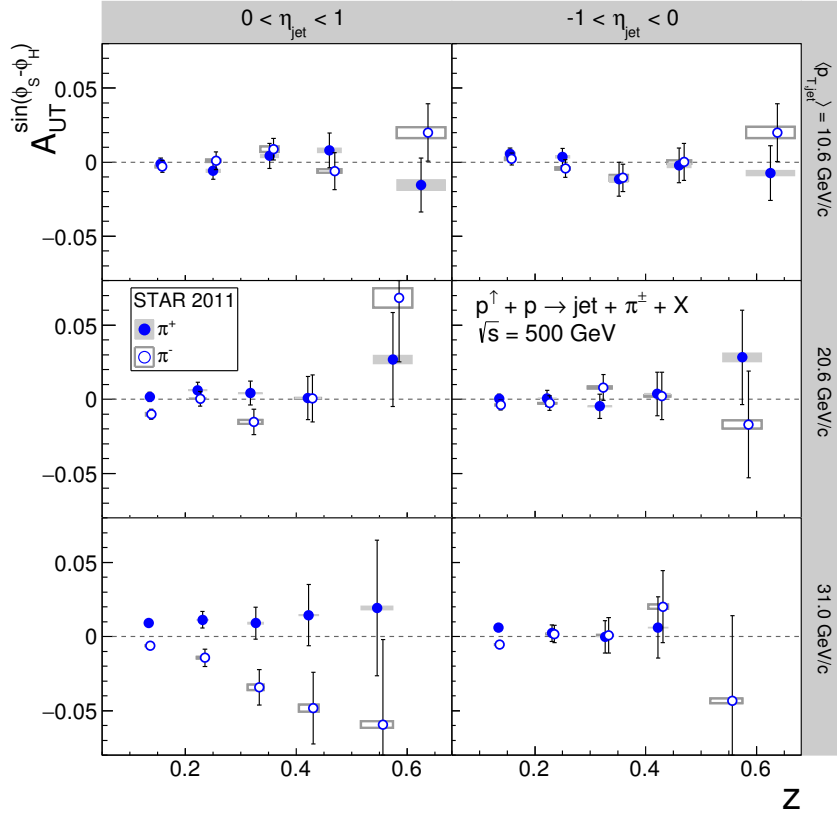


FIG. 45. Final Collins-like asymmetries as a function of pion  $z$ . Asymmetries are shown separately for  $\pi^+$  and  $\pi^-$  for two bins of jet  $\eta$  (relative to the polarized beam) and three bins of jet  $p_T$ . Statistical uncertainties are shown as error bars, while systematic uncertainties are shown as shaded error boxes.

### C. Comparison to Models

Unpolarized Monte Carlo simulations suggest that the present data span a range of quark  $x$  which complements existing SIDIS measurements and current transversity extractions [34, 35] but at much higher values of  $Q^2$ . Accordingly, the present data present an opportunity to address existing theoretical questions concerning universality and the size of possible TMD factorization-breaking effects in polarized-proton collisions, and TMD evolution.

Figure 47 presents the Collins asymmetries for jets reconstructed with  $22.7 < p_T < 55$   $\text{GeV}/c$  and  $0 < \eta < 1$  in comparison with four sets of model calculations. Each set is based upon a global analysis of SIDIS and  $e^+e^-$  data, assumes robust TMD factorization applied to

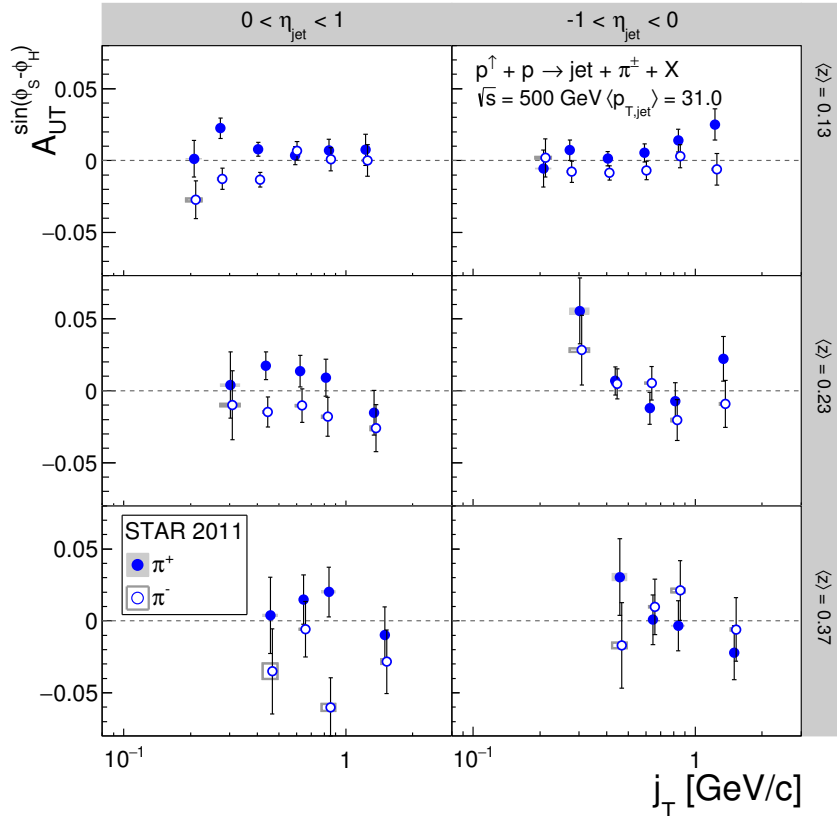


FIG. 46. Final Collins asymmetries as a function of pion  $j_T$  for jets reconstructed with  $22.7 < p_T < 55 \text{ GeV}/c$ . Asymmetries are shown separately for  $\pi^+$  and  $\pi^-$  for two bins of jet  $\eta$  (relative to the polarized beam) and three bins of pion  $z$ . Statistical uncertainties are shown as error bars, while systematic uncertainties are shown as shaded error boxes.

proton-proton interactions, and assumes universality of the Collins fragmentation function. Both of the so-called “SIDIS-1” [34] and “SIDIS-2” [34] predictions are based upon Ref. [9]. The SIDIS-1 curves utilize fragmentation functions from Ref. [36], while the SIDIS-2 curves utilize an updated set of SIDIS results and the fragmentation functions from Ref. [37]. The KRPY and KPRY-NLL predictions are based upon Ref. [35]. The KPRY-NLL curves assume TMD evolution up to next-to-leading-log, while the KPRY curves assume no TMD evolution. In general the models compare favorably with the data, consistent with the expectation of universality of the Collins fragmentation function. In addition, this comparison is also consistent with the assumption of robust TMD factorization for proton-proton inter-

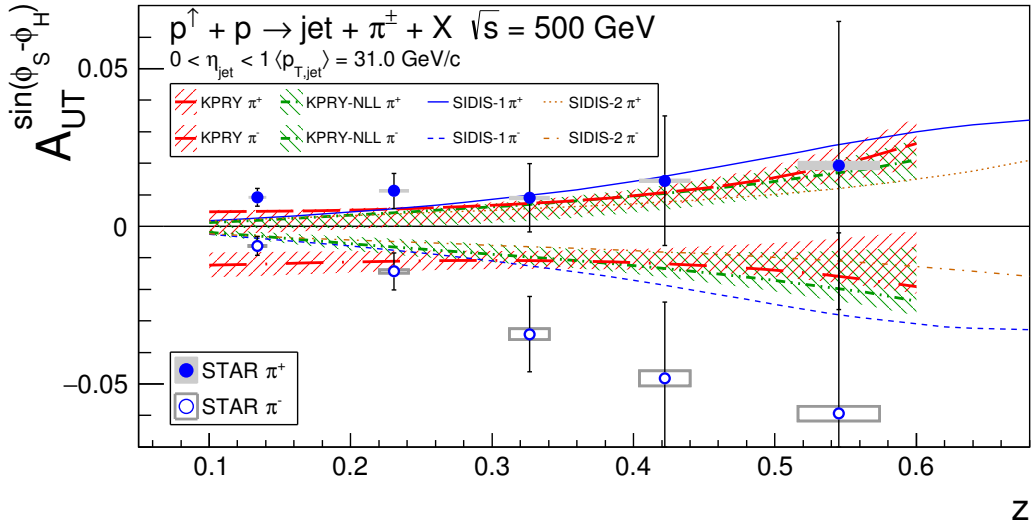


FIG. 47. Collins asymmetries as a function of pion  $z$  for jets reconstructed with  $22.7 < p_T < 55$  GeV/ $c$  and  $0 < \eta < 1$ . The asymmetries are shown in comparison with model calculations from Refs. [9, 34, 35]. The calculations are based upon SIDIS and  $e^+e^-$  results and assume robust factorization and universality of the Collins function. The SIDIS-1 [34], SIDIS-2 [34], and KPRY [35] predictions assume no TMD evolution, while the KPRY-NLL [35] curves assume TMD evolution up to next-to-leading-log. The general agreement between the data and the model calculations is consistent with assumptions of robust TMD-factorization and universality of the Collins function.

actions. While it is generally expected that TMD factorization is broken for proton-proton interactions, it has been argued that such factorization holds for observation of a hadron fragment within a jet [38]. Within theoretical uncertainties, the data agree relatively well with either assumption of TMD evolution from the KPRY predictions. However, the data do show a slight preference, for the model without TMD evolution. To quantify this, a simple  $\chi^2$  test is used. The data are compared to the model calculations using the data statistical uncertainties plus the data point-to-point systematics (parton-jet matching, azimuthal resolution, leak-through, and contamination). The test returns  $\chi^2 = 14.2$  for 10 degrees of freedom without evolution compared with  $\chi^2 = 17.7$  with evolution. Including the correlated scale systematics in quadrature with the point-to-point systematics yields  $\chi^2 = 14.0$  for 10 degrees of freedom without evolution compared with  $\chi^2 = 17.6$  with evolution.

**Appendix A: Run List**

12043044 12043045 12043046 12043047 12043048 12043049 12043051 12043053 12043055  
12043060 12043065 12043066 12043067 12043068 12043069 12043077 12043078 12043079  
12043081 12044023 12044024 12044025 12044026 12044029 12044030 12044031 12044038  
12044039 12044040 12044041 12044042 12044043 12044050 12044051 12044052 12044053  
12044054 12044055 12044099 12044100 12044101 12044102 12044103 12045001 12045002  
12045004 12045005 12045006 12045011 12045013 12045016 12046035 12046036 12046037  
12046038 12046039 12046040 12046041 12046042 12046043 12046046 12046068 12046069  
12046070 12046075 12046095 12046097 12046098 12046099 12046100 12046101 12046104  
12046105 12046106 12046107 12047009 12047016 12047017 12047018 12047019 12047020  
12047021 12049037 12049038 12049042 12049043 12049044 12050022 12050023 12050024  
12050034 12050035 12050037 12050038 12050039 12050040 12050041 12050042 12050044  
12050045 12050046 12050047 12050048 12051006 12051007 12051008 12051009 12051010  
12051011 12051012 12051013 12051014 12051020 12051021 12051022 12051023 12051024  
12051025 12051026 12051027 12051028 12051029 12051030 12051031 12051032 12051033  
12051034 12051035 12051036 12051037 12051038 12051052 12051053 12051054 12051055  
12051056 12051057 12051059 12051062 12052011 12052012 12052013 12052014 12052018  
12052019 12052020 12052021 12052022 12052023 12052024 12052026 12052027 12052028  
12052029 12052030 12052031 12052032 12052033 12052034 12052047 12052048 12052049  
12052050 12052051 12052054 12053031 12053036 12053039 12053040 12053041 12053042  
12053043 12053044 12053048 12053049 12053050 12053052 12053070 12054013 12054014  
12054015 12054016 12054017 12054018 12054019 12054020 12054021 12054022 12054024  
12054025 12054026 12054027 12054028 12054029 12054030 12055031 12055034 12055035  
12056007 12056008 12056009 12056010 12056011 12056012 12056013 12056014 12056015  
12056016 12056017 12056018 12056019 12056020 12057008 12057009 12057010 12057011  
12057012 12057013 12057014 12057016 12057017 12057018 12057019 12057020 12057022  
12057050 12057051 12057052 12057053 12057054 12057055 12057057 12057058 12057059  
12057060 12058001 12058003 12058004 12058005 12058011 12058012 12058013 12058014  
12058015 12058016 12058017 12058018 12058019 12058021 12058022 12058024 12058040  
12058048 12058049 12058050 12058052 12058054 12058055 12058057 12058058 12059009

12059011 12059017 12059018 12059019 12059020 12059021 12059024 12059027 12059028  
12059029 12059030 12059031 12059035 12059036 12059037 12059038 12059039 12059070  
12059071 12059077 12059078 12059079 12059080 12059082 12059083 12059084 12060001  
12060004 12060005 12060006 12060007 12060009 12060010 12060011 12060030 12060033  
12060034 12060035 12060036 12060037 12060038 12060039 12060040 12060041 12060042  
12060043 12060044 12060045 12060046 12060047 12060048 12060049 12060051 12060056  
12060058 12060138 12060143 12060144 12060145 12060146 12061006 12061008 12061010  
12061011 12061013 12061014 12061015 12061016 12061018 12062011 12062012 12062013  
12062014 12062015 12062016 12062018 12062019 12062021 12062022 12064005 12064007  
12064008 12064010 12064011 12064012 12064013 12064014 12064015 12064016 12064026  
12064027 12064028 12064029 12064033 12064034 12064035 12064036 12064040 12064042  
12064043 12064044 12064045 12075019 12075021 12075022 12075024 12075029 12075030  
12075031 12075032 12075033 12075034 12075039 12075040 12075041 12075042 12075043  
12076002 12076007 12076008 12076009 12076028 12079005 12079026 12079027 12079028  
12079030 12079031 12079038 12079039 12079040 12080058 12080059 12080062 12080064  
12080066 12080067 12080068 12080069 12080070 12081011 12081014 12081015 12081016  
12081020 12081021 12081022 12081023 12081024 12081025 12081027 12081055 12081056  
12081057 12081069 12081070 12082001 12082002 12082003 12082004 12082005 12082007  
12082022 12082023 12082024 12083020 12083021 12083022 12083023 12083024 12083045  
12083046 12083047 12083051 12083054 12083055 12083056 12083057 12083058 12083059  
12083060 12083061 12084004 12084009 12084010 12084011 12084012 12084013 12084014  
12084015 12084016 12084017 12084018 12084019 12084020 12084021 12085023 12085024  
12085025 12085026 12085027 12085028 12085029 12085030 12085031 12086001 12086002  
12086004 12086005 12086006 12086007 12086017 12086019 12086020 12086033 12086034  
12086035 12086037 12086038 12086039 12086040 12086041 12086042 12086046 12086047  
12087002 12087003 12087004 12087005 12087012 12087023 12087025 12087026 12087027  
12087032 12087033 12087080 12087084 12087085 12087095 12087096 12087097 12087098  
12087099 12087100 12088075 12088076 12088077 12088078 12088079 12088080 12088081  
12088086 12088087 12088088 12089006 12089008 12089009 12089010 12089085 12089086  
12089087 12089088 12090002 12090003 12090009 12090010 12090011 12090017 12090019  
12090020 12090021 12090042 12090043 12090045 12090046 12090047 12090048 12090049

12090050 12090051 12090052 12090053 12090054 12090055 12090060 12091004 12091005  
 12091006 12091007 12091009 12091010 12091011 12091012 12091013 12091014 12091016  
 12091017 12091018 12091019 12091021 12091022 12091023 12091041 12091042 12091043  
 12091044 12091045 12091048 12092020 12092021 12092047 12093001 12093002 12093003  
 12093004 12093005 12093006 12093007 12093008 12093009 12093010 12093014 12093023  
 12093024 12093025 12093030 12093032 12093033 12093034 12093036 12093037 12093039  
 12093040 12093041 12093042 12093044 12093049 12093050 12093051 12094009 12094010  
 12094011 12094012 12094013 12094014 12094015 12094016 12094017 12094018 12094019  
 12094020 12094021 12094022 12094024 12094025 12094026 12094060 12094061 12094062  
 12094063 12094064 12094065 12095005 12095038 12095039 12095041 12095042 12095043  
 12095044 12095045 12095046 12095055 12095056 12095057 12095058 12095059 12095060  
 12095061 12095063 12096005 12096006 12096014 12096015 12096016 12096017 12096018  
 12096019 12096020 12096021 12096023 12096024 12096025 12096026 12096027 12096028  
 12096029 12096030 12096031 12096032 12096033 12096034 12096047 12096048 12096049  
 12096056 12096057 12096058 12096059 12096060 12096061 12096062 12097002 12097003  
 12097004 12097007 12097008 12097009 12097010 12097011 12097012 12097013 12097016  
 12097017 12097018 12097019 12097020 12097021 12097022 12098009 12098010 12098012  
 12098013 12098014 12098017 12098018 12098019 12098020 12098021 12098022 12098031

## Appendix B: Resolution Corrections

<b><math>z</math> Range</b>	<b>VPDMB</b>	<b>JP0</b>	<b>JP1</b>
0.1 – 0.2	$0.695(5.84 \times 10^{-2})$	$0.810(5.80 \times 10^{-3})$	$0.859(2.01 \times 10^{-2})$
0.2 – 0.3	$0.662(2.06 \times 10^{-2})$	$0.699(4.96 \times 10^{-2})$	$0.865(1.07 \times 10^{-2})$
0.3 – 0.4	$0.687(2.96 \times 10^{-2})$	$0.863(2.42 \times 10^{-2})$	$0.747(5.77 \times 10^{-2})$
0.4 – 0.5	$0.726(6.05 \times 10^{-2})$	$0.805(1.75 \times 10^{-2})$	$0.763(9.48 \times 10^{-2})$
0.5 – 0.8	$0.678(1.48 \times 10^{-2})$	$0.414(7.66 \times 10^{-1})$	$0.625(2.88 \times 10^{-1})$

TABLE XX. Corrections (and relative systematic uncertainties) for dilutions to the low- $p_T$  Collins-like asymmetry from finite azimuthal angular resolution.

$z$ Range	VPDMB	JP0	JP1	JP2
0.1 – 0.2	0.816( $1.74 \times 10^{-2}$ )	0.865( $4.65 \times 10^{-3}$ )	0.869( $1.75 \times 10^{-2}$ )	0.888( $4.57 \times 10^{-2}$ )
0.2 – 0.3	0.818( $3.40 \times 10^{-3}$ )	0.824( $1.13 \times 10^{-2}$ )	0.798( $1.20 \times 10^{-2}$ )	0.792( $2.83 \times 10^{-2}$ )
0.3 – 0.4	0.743( $2.54 \times 10^{-2}$ )	0.828( $1.94 \times 10^{-2}$ )	0.798( $3.61 \times 10^{-2}$ )	0.904( $1.03 \times 10^{-1}$ )
0.4 – 0.5	0.870( $3.45 \times 10^{-2}$ )	0.870( $1.38 \times 10^{-2}$ )	0.771( $1.37 \times 10^{-2}$ )	0.785( $4.96 \times 10^{-2}$ )
0.5 – 0.8	0.711( $5.99 \times 10^{-2}$ )	0.570( $4.02 \times 10^{-2}$ )	0.613( $5.04 \times 10^{-2}$ )	0.843( $5.78 \times 10^{-2}$ )

TABLE XXI. Corrections (and relative systematic uncertainties) for dilutions to the mid- $p_T$  Collins-like asymmetry from finite azimuthal angular resolution.

$z$ Range	JP0	JP1	JP2
0.1 – 0.2	0.913( $3.37 \times 10^{-2}$ )	0.913( $3.68 \times 10^{-2}$ )	0.915( $3.17 \times 10^{-2}$ )
0.2 – 0.3	0.908( $2.95 \times 10^{-2}$ )	0.895( $1.09 \times 10^{-2}$ )	0.912( $2.68 \times 10^{-2}$ )
0.3 – 0.4	0.856( $2.76 \times 10^{-2}$ )	0.867( $1.77 \times 10^{-2}$ )	0.883( $2.16 \times 10^{-2}$ )
0.4 – 0.5	0.874( $2.94 \times 10^{-2}$ )	0.870( $2.76 \times 10^{-2}$ )	0.933( $1.47 \times 10^{-2}$ )
0.5 – 0.8	0.856( $6.13 \times 10^{-2}$ )	0.865( $1.02 \times 10^{-1}$ )	0.781( $4.77 \times 10^{-2}$ )

TABLE XXII. Corrections (and relative systematic uncertainties) for dilutions to the high- $p_T$  Collins-like asymmetry from finite azimuthal angular resolution.

$p_T$ Range [GeV/ $c$ ]	VPDMB	JP0	JP1	JP2
6.0 – 7.1	$0.635(9.88 \times 10^{-2})$			
7.1 – 8.4	$0.769(2.60 \times 10^{-2})$	$0.795(4.40 \times 10^{-2})$		
8.4 – 9.9	$0.744(5.95 \times 10^{-3})$	$0.809(4.40 \times 10^{-3})$		
9.9 – 11.7	$0.818(4.41 \times 10^{-3})$	$0.789(2.85 \times 10^{-2})$	$0.838(2.94 \times 10^{-2})$	
11.7 – 13.8	$0.856(9.71 \times 10^{-3})$	$0.860(1.80 \times 10^{-2})$	$0.883(5.00 \times 10^{-2})$	
13.8 – 16.3	$0.816(1.75 \times 10^{-2})$	$0.842(1.83 \times 10^{-2})$	$0.858(2.45 \times 10^{-2})$	
16.3 – 19.2		$0.888(1.75 \times 10^{-2})$	$0.868(8.99 \times 10^{-3})$	$0.875(8.59 \times 10^{-3})$
19.2 – 22.7		$0.896(1.09 \times 10^{-2})$	$0.892(1.48 \times 10^{-2})$	$0.898(3.43 \times 10^{-2})$
22.7 – 26.8		$0.906(7.75 \times 10^{-3})$	$0.908(8.90 \times 10^{-3})$	$0.900(1.03 \times 10^{-2})$
26.8 – 31.6		$0.925(8.39 \times 10^{-3})$	$0.924(9.59 \times 10^{-3})$	$0.944(1.11 \times 10^{-2})$
31.6 – 37.3		$0.917(1.08 \times 10^{-2})$	$0.914(1.07 \times 10^{-2})$	$0.897(1.36 \times 10^{-2})$
37.3 – 45.0		$0.907(8.54 \times 10^{-3})$	$0.902(7.74 \times 10^{-3})$	$0.910(8.81 \times 10^{-3})$
45.0 – 55.0		$0.965(2.91 \times 10^{-2})$	$0.967(2.08 \times 10^{-2})$	$0.964(2.16 \times 10^{-2})$

TABLE XXIII. Corrections (and relative systematic uncertainties) for dilutions to the low- $z$  Collins-like asymmetry from finite azimuthal angular resolution.

$p_T$	Range [GeV/ $c$ ]	VPDMB	JP0	JP1	JP2
6.0 – 7.1		0.638( $2.97 \times 10^{-2}$ )			
7.1 – 8.4		0.658( $1.76 \times 10^{-1}$ )	0.556( $5.06 \times 10^{-2}$ )		
8.4 – 9.9		0.677( $3.01 \times 10^{-2}$ )	0.568( $5.23 \times 10^{-2}$ )		
9.9 – 11.7		0.780( $3.74 \times 10^{-2}$ )	0.865( $6.33 \times 10^{-2}$ )	0.809( $5.53 \times 10^{-2}$ )	
11.7 – 13.8		0.862( $9.80 \times 10^{-3}$ )	0.851( $1.89 \times 10^{-2}$ )	0.891( $2.13 \times 10^{-2}$ )	
13.8 – 16.3		0.818( $3.38 \times 10^{-3}$ )	0.797( $6.39 \times 10^{-3}$ )	0.757( $2.55 \times 10^{-2}$ )	
16.3 – 19.2		0.839( $2.36 \times 10^{-2}$ )	0.808( $2.09 \times 10^{-2}$ )	0.708( $9.19 \times 10^{-2}$ )	
19.2 – 22.7		0.880( $7.10 \times 10^{-3}$ )	0.876( $1.49 \times 10^{-2}$ )	0.891( $1.30 \times 10^{-2}$ )	
22.7 – 26.8		0.912( $1.63 \times 10^{-2}$ )	0.895( $6.59 \times 10^{-3}$ )	0.928( $2.64 \times 10^{-2}$ )	
26.8 – 31.6		0.895( $1.91 \times 10^{-2}$ )	0.884( $2.31 \times 10^{-2}$ )	0.895( $1.95 \times 10^{-2}$ )	
31.6 – 37.3		0.901( $1.73 \times 10^{-2}$ )	0.896( $1.77 \times 10^{-2}$ )	0.886( $1.78 \times 10^{-2}$ )	
37.3 – 45.0		0.931( $1.16 \times 10^{-2}$ )	0.930( $2.03 \times 10^{-2}$ )	0.925( $1.87 \times 10^{-2}$ )	
45.0 – 55.0		0.955( $2.71 \times 10^{-2}$ )	0.958( $2.14 \times 10^{-2}$ )	0.952( $1.98 \times 10^{-2}$ )	

TABLE XXIV. Corrections (and relative systematic uncertainties) for dilutions to the mid- $z$  Collins-like asymmetry from finite azimuthal angular resolution.

$p_T$ Range [GeV/ $c$ ]	VPDMB	JP0	JP1	JP2
6.0 – 7.1	$0.6666(4.14 \times 10^{-2})$			
7.1 – 8.4	$0.694(5.06 \times 10^{-2})$	$0.906(2.57 \times 10^{-2})$		
8.4 – 9.9	$0.794(5.00 \times 10^{-2})$	$0.716(4.17 \times 10^{-2})$		
9.9 – 11.7	$0.755(5.95 \times 10^{-2})$	$0.770(2.72 \times 10^{-2})$	$0.573(1.98 \times 10^{-1})$	
11.7 – 13.8	$0.768(1.37 \times 10^{-2})$	$0.835(3.33 \times 10^{-2})$	$0.881(4.53 \times 10^{-2})$	
13.8 – 16.3	$0.779(1.52 \times 10^{-2})$	$0.780(6.18 \times 10^{-3})$	$0.804(3.22 \times 10^{-2})$	
16.3 – 19.2		$0.821(3.04 \times 10^{-2})$	$0.690(2.44 \times 10^{-2})$	$0.832(1.35 \times 10^{-2})$
19.2 – 22.7		$0.857(1.75 \times 10^{-2})$	$0.819(1.26 \times 10^{-2})$	$0.889(6.09 \times 10^{-3})$
22.7 – 26.8		$0.866(4.73 \times 10^{-2})$	$0.882(4.51 \times 10^{-2})$	$0.898(7.82 \times 10^{-3})$
26.8 – 31.6		$0.833(1.69 \times 10^{-2})$	$0.832(3.11 \times 10^{-2})$	$0.905(2.34 \times 10^{-2})$
31.6 – 37.3		$0.865(5.34 \times 10^{-2})$	$0.846(6.64 \times 10^{-2})$	$0.779(1.36 \times 10^{-1})$
37.3 – 45.0		$0.905(1.82 \times 10^{-2})$	$0.903(1.53 \times 10^{-2})$	$0.902(1.44 \times 10^{-2})$
45.0 – 55.0		$0.946(8.02 \times 10^{-3})$	$0.945(8.07 \times 10^{-3})$	$0.952(1.44 \times 10^{-2})$

TABLE XXV. Corrections (and relative systematic uncertainties) for dilutions to the high- $z$  Collins-like asymmetry from finite azimuthal angular resolution.

$p_T$	Range [GeV/ $c$ ]	VPDMB	JP0	JP1	JP2
6.0 – 7.1		0.636(5.51 × 10 <sup>-2</sup> )			
7.1 – 8.4		0.729(7.36 × 10 <sup>-2</sup> )	0.738(3.53 × 10 <sup>-2</sup> )		
8.4 – 9.9		0.722(1.25 × 10 <sup>-2</sup> )	0.739(2.39 × 10 <sup>-2</sup> )		
9.9 – 11.7		0.806(1.04 × 10 <sup>-2</sup> )	0.812(2.37 × 10 <sup>-3</sup> )	0.833(3.21 × 10 <sup>-2</sup> )	
11.7 – 13.8		0.858(9.31 × 10 <sup>-3</sup> )	0.857(1.20 × 10 <sup>-2</sup> )	0.886(9.71 × 10 <sup>-3</sup> )	
13.8 – 16.3		0.816(1.21 × 10 <sup>-2</sup> )	0.832(1.37 × 10 <sup>-2</sup> )	0.832(2.46 × 10 <sup>-2</sup> )	
16.3 – 19.2		0.877(1.80 × 10 <sup>-2</sup> )	0.853(1.12 × 10 <sup>-2</sup> )	0.832(4.99 × 10 <sup>-2</sup> )	
19.2 – 22.7		0.892(1.02 × 10 <sup>-2</sup> )	0.889(1.08 × 10 <sup>-2</sup> )	0.896(2.56 × 10 <sup>-2</sup> )	
22.7 – 26.8		0.908(7.67 × 10 <sup>-3</sup> )	0.905(9.05 × 10 <sup>-3</sup> )	0.906(1.12 × 10 <sup>-2</sup> )	
26.8 – 31.6		0.918(8.77 × 10 <sup>-3</sup> )	0.914(9.67 × 10 <sup>-3</sup> )	0.934(1.10 × 10 <sup>-2</sup> )	
31.6 – 37.3		0.914(1.22 × 10 <sup>-2</sup> )	0.910(1.20 × 10 <sup>-2</sup> )	0.895(1.34 × 10 <sup>-2</sup> )	
37.3 – 45.0		0.913(8.34 × 10 <sup>-3</sup> )	0.909(8.73 × 10 <sup>-3</sup> )	0.913(1.10 × 10 <sup>-2</sup> )	
45.0 – 55.0		0.963(1.75 × 10 <sup>-2</sup> )	0.965(2.09 × 10 <sup>-2</sup> )	0.962(2.11 × 10 <sup>-2</sup> )	

TABLE XXVI. Corrections (and relative systematic uncertainties) for dilutions to the low+mid- $z$  Collins-like asymmetry from finite azimuthal angular resolution.

$p_T$ Range [GeV/ $c$ ]	VPDMB	JP0	JP1	JP2
6.0 – 7.1	0.954( $4.16 \times 10^{-3}$ )			
7.1 – 8.4	0.971( $5.30 \times 10^{-3}$ )	0.964( $6.74 \times 10^{-3}$ )		
8.4 – 9.9	0.966( $2.49 \times 10^{-3}$ )	0.977( $1.05 \times 10^{-3}$ )		
9.9 – 11.7	0.963( $1.69 \times 10^{-3}$ )	0.971( $3.23 \times 10^{-3}$ )	0.971( $4.28 \times 10^{-3}$ )	
11.7 – 13.8	0.980( $1.93 \times 10^{-3}$ )	0.981( $2.98 \times 10^{-4}$ )	0.969( $4.30 \times 10^{-4}$ )	
13.8 – 16.3	0.974( $2.66 \times 10^{-4}$ )	0.979( $5.30 \times 10^{-2}$ )	0.983( $9.49 \times 10^{-4}$ )	
16.3 – 19.2		0.986( $6.80 \times 10^{-4}$ )	0.982( $3.38 \times 10^{-3}$ )	0.996( $1.00 \times 10^{-4}$ )
19.2 – 22.7		0.984( $1.35 \times 10^{-3}$ )	0.981( $9.25 \times 10^{-4}$ )	0.991( $5.54 \times 10^{-4}$ )
22.7 – 26.8		0.988( $5.30 \times 10^{-3}$ )	0.986( $3.97 \times 10^{-2}$ )	0.993( $1.35 \times 10^{-3}$ )
26.8 – 31.6		0.988( $6.35 \times 10^{-2}$ )	0.984( $2.10 \times 10^{-3}$ )	0.994( $6.03 \times 10^{-4}$ )
31.6 – 37.3		0.987( $2.04 \times 10^{-3}$ )	0.986( $2.80 \times 10^{-2}$ )	0.982( $3.29 \times 10^{-3}$ )
37.3 – 45.0		0.985( $2.98 \times 10^{-4}$ )	0.985( $1.29 \times 10^{-4}$ )	0.991( $4.28 \times 10^{-3}$ )
45.0 – 55.0		0.994( $2.97 \times 10^{-2}$ )	0.994( $1.32 \times 10^{-3}$ )	0.994( $1.97 \times 10^{-3}$ )

TABLE XXVII. Corrections (and relative systematic uncertainties) for dilutions to the inclusive jet asymmetry from finite azimuthal angular resolution.

$z$ Range	VPDMB	JP0	JP1
0.1 – 0.2	$0.852(1.50 \times 10^{-2})$	$0.895(6.23 \times 10^{-3})$	$0.949(3.52 \times 10^{-2})$
0.2 – 0.3	$0.830(1.27 \times 10^{-2})$	$0.833(2.31 \times 10^{-2})$	$0.942(7.07 \times 10^{-3})$
0.3 – 0.4	$0.854(1.02 \times 10^{-2})$	$0.936(1.11 \times 10^{-2})$	$0.897(5.70 \times 10^{-2})$
0.4 – 0.5	$0.752(3.73 \times 10^{-2})$	$0.903(7.03 \times 10^{-3})$	$0.928(1.31 \times 10^{-3})$
0.5 – 0.8	$0.784(3.90 \times 10^{-2})$	$0.742(5.23 \times 10^{-2})$	$0.679(3.61 \times 10^{-1})$

TABLE XXVIII. Corrections (and relative systematic uncertainties) for dilutions to the low- $p_T$  Collins asymmetry from finite azimuthal angular resolution.

$z$ Range	VPDMB	JP0	JP1	JP2
0.1 – 0.2	$0.911(4.56 \times 10^{-3})$	$0.939(5.30 \times 10^{-2})$	$0.943(3.60 \times 10^{-2})$	$0.951(3.72 \times 10^{-2})$
0.2 – 0.3	$0.933(5.40 \times 10^{-3})$	$0.929(7.71 \times 10^{-3})$	$0.929(8.78 \times 10^{-3})$	$0.935(1.90 \times 10^{-2})$
0.3 – 0.4	$0.878(1.98 \times 10^{-2})$	$0.925(7.63 \times 10^{-3})$	$0.923(8.30 \times 10^{-3})$	$0.963(6.71 \times 10^{-3})$
0.4 – 0.5	$0.955(9.69 \times 10^{-3})$	$0.952(9.92 \times 10^{-3})$	$0.910(1.62 \times 10^{-2})$	$0.941(2.71 \times 10^{-2})$
0.5 – 0.8	$0.887(4.43 \times 10^{-2})$	$0.810(1.13 \times 10^{-1})$	$0.793(5.18 \times 10^{-2})$	$0.414(1.71 \times 10^{-1})$

TABLE XXIX. Corrections (and relative systematic uncertainties) for dilutions to the mid- $p_T$  Collins asymmetry from finite azimuthal angular resolution.

$z$ Range	JP0	JP1	JP2
0.1 – 0.2	$0.960(7.89 \times 10^{-3})$	$0.958(8.02 \times 10^{-3})$	$0.959(2.22 \times 10^{-2})$
0.2 – 0.3	$0.967(1.00 \times 10^{-2})$	$0.962(8.77 \times 10^{-3})$	$0.973(7.78 \times 10^{-3})$
0.3 – 0.4	$0.941(3.14 \times 10^{-2})$	$0.944(8.02 \times 10^{-3})$	$0.936(4.08 \times 10^{-2})$
0.4 – 0.5	$0.934(2.49 \times 10^{-2})$	$0.920(6.01 \times 10^{-2})$	$0.970(2.30 \times 10^{-2})$
0.5 – 0.8	$0.924(5.85 \times 10^{-2})$	$0.906(9.31 \times 10^{-2})$	$0.728(3.84 \times 10^{-2})$

TABLE XXX. Corrections (and relative systematic uncertainties) for dilutions to the high- $p_T$  Collins asymmetry from finite azimuthal angular resolution.

$p_T$ Range [GeV/ $c$ ]	VPDMB	JP0	JP1	JP2
6.0 – 7.1	0.833(1.53 $\times 10^{-2}$ )			
7.1 – 8.4	0.869(3.94 $\times 10^{-2}$ )	0.846(5.66 $\times 10^{-3}$ )		
8.4 – 9.9	0.866(9.28 $\times 10^{-3}$ )	0.897(1.24 $\times 10^{-2}$ )		
9.9 – 11.7	0.901(4.44 $\times 10^{-2}$ )	0.913(2.63 $\times 10^{-2}$ )	0.941(2.89 $\times 10^{-2}$ )	
11.7 – 13.8	0.934(8.68 $\times 10^{-3}$ )	0.943(6.58 $\times 10^{-3}$ )	0.959(1.55 $\times 10^{-2}$ )	
13.8 – 16.3	0.911(8.40 $\times 10^{-3}$ )	0.928(1.56 $\times 10^{-2}$ )	0.939(1.09 $\times 10^{-2}$ )	
16.3 – 19.2		0.951(1.12 $\times 10^{-2}$ )	0.939(8.77 $\times 10^{-3}$ )	0.941(9.05 $\times 10^{-3}$ )
19.2 – 22.7		0.953(1.12 $\times 10^{-2}$ )	0.957(1.38 $\times 10^{-2}$ )	0.959(2.50 $\times 10^{-2}$ )
22.7 – 26.8		0.958(6.81 $\times 10^{-3}$ )	0.959(6.76 $\times 10^{-3}$ )	0.956(7.21 $\times 10^{-3}$ )
26.8 – 31.6		0.969(2.06 $\times 10^{-2}$ )	0.962(9.00 $\times 10^{-3}$ )	0.981(1.62 $\times 10^{-2}$ )
31.6 – 37.3		0.957(1.80 $\times 10^{-2}$ )	0.955(1.88 $\times 10^{-2}$ )	0.941(2.51 $\times 10^{-2}$ )
37.3 – 45.0		0.931(8.35 $\times 10^{-3}$ )	0.927(8.64 $\times 10^{-3}$ )	0.918(8.07 $\times 10^{-3}$ )
45.0 – 55.0		0.987(9.40 $\times 10^{-3}$ )	0.988(8.33 $\times 10^{-3}$ )	0.986(8.69 $\times 10^{-3}$ )

TABLE XXXI. Corrections (and relative systematic uncertainties) for dilutions to the low- $z$  Collins asymmetry from finite azimuthal angular resolution.

$p_T$ Range [GeV/ $c$ ]	VPDMB	JP0	JP1	JP2
6.0 – 7.1	0.828(1.23 $\times 10^{-2}$ )			
7.1 – 8.4	0.814(4.80 $\times 10^{-2}$ )	0.664(1.68 $\times 10^{-2}$ )		
8.4 – 9.9	0.811(3.05 $\times 10^{-2}$ )	0.806(2.49 $\times 10^{-2}$ )		
9.9 – 11.7	0.919(8.90 $\times 10^{-3}$ )	0.931(4.08 $\times 10^{-2}$ )	0.901(2.71 $\times 10^{-2}$ )	
11.7 – 13.8	0.942(6.31 $\times 10^{-3}$ )	0.936(1.21 $\times 10^{-2}$ )	0.961(3.29 $\times 10^{-2}$ )	
13.8 – 16.3	0.933(5.40 $\times 10^{-3}$ )	0.920(9.59 $\times 10^{-3}$ )	0.918(1.01 $\times 10^{-2}$ )	
16.3 – 19.2		0.938(1.26 $\times 10^{-2}$ )	0.929(1.01 $\times 10^{-2}$ )	0.909(2.94 $\times 10^{-2}$ )
19.2 – 22.7		0.941(9.03 $\times 10^{-3}$ )	0.954(8.14 $\times 10^{-3}$ )	0.965(5.39 $\times 10^{-3}$ )
22.7 – 26.8		0.967(1.12 $\times 10^{-2}$ )	0.959(1.18 $\times 10^{-2}$ )	0.980(1.00 $\times 10^{-2}$ )
26.8 – 31.6		0.965(1.07 $\times 10^{-2}$ )	0.960(1.13 $\times 10^{-2}$ )	0.968(4.13 $\times 10^{-3}$ )
31.6 – 37.3		0.969(2.33 $\times 10^{-2}$ )	0.967(1.12 $\times 10^{-2}$ )	0.961(1.50 $\times 10^{-2}$ )
37.3 – 45.0		0.979(4.20 $\times 10^{-3}$ )	0.980(3.30 $\times 10^{-3}$ )	0.978(2.64 $\times 10^{-3}$ )
45.0 – 55.0		0.983(1.01 $\times 10^{-2}$ )	0.983(1.09 $\times 10^{-2}$ )	0.981(1.92 $\times 10^{-2}$ )

TABLE XXXII. Corrections (and relative systematic uncertainties) for dilutions to the mid- $z$  Collins asymmetry from finite azimuthal angular resolution.

$p_T$ Range [GeV/ $c$ ]	VPDMB	JP0	JP1	JP2
6.0 – 7.1	0.776( $3.41 \times 10^{-2}$ )			
7.1 – 8.4	0.836( $5.30 \times 10^{-2}$ )	0.944( $1.53 \times 10^{-2}$ )		
8.4 – 9.9	0.902( $2.01 \times 10^{-2}$ )	0.880( $3.39 \times 10^{-2}$ )		
9.9 – 11.7	0.867( $1.94 \times 10^{-2}$ )	0.884( $2.47 \times 10^{-2}$ )	0.822( $6.97 \times 10^{-2}$ )	
11.7 – 13.8	0.895( $5.28 \times 10^{-3}$ )	0.932( $1.63 \times 10^{-2}$ )	0.960( $2.77 \times 10^{-2}$ )	
13.8 – 16.3	0.906( $1.63 \times 10^{-2}$ )	0.907( $2.26 \times 10^{-2}$ )	0.924( $9.30 \times 10^{-3}$ )	
16.3 – 19.2		0.920( $2.00 \times 10^{-2}$ )	0.863( $1.54 \times 10^{-2}$ )	0.808( $3.66 \times 10^{-2}$ )
19.2 – 22.7		0.943( $9.13 \times 10^{-3}$ )	0.927( $1.08 \times 10^{-2}$ )	0.959( $8.91 \times 10^{-3}$ )
22.7 – 26.8		0.947( $3.02 \times 10^{-2}$ )	0.953( $2.34 \times 10^{-2}$ )	0.954( $7.20 \times 10^{-3}$ )
26.8 – 31.6		0.927( $2.15 \times 10^{-2}$ )	0.916( $2.54 \times 10^{-2}$ )	0.952( $1.17 \times 10^{-2}$ )
31.6 – 37.3		0.877( $1.07 \times 10^{-1}$ )	0.857( $1.30 \times 10^{-1}$ )	0.762( $2.63 \times 10^{-1}$ )
37.3 – 45.0		0.974( $1.77 \times 10^{-2}$ )	0.973( $1.63 \times 10^{-2}$ )	0.972( $1.96 \times 10^{-2}$ )
45.0 – 55.0		0.957( $1.04 \times 10^{-2}$ )	0.957( $1.07 \times 10^{-2}$ )	0.981( $6.71 \times 10^{-3}$ )

TABLE XXXIII. Corrections (and relative systematic uncertainties) for dilutions to the high- $z$  Collins asymmetry from finite azimuthal angular resolution.

$j_T$ Range [GeV/c]	<b>JP0</b>	<b>JP1</b>	<b>JP2</b>
0.1 – 0.2	0.904( $1.23 \times 10^{-2}$ )	0.923( $1.16 \times 10^{-2}$ )	0.893( $9.80 \times 10^{-4}$ )
0.2 – 0.3	0.944( $8.83 \times 10^{-3}$ )	0.933( $8.15 \times 10^{-3}$ )	0.953( $7.96 \times 10^{-3}$ )
0.3 – 0.5	0.975( $7.60 \times 10^{-3}$ )	0.968( $7.54 \times 10^{-3}$ )	0.976( $8.54 \times 10^{-3}$ )
0.5 – 0.7	0.964( $1.23 \times 10^{-2}$ )	0.966( $1.72 \times 10^{-2}$ )	0.969( $2.26 \times 10^{-2}$ )
0.7 – 1.0	0.969( $1.21 \times 10^{-2}$ )	0.974( $6.87 \times 10^{-3}$ )	0.952( $3.35 \times 10^{-2}$ )
1.0 – 2.0	0.957( $2.62 \times 10^{-2}$ )	0.950( $3.07 \times 10^{-2}$ )	0.951( $4.62 \times 10^{-2}$ )

TABLE XXXIV. Corrections (and relative systematic uncertainties) for dilutions to the high- $p_T$ , low- $z$  Collins asymmetry from finite azimuthal angular resolution.

$j_T$ Range [GeV/c]	<b>JP0</b>	<b>JP1</b>	<b>JP2</b>
0.2 – 0.3	0.960( $1.80 \times 10^{-2}$ )	0.950( $2.04 \times 10^{-2}$ )	0.957( $3.18 \times 10^{-2}$ )
0.3 – 0.5	0.956( $9.26 \times 10^{-3}$ )	0.949( $8.16 \times 10^{-3}$ )	0.967( $2.67 \times 10^{-3}$ )
0.5 – 0.7	0.966( $7.75 \times 10^{-3}$ )	0.961( $1.83 \times 10^{-2}$ )	0.976( $1.03 \times 10^{-2}$ )
0.7 – 1.0	0.985( $1.11 \times 10^{-2}$ )	0.983( $9.13 \times 10^{-3}$ )	0.984( $1.08 \times 10^{-2}$ )
1.0 – 2.0	0.990( $3.04 \times 10^{-2}$ )	0.989( $3.54 \times 10^{-2}$ )	0.987( $1.75 \times 10^{-2}$ )

TABLE XXXV. Corrections (and relative systematic uncertainties) for dilutions to the high- $p_T$ , mid- $z$  Collins asymmetry from finite azimuthal angular resolution.

$j_T$ Range [GeV/c]	<b>JP0</b>	<b>JP1</b>	<b>JP2</b>
0.3 – 0.5	0.885( $6.96 \times 10^{-3}$ )	0.882( $5.09 \times 10^{-2}$ )	0.837( $1.33 \times 10^{-1}$ )
0.5 – 0.7	0.954( $1.24 \times 10^{-2}$ )	0.956( $1.69 \times 10^{-2}$ )	0.979( $1.58 \times 10^{-2}$ )
0.7 – 1.0	0.947( $8.51 \times 10^{-3}$ )	0.950( $8.31 \times 10^{-3}$ )	0.919( $3.31 \times 10^{-3}$ )
1.0 – 2.0	0.951( $1.71 \times 10^{-2}$ )	0.941( $1.18 \times 10^{-2}$ )	0.976( $8.07 \times 10^{-3}$ )

TABLE XXXVI. Corrections (and relative systematic uncertainties) for dilutions to the high- $p_T$ , high- $z$  Collins asymmetry from finite azimuthal angular resolution.

## Appendix C: Non-pion Background Corrections

$z$	Range	$f_1^\pi$	$f_1^K$	$f_1^p$	$f_2^\pi$	$f_2^K$	$f_2^p$	$f_3^\pi$	$f_3^K$	$f_3^p$	Rel. Syst.
0.1 – 0.2	0.853	0.092	0.055	0.468	0.379	0.149	0.271	0.124	0.449	3.69 × 10 <sup>-2</sup>	
0.2 – 0.3	0.893	0.051	0.053	0.426	0.312	0.262	0.065	0.357	0.573	6.85 × 10 <sup>-3</sup>	
0.3 – 0.4	0.931	0.022	0.041	0.451	0.311	0.238	0.038	0.498	0.464	2.57 × 10 <sup>-2</sup>	
0.4 – 0.5	0.948	0.029	0.014	0.457	0.394	0.149	0.034	0.605	0.361	1.12 × 10 <sup>-3</sup>	
0.5 – 0.8	0.942	0.042	0.000	0.450	0.535	0.015	0.035	0.844	0.121	5.13 × 10 <sup>-3</sup>	
<hr/>											
0.1 – 0.2	0.847	0.094	0.059	0.478	0.358	0.161	0.249	0.110	0.490	4.14 × 10 <sup>-2</sup>	
0.2 – 0.3	0.881	0.052	0.065	0.413	0.301	0.287	0.054	0.320	0.622	1.06 × 10 <sup>-2</sup>	
0.3 – 0.4	0.927	0.024	0.042	0.422	0.283	0.295	0.029	0.419	0.551	3.60 × 10 <sup>-2</sup>	
0.4 – 0.5	0.944	0.030	0.017	0.415	0.365	0.220	0.027	0.484	0.488	1.29 × 10 <sup>-2</sup>	
0.5 – 0.8	0.933	0.050	0.001	0.424	0.539	0.037	0.031	0.736	0.233	8.88 × 10 <sup>-4</sup>	

TABLE XXXVII. Positively (top) and negatively (bottom) charged pion, kaon, and proton yield fractions and relative systematic uncertainties for background corrections to the low- $p_T$  asymmetries.

$z$	Range	$f_1^\pi$	$f_1^K$	$f_1^p$	$f_2^\pi$	$f_2^K$	$f_2^p$	$f_3^\pi$	$f_3^K$	$f_3^p$	Rel. Syst.
0.1 – 0.2	0.913	0.051	0.030	0.504	0.294	0.202	0.063	0.470	0.467	3.57 × 10 <sup>-3</sup>	
0.2 – 0.3	0.965	0.020	0.005	0.566	0.241	0.192	0.047	0.429	0.523	4.83 × 10 <sup>-3</sup>	
0.3 – 0.4	0.945	0.036	0.001	0.515	0.453	0.032	0.044	0.672	0.283	7.30 × 10 <sup>-3</sup>	
0.4 – 0.5	0.921	0.049	0.001	0.483	0.470	0.046	0.045	0.597	0.357	2.22 × 10 <sup>-2</sup>	
0.5 – 0.8	0.892	0.067	0.002	0.460	0.487	0.053	0.055	0.598	0.346	5.56 × 10 <sup>-3</sup>	
<hr/>											
0.1 – 0.2	0.911	0.054	0.029	0.507	0.296	0.197	0.063	0.478	0.458	4.25 × 10 <sup>-3</sup>	
0.2 – 0.3	0.966	0.015	0.009	0.586	0.204	0.209	0.050	0.343	0.605	1.48 × 10 <sup>-3</sup>	
0.3 – 0.4	0.943	0.038	0.001	0.533	0.428	0.039	0.049	0.613	0.338	6.93 × 10 <sup>-3</sup>	
0.4 – 0.5	0.916	0.053	0.002	0.501	0.440	0.058	0.050	0.519	0.430	5.03 × 10 <sup>-2</sup>	
0.5 – 0.8	0.882	0.071	0.003	0.486	0.439	0.075	0.062	0.482	0.455	2.65 × 10 <sup>-2</sup>	

TABLE XXXVIII. Positively (top) and negatively (bottom) charged pion, kaon, and proton yield fractions and relative systematic uncertainties for background corrections to the mid- $p_T$  asymmetries.

$z$	Range	$f_1^\pi$	$f_1^K$	$f_1^p$	$f_2^\pi$	$f_2^K$	$f_2^p$	$f_3^\pi$	$f_3^K$	$f_3^p$	Rel. Syst.
0.1 – 0.2	0.970	0.016	0.006	0.609	0.283	0.108	0.060	0.578	0.361	3.60 × 10 <sup>-3</sup>	
0.2 – 0.3	0.955	0.025	0.007	0.550	0.285	0.164	0.050	0.379	0.570	6.96 × 10 <sup>-4</sup>	
0.3 – 0.4	0.920	0.061	0.002	0.474	0.453	0.073	0.050	0.510	0.439	3.65 × 10 <sup>-2</sup>	
0.4 – 0.5	0.889	0.085	0.005	0.434	0.459	0.106	0.053	0.455	0.492	1.27 × 10 <sup>-2</sup>	
0.5 – 0.8	0.859	0.107	0.010	0.415	0.446	0.137	0.063	0.424	0.510	5.38 × 10 <sup>-2</sup>	
<hr/>											
0.1 – 0.2	0.971	0.016	0.005	0.638	0.266	0.096	0.069	0.562	0.368	2.14 × 10 <sup>-3</sup>	
0.2 – 0.3	0.959	0.023	0.006	0.609	0.236	0.155	0.064	0.315	0.620	1.86 × 10 <sup>-2</sup>	
0.3 – 0.4	0.924	0.057	0.003	0.534	0.382	0.084	0.067	0.426	0.507	2.47 × 10 <sup>-2</sup>	
0.4 – 0.5	0.890	0.080	0.008	0.492	0.371	0.136	0.070	0.347	0.579	3.03 × 10 <sup>-2</sup>	
0.5 – 0.8	0.873	0.079	0.023	0.478	0.283	0.237	0.081	0.240	0.677	4.88 × 10 <sup>-3</sup>	

TABLE XXXIX. Positively (top) and negatively (bottom) charged pion, kaon, and proton yield fractions and relative systematic uncertainties for background corrections to the high- $p_T$  asymmetries.

$p_T$ Range [GeV/c]	$f_1^\pi$	$f_1^K$	$f_1^p$	$f_2^\pi$	$f_2^K$	$f_2^p$	$f_3^\pi$	$f_3^K$	$f_3^p$	Rel. Syst.
6.0 – 7.1	0.885	0.093	0.022	0.404	0.352	0.191	0.112	0.013	0.847	$4.74 \times 10^{-3}$
7.1 – 8.4	0.867	0.099	0.035	0.548	0.235	0.210	0.074	0.004	0.791	$1.66 \times 10^{-4}$
8.4 – 9.9	0.833	0.111	0.056	0.424	0.495	0.081	0.310	0.017	0.508	$4.44 \times 10^{-2}$
9.9 – 11.7	0.854	0.075	0.071	0.424	0.452	0.123	0.081	0.296	0.401	$6.20 \times 10^{-2}$
11.7 – 13.8	0.850	0.089	0.060	0.478	0.367	0.155	0.461	0.161	0.238	$4.03 \times 10^{-2}$
13.8 – 16.3	0.889	0.062	0.047	0.487	0.320	0.193	0.072	0.540	0.388	$7.95 \times 10^{-2}$
16.3 – 19.2	0.897	0.061	0.033	0.451	0.311	0.238	0.055	0.429	0.516	$6.29 \times 10^{-3}$
19.2 – 22.7	0.938	0.036	0.019	0.547	0.270	0.182	0.065	0.472	0.463	$2.77 \times 10^{-2}$
22.7 – 26.8	0.971	0.008	0.012	0.617	0.219	0.163	0.061	0.484	0.454	$9.88 \times 10^{-4}$
26.8 – 31.6	0.971	0.021	0.000	0.608	0.295	0.096	0.060	0.581	0.357	$5.79 \times 10^{-3}$
31.6 – 37.3	0.969	0.023	0.000	0.598	0.382	0.019	0.059	0.767	0.173	$3.05 \times 10^{-3}$
37.3 – 45.0	0.964	0.026	0.001	0.589	0.385	0.026	0.059	0.696	0.245	$8.19 \times 10^{-3}$
45.0 – 55.0	0.957	0.033	0.001	0.568	0.398	0.033	0.060	0.641	0.298	$2.30 \times 10^{-2}$

TABLE XL. Positively charged pion, kaon, and proton yield fractions and relative systematic uncertainties for background corrections to the low- $z$  asymmetries.

$p_T$	Range	$f_1^\pi$	$f_1^K$	$f_1^p$	$f_2^\pi$	$f_2^K$	$f_2^p$	$f_3^\pi$	$f_3^K$	$f_3^p$	Rel. Syst.
[GeV/c]											
6.0 – 7.1	0.881	0.092	0.027	0.383	0.319	0.251	0.085	0.009	0.877	$9.16 \times 10^{-3}$	
7.1 – 8.4	0.864	0.095	0.041	0.502	0.238	0.252	0.033	0.004	0.848	$3.22 \times 10^{-2}$	
8.4 – 9.9	0.829	0.106	0.065	0.504	0.409	0.087	0.277	0.022	0.549	$4.02 \times 10^{-2}$	
9.9 – 11.7	0.838	0.092	0.070	0.458	0.418	0.125	0.144	0.245	0.386	$5.13 \times 10^{-2}$	
11.7 – 13.8	0.850	0.087	0.061	0.477	0.368	0.156	0.447	0.170	0.240	$4.69 \times 10^{-2}$	
13.8 – 16.3	0.888	0.064	0.045	0.496	0.324	0.180	0.069	0.546	0.385	$1.44 \times 10^{-2}$	
16.3 – 19.2	0.902	0.060	0.032	0.455	0.323	0.221	0.050	0.480	0.469	$4.12 \times 10^{-3}$	
19.2 – 22.7	0.929	0.044	0.020	0.546	0.266	0.188	0.069	0.455	0.476	$1.94 \times 10^{-2}$	
22.7 – 26.8	0.971	0.009	0.011	0.636	0.212	0.152	0.068	0.479	0.452	$5.52 \times 10^{-4}$	
26.8 – 31.6	0.973	0.020	0.000	0.640	0.291	0.069	0.069	0.596	0.334	$5.33 \times 10^{-3}$	
31.6 – 37.3	0.971	0.021	0.001	0.641	0.335	0.024	0.071	0.700	0.229	$4.70 \times 10^{-3}$	
37.3 – 45.0	0.965	0.025	0.001	0.633	0.339	0.028	0.073	0.640	0.286	$5.52 \times 10^{-3}$	
45.0 – 55.0	0.961	0.029	0.001	0.632	0.329	0.039	0.078	0.551	0.371	$4.46 \times 10^{-4}$	

TABLE XLI. Negatively charged pion, kaon, and proton yield fractions and relative systematic uncertainties for background corrections to the low- $z$  asymmetries.

$p_T$ Range [GeV/c]	$f_1^\pi$	$f_1^K$	$f_1^p$	$f_2^\pi$	$f_2^K$	$f_2^p$	$f_3^\pi$	$f_3^K$	$f_3^p$	Rel. Syst.
6.0 – 7.1	0.759	0.123	0.118	0.090	0.776	0.134	0.490	0.017	0.371	$1.87 \times 10^{-2}$
7.1 – 8.4	0.866	0.042	0.091	0.442	0.351	0.207	0.019	0.582	0.399	$1.36 \times 10^{-1}$
8.4 – 9.9	0.895	0.067	0.037	0.080	0.504	0.416	0.042	0.451	0.507	$2.61 \times 10^{-2}$
9.9 – 11.7	0.894	0.064	0.039	0.413	0.317	0.270	0.048	0.442	0.510	$9.52 \times 10^{-3}$
11.7 – 13.8	0.942	0.008	0.046	0.481	0.183	0.336	0.045	0.288	0.667	$1.54 \times 10^{-3}$
13.8 – 16.3	0.963	0.029	0.002	0.528	0.040	0.432	0.043	0.047	0.910	$4.17 \times 10^{-3}$
16.3 – 19.2	0.966	0.017	0.005	0.574	0.300	0.125	0.048	0.567	0.385	$5.21 \times 10^{-3}$
19.2 – 22.7	0.964	0.018	0.005	0.579	0.292	0.128	0.048	0.498	0.453	$4.81 \times 10^{-3}$
22.7 – 26.8	0.963	0.016	0.008	0.572	0.231	0.197	0.049	0.347	0.603	$7.57 \times 10^{-4}$
26.8 – 31.6	0.959	0.020	0.009	0.557	0.235	0.206	0.050	0.313	0.636	$7.71 \times 10^{-3}$
31.6 – 37.3	0.941	0.046	0.001	0.517	0.433	0.051	0.053	0.553	0.394	$1.35 \times 10^{-3}$
37.3 – 45.0	0.928	0.057	0.002	0.491	0.444	0.065	0.054	0.514	0.431	$3.59 \times 10^{-2}$
45.0 – 55.0	0.914	0.072	0.004	0.465	0.443	0.092	0.057	0.461	0.482	$4.54 \times 10^{-2}$

TABLE XLII. Positively charged pion, kaon, and proton yield fractions and relative systematic uncertainties for background corrections to the mid- $z$  asymmetries.

$p_T$ Range [GeV/ $c$ ]	$f_1^\pi$	$f_1^K$	$f_1^p$	$f_2^\pi$	$f_2^K$	$f_2^p$	$f_3^\pi$	$f_3^K$	$f_3^p$	Rel. Syst.
6.0 – 7.1	0.742	0.118	0.140	0.122	0.703	0.175	0.425	0.014	0.428	$6.87 \times 10^{-3}$
7.1 – 8.4	0.848	0.046	0.105	0.424	0.355	0.221	0.019	0.519	0.462	$1.68 \times 10^{-1}$
8.4 – 9.9	0.877	0.063	0.058	0.058	0.395	0.547	0.020	0.396	0.584	$1.61 \times 10^{-2}$
9.9 – 11.7	0.878	0.068	0.051	0.380	0.294	0.326	0.041	0.368	0.592	$1.94 \times 10^{-3}$
11.7 – 13.8	0.942	0.008	0.046	0.506	0.159	0.335	0.041	0.278	0.681	$1.40 \times 10^{-2}$
13.8 – 16.3	0.963	0.029	0.002	0.532	0.304	0.164	0.045	0.491	0.464	$6.68 \times 10^{-4}$
16.3 – 19.2	0.966	0.007	0.016	0.589	0.119	0.291	0.049	0.214	0.736	$2.13 \times 10^{-3}$
19.2 – 22.7	0.966	0.015	0.006	0.614	0.230	0.156	0.055	0.388	0.556	$1.29 \times 10^{-3}$
22.7 – 26.8	0.966	0.011	0.010	0.624	0.153	0.222	0.060	0.233	0.706	$1.59 \times 10^{-3}$
26.8 – 31.6	0.960	0.024	0.004	0.614	0.261	0.125	0.065	0.363	0.572	$8.29 \times 10^{-3}$
31.6 – 37.3	0.945	0.041	0.001	0.584	0.359	0.057	0.071	0.467	0.462	$5.45 \times 10^{-2}$
37.3 – 45.0	0.935	0.052	0.002	0.560	0.364	0.076	0.074	0.418	0.509	$8.68 \times 10^{-2}$
45.0 – 55.0	0.924	0.065	0.005	0.543	0.348	0.108	0.081	0.351	0.568	$1.21 \times 10^{-1}$

TABLE XLIII. Negatively charged pion, kaon, and proton yield fractions and relative systematic uncertainties for background corrections to the mid- $z$  asymmetries.

$p_T$ Range [GeV/c]	$f_1^\pi$	$f_1^K$	$f_1^p$	$f_2^\pi$	$f_2^K$	$f_2^p$	$f_3^\pi$	$f_3^K$	$f_3^p$	Rel. Syst.
6.0 – 7.1	0.908	0.054	0.036	0.301	0.476	0.223	0.035	0.657	0.308	$3.89 \times 10^{-3}$
7.1 – 8.4	0.915	0.038	0.043	0.409	0.340	0.251	0.035	0.520	0.445	$2.98 \times 10^{-2}$
8.4 – 9.9	0.953	0.010	0.032	0.477	0.238	0.285	0.035	0.412	0.553	$1.20 \times 10^{-2}$
9.9 – 11.7	0.942	0.013	0.034	0.491	0.358	0.151	0.037	0.559	0.403	$2.56 \times 10^{-2}$
11.7 – 13.8	0.952	0.034	0.000	0.490	0.489	0.020	0.038	0.801	0.161	$5.03 \times 10^{-3}$
13.8 – 16.3	0.948	0.040	0.001	0.480	0.494	0.026	0.039	0.738	0.223	$1.54 \times 10^{-2}$
16.3 – 19.2	0.932	0.040	0.001	0.513	0.450	0.036	0.047	0.643	0.310	$1.22 \times 10^{-2}$
19.2 – 22.7	0.926	0.047	0.001	0.502	0.451	0.047	0.049	0.584	0.367	$5.53 \times 10^{-3}$
22.7 – 26.8	0.920	0.058	0.002	0.481	0.453	0.065	0.051	0.529	0.420	$2.83 \times 10^{-2}$
26.8 – 31.6	0.908	0.072	0.003	0.458	0.457	0.084	0.052	0.483	0.464	$5.21 \times 10^{-3}$
31.6 – 37.3	0.894	0.086	0.006	0.434	0.444	0.121	0.053	0.422	0.524	$1.03 \times 10^{-1}$
37.3 – 45.0	0.866	0.110	0.010	0.397	0.458	0.143	0.055	0.419	0.521	$3.83 \times 10^{-2}$
45.0 – 55.0	0.821	0.140	0.013	0.364	0.474	0.159	0.057	0.413	0.528	$1.39 \times 10^{-1}$

TABLE XLIV. Positively charged pion, kaon, and proton yield fractions and relative systematic uncertainties for background corrections to the high- $z$  asymmetries.

$p_T$ Range [GeV/ $c$ ]	$f_1^\pi$	$f_1^K$	$f_1^p$	$f_2^\pi$	$f_2^K$	$f_2^p$	$f_3^\pi$	$f_3^K$	$f_3^p$	Rel. Syst.
6.0 – 7.1	0.898	0.051	0.048	0.308	0.425	0.267	0.028	0.563	0.409	$5.65 \times 10^{-2}$
7.1 – 8.4	0.912	0.041	0.044	0.383	0.300	0.317	0.024	0.450	0.526	$3.26 \times 10^{-2}$
8.4 – 9.9	0.949	0.012	0.033	0.415	0.324	0.261	0.027	0.436	0.537	$4.50 \times 10^{-3}$
9.9 – 11.7	0.939	0.017	0.034	0.448	0.265	0.287	0.031	0.358	0.611	$2.31 \times 10^{-2}$
11.7 – 13.8	0.943	0.039	0.001	0.475	0.490	0.035	0.035	0.712	0.253	$3.62 \times 10^{-3}$
13.8 – 16.3	0.944	0.042	0.001	0.495	0.468	0.037	0.041	0.659	0.299	$2.10 \times 10^{-2}$
16.3 – 19.2	0.929	0.042	0.001	0.526	0.427	0.047	0.050	0.571	0.378	$1.53 \times 10^{-2}$
19.2 – 22.7	0.923	0.049	0.002	0.531	0.413	0.056	0.058	0.519	0.423	$2.01 \times 10^{-2}$
22.7 – 26.8	0.918	0.056	0.003	0.530	0.390	0.080	0.064	0.437	0.499	$7.08 \times 10^{-3}$
26.8 – 31.6	0.914	0.065	0.005	0.523	0.369	0.107	0.071	0.387	0.541	$1.94 \times 10^{-2}$
31.6 – 37.3	0.904	0.075	0.010	0.504	0.343	0.153	0.076	0.324	0.601	$4.95 \times 10^{-2}$
37.3 – 45.0	0.877	0.090	0.017	0.474	0.323	0.199	0.078	0.271	0.642	$6.04 \times 10^{-2}$
45.0 – 55.0	0.876	0.086	0.031	0.468	0.246	0.286	0.084	0.184	0.732	$1.50 \times 10^{-1}$

TABLE XLV. Negatively charged pion, kaon, and proton yield fractions and relative systematic uncertainties for background corrections to the high- $z$  asymmetries.

$p_T$ Range [GeV/ $c$ ]	$f_1^\pi$	$f_1^K$	$f_1^p$	$f_2^\pi$	$f_2^K$	$f_2^p$	$f_3^\pi$	$f_3^K$	$f_3^p$	Rel. Syst.
6.0 – 7.1	0.840	0.102	0.058	0.321	0.438	0.204	0.182	0.012	0.755	$8.45 \times 10^{-3}$
7.1 – 8.4	0.864	0.090	0.045	0.473	0.302	0.221	0.049	0.030	0.806	$3.26 \times 10^{-2}$
8.4 – 9.9	0.840	0.101	0.059	0.420	0.451	0.130	0.263	0.066	0.532	$3.09 \times 10^{-2}$
9.9 – 11.7	0.856	0.079	0.064	0.422	0.380	0.198	0.083	0.327	0.464	$4.07 \times 10^{-2}$
11.7 – 13.8	0.873	0.068	0.057	0.482	0.311	0.207	0.312	0.206	0.389	$2.96 \times 10^{-2}$
13.8 – 16.3	0.908	0.054	0.034	0.502	0.280	0.218	0.058	0.416	0.526	$3.33 \times 10^{-2}$
16.3 – 19.2	0.914	0.050	0.028	0.492	0.284	0.223	0.051	0.424	0.524	$3.68 \times 10^{-3}$
19.2 – 22.7	0.940	0.034	0.017	0.559	0.267	0.175	0.062	0.457	0.480	$1.88 \times 10^{-2}$
22.7 – 26.8	0.970	0.010	0.011	0.619	0.210	0.171	0.061	0.425	0.513	$3.49 \times 10^{-4}$
26.8 – 31.6	0.969	0.021	0.002	0.614	0.281	0.104	0.062	0.517	0.420	$4.34 \times 10^{-3}$
31.6 – 37.3	0.964	0.027	0.001	0.601	0.369	0.030	0.064	0.678	0.258	$2.51 \times 10^{-3}$
37.3 – 45.0	0.958	0.032	0.001	0.588	0.373	0.038	0.065	0.622	0.313	$1.16 \times 10^{-2}$
45.0 – 55.0	0.950	0.039	0.001	0.575	0.373	0.052	0.068	0.557	0.374	$2.50 \times 10^{-3}$

TABLE XLVI. Pion, kaon, and proton yield fractions and relative systematic uncertainties for background corrections to the low+mid- $z$  asymmetries.

## ACKNOWLEDGMENTS

JLD gratefully acknowledges his colleagues at VU for the opportunity to continue his work on STAR. In particular he would like to recognize Shirvel Stanislaus and Don Koetke for taking on extra teaching responsibilities, allowing him to devote his full-time effort to this analysis during the fall of 2014. In addition, he would like to recognize Jacob Long for his efforts analyzing Monte Carlo for this analysis as a summer research student during the summer of 2013. Finally, JLD would like to acknowledge Pibero Djawotho for generously giving of his time and expertise, even after his transition to new horizons.

---

- [1] A. Airapetian *et al.* (HERMES Collaboration), Phys. Rev. Lett. **94**, 012002 (2005); **103**, 152002 (2009); Phys. Lett. B **693**, 11 (2010).
- [2] V. Y. Alexakhin *et al.* (COMPASS Collaboration), Phys. Rev. Lett. **94**, 202002 (2005); E. S. Ageev *et al.* (COMPASS Collaboration), Nucl. Phys. **B765**, 31 (2007); M. G. Alekseev *et al.* (COMPASS Collaboration), Phys. Lett. B **673**, 127 (2009); **692**, 240 (2010); C. Adolph *et al.* (COMPASS Collaboration), **717**, 376 (2012); N. Makke (COMPASS Collaboration), PoS **EPS-HEP2013**, 443 (2013).
- [3] X. Qian *et al.* (Jefferson Lab Hall A Collaboration), Phys. Rev. Lett. **107**, 072003 (2011).
- [4] A. Efremov and O. Teryaev, Yad. Fiz. **36**, 242 (1982), [Sov. J. Nucl. Phys. 36, 140 (1982)].
- [5] J. Qiu and G. Sterman, Phys. Rev. D **59**, 014004 (1998).
- [6] D. Sivers, Phys. Rev. D **41**, 83 (1990); **43**, 261 (1991).
- [7] D. Boer, P. J. Mulders, and F. Pijlman, Nucl. Phys. **B667**, 201 (2003).
- [8] J. Collins, Nucl. Phys. **B396**, 161 (1993).
- [9] M. Anselmino *et al.*, Phys. Rev. D **73**, 014020 (2006); U. D'Alesio, F. Murgia, and C. Pisano, **83**, 034021 (2011).
- [10] M. Cacciari, G. P. Salam, and G. Soyez, J. High Energy Phys. **04**, 063 (2008).
- [11] L. Adamczyk *et al.* (STAR Collaboration), Phys. Rev. Lett. **115**, 092002 (2015).
- [12] J. Dunlop, “Lumi txt file,” (2011).
- [13] RHIC Polarimetry Group, “RHIC Polarizations for Runs 9-12,” (2013), C-A/AP/490.

- [14] G. G. Ohlsen and P. W. Keaton, Nucl. Inst. & Meth. **109**, 41 (1973).
- [15] J. L. Drachenberg, *Forward di-hadron asymmetries from  $p^{\uparrow(\downarrow)} + p$  at  $\sqrt{s} = 200$  GeV at STAR*, Ph.D. thesis, Texas A&M University (2012).
- [16] T. Sjöstrand, S. Mrenna, and P. Skands, J. High Energy Phys. **05**, 026 (2006).
- [17] P. Z. Skands, Phys. Rev. D **82**, 074018 (2010).
- [18] R. Brun *et al.*, “GEANT3,” (1987), CERN-DD-EE-84-1; R. Brun, F. Carminati, and S. Giani, “GEANT Detector Description and Simulation Tool,” (1994), CERN-W5013, CERN-W-5013.
- [19] B. Page, “2011 L2 Online Monitoring: L2 Jet (High Threshold),” <http://online.star.bnl.gov/L2algo2011/l2jetHigh/archive.html>.
- [20] L. Adamczyk *et al.* (STAR Collaboration), Phys. Rev. D **86**, 032006 (2012).
- [21] R. Fatemi (STAR Collaboration), AIP Conf. Proc. **1441**, 233 (2012).
- [22] P. R. Bevington and K. D. Robinson, *Data Reduction and Error Analysis for the Physical Sciences*, 3rd ed. (McGraw-Hill, 2003).
- [23] J. Adams *et al.* (STAR Collaboration), Phys. Rev. C **70**, 054907 (2004).
- [24] L. Huo, *In-Jet Tracking Efficiency Analysis for the STAR Time Projection Chamber in Polarized Proton-Proton Collisions at  $\sqrt{S} = 200$  GeV*, Master’s thesis, Texas A&M University (2012).
- [25] M. Shao *et al.*, Nucl. Instr. Meth. **A558**, 419 (2006).
- [26] Y. Xu *et al.*, Nucl. Inst. & Meth. **A614**, 28 (2010).
- [27] STAR ZCD Polarimetry Group, “ZDC Scaler Polarimetry,” <http://online.star.bnl.gov/scaler2011/polarimetry/>.
- [28] B. Abelev *et al.* (STAR Collaboration), Phys. Rev. Lett. **99**, 142003 (2007).
- [29] A. Mukherjee and W. Vogelsang, Phys. Rev. D **86**, 094009 (2012).
- [30] R. Seidl *et al.* (Belle Collaboration), Phys. Rev. Lett. **96**, 232002 (2006); Phys. Rev. D **86**, 039905(E) (2012).
- [31] L. Adamczyk *et al.* (STAR Collaboration), Phys. Rev. Lett. **115**, 242501 (2015).
- [32] M. J. Skoby (STAR Collaboration), in *Proceedings of the 21st International Symposium on Spin Physics (Spin2014)* (2015).
- [33] J. K. Adkins and J. L. Drachenberg (STAR Collaboration), in *Proceedings of the 21st International Symposium on Spin Physics (Spin2014)* (2015).

- [34] M. Anselmino, M. Boglione, U. D'Alesio, F. Kotzinian, F. Murgia, and A. Prokudin, Phys. Rev. D **75**, 054032 (2007); M. Anselmino, M. Boglione, U. D'Alesio, F. Kotzinian, S. Melis, F. Murgia, and A. Prokudin, Nucl. Phys. B, Proc. Suppl. **191**, 98 (2009).
- [35] Z.-B. Kang, A. Prokudin, F. Ringer, and F. Yuan, In preparation; M. Anselmino, M. Boglione, U. D'Alesio, S. Melis, F. Murgia, and A. Prokudin, Phys. Rev. D **87**, 094019 (2013); Z.-B. Kang, A. Prokudin, P. Sun, and F. Yuan, **93** (2016).
- [36] S. Kretzer, Phys. Rev. D **62**, 054001 (2000).
- [37] D. de Florian, R. Sassot, and M. Stratmann, Phys. Rev. D **75**, 114010 (2007).
- [38] Z.-B. Kang, X. Liu, F. Ringer, and H. Xing, (2017), arXiv:1705.08443 [hep-ph].